The Interplay Between Quantum Spins and Superconductivity
at the Atomic Level

Dissertation

zur Erlangung des Doktorgrades der Naturwissenschaften
(Dr. rer. nat.)

der

Naturwissenschaftlichen Fakultät II
Chemie, Physik und Mathematik

der Martin-Luther-Universität
Halle-Wittenberg

vorgelegt von

Felix Küster

Doctoral thesis
Author: Felix Küster
Mentoring Professor: Prof. Dr. Stuart Parkin
Institution: Max Planck Institute of Microstructure Physics
                           Weinberg 2, 06120 Halle (Saale)

Reviewers: Prof. Dr. Stuart Parkin (MPI MSP)
                           Prof. Dr. Wolf Widdra (MLU Halle)
                           Prof. Dr. Matthias Bode (JMU Würzburg)

Date of Defense: 20.12.2023

Committee Members: Prof. Dr. Jan Kantelhardt (Chairman)
                           Prof. Dr. Stuart Parkin
                           Prof. Dr. Wolf Widdra
                           Prof. Dr. Matthias Bode
                           Prof. Dr. Georg Woltersdorf
                           Dr. Dirk Sander
                           Dr. Jürgen Henk

Abstract

Single magnetic impurities embedded in a superconducting host material represent a microscopic interface between magnet and superconductor. Very locally around such atomic-scale magnets, electronic quasiparticle resonances emerge at sharply defined energies close to the Fermi level and governed by the impurity spin-to-superconductor coupling strength. These so-called Yu-Shiba-Rusinov states attract great interest in fundamental research and technology as the initial ingredient for application proposals, e.g. in quantum computers.

This thesis explores magnetic surface atoms on superconducting Nb(110) by scanning tunneling microscopy and spectroscopy with normal metallic, superconducting and magnetic tips. Theoretical first-principles and tight-binding models are employed to shed light on the complex phenomena observed in measurement data.

An initial comparison of single adsorbates from different elements correlates spectroscopy in the superconducting and metallic phase as well as Josephson supercurrents to deduce well-defined trends. Chromium yields a particularly interesting candidate for the creation of custom tailored nanostructures. Precisely controlling their relative positions by atomic manipulation with the tip, two interacting Cr impurities are found to unfold an unprecedented flexibility to be tuned on demand, facilitated by indirect mediation through the anisotropic substrate structure. Artificially crafted spin chains are built to explore the predicted emergence of topological superconductivity, thereby unraveling general trends that effectively mimic sought-after Majorana zero modes. After evaluation of different approaches to spin-polarized tunneling, single atom tip apex functionalization is identified as a suitable tool to characterize the ordered spin textures under investigation. Finally, an outlook into two dimensional tailored spin nanostructures with several realized assemblies paves the way for fruitful future research on fundamental and device-based concepts.

Contents

1 Introduction

"Through measurement to knowledge"[1], a motto that Heike Kamerlingh Onnes expressed as paramount for experimental research in his visionary speech at Leiden University. This dates to about thirty years before he discovered the phenomenon of *superconductivity*[2], a phase of matter where electrical current flows without resistance and magnetic fields are expelled, usually showing up at very low temperatures.

Fundamentally driven by curiosity, scientific research is often spurred based on prospects to greatly impact modern technology. This is particularly true for the field of superconductors where Onnes' early vision of high current density magnet coils brought us levitating trains, magnetic resonance imaging (MRI), large-scale particle accelerators and many more.

Recent interest in the interface between magnets and superconductors is motivated by the young field of spintronics striving for energy efficient information storage devices[3] augmented by *spin-triplet* superconductivity[4] as well as the technological quest of information processing with quantum computers demanding new candidates for fault-tolerant qubits. Concerning the latter, high hopes are lying on *Majorana zero modes*[5] that are predicted to emerge at the quantum spin-to-superconductor interface under suitable conditions[6,7] involving topological superconductivity[8,9]. Despite those clear visions, it is a long way to actual realization which requires scientists to start from fundamental research.

The ground breaking achievement of Bardeen, Cooper and Schrieffer in unraveling a microscopic theory about superconductivity[10] enabled theoretical physicists to describe this state of electrons, called a coherent macroscopic matter wave, on the quantum level. That way Yu, Shiba and Rusinov were able to analytically describe the scenario of a magnetic moment originating from just a single atomic impurity present within a superconducting condensate. They found that the competition of fundamental electron-electron interactions of superconducting and magnetic nature induces sharp resonant states locally bound to the impurity[11–13].

In experiments, it was only the *scanning tunneling microscope* (STM) that, operated at very low temperatures, allowed for the direct observation of such *Yu-Shiba-Rusinov* (YSR) states[14] around single magnetic surface adsorbates on a superconductor. After the proposal of Majorana modes arising from hybridized YSR states or *Shiba bands*[6], a true flood of STM research was triggered, addressing both fundamental properties[15–31] and the possible realization of Majorana zero modes in spin chains[32–39]. However, up to

date experiments have by far not reached the desired goal of controllably manipulating such exotic states, rather is their actual observation still a matter of debate[40].

In their 2013 published seminal proposal, Nadj-Perge *et al.* pointed out the necessity to experimentally explore a wide parameter space. They suggest a "systematic experimental approach", using magnetic atoms with different spin, characterizing the single-impurity states and their modification when impurities are brought close enough to interact and building chains with different spacing[6]. To prevent Shiba bands from overlap with the quasiparticle continuum outside the *energy gap* of a condensate, the ideal foundation for topological superconductivity phase is described as having "an *s*-wave superconductor with large gap Δ"[6], YSR states that are "deep" inside the gap with energies near the Fermi level[7] and dilute chains where "adatoms are spaced sufficiently far that direct overlap of their *d* orbitals is negligible, yet close enough that their Yu-Shiba-Rusinov (YSR) states hybridize."[41] Under this premise, a maximum variety of parameters can be tuned to find suitable conditions for topological superconducting phases. Exactly these guidelines well outline the aim of the present thesis.

In this work, single magnetic atoms are deposited on superconducting Nb(110) samples and probed by low-temperature STM. The goal is to establish a platform offering an unprecedented control and tunability of YSR systems. Therefore, in-depth investigations are conducted following a systematic bottom-up approach and using a rich workbench of characterization methods offered by STM, atomic manipulation facilitated assembly of spin nanostructures and with support by *ab initio* and tight-binding calculations.

In chapter 2, after giving a general introduction to the historical relation between superconductivity and magnetism, a basic outline of essential results from BCS theory up until the assumed ground state of magnetic impurities in superconductors shall lay out the foundation for the understanding of measurement results. This is followed by a brief review of the research field of experimentally probing magnetic adsorbates on superconductors without the claim for completeness.

Chapter 3 will start providing a general overview of the STM working principle and a description of the actually used laboratory system. This is followed by an explanation of tip preparation methods, in particular the effect of primarily employed superconducting tips as well as magnetic tips. Next, sample preparation will be shown, from obtaining a clean Nb(110) surface to the manipulation of single adatoms. Finally, a list of theory methods is given used to obtain presented calculation results, however, performed by external collaborators.

Results will be presented in chapter 4. Section 4.1 starts from an investigation of single and isolated adatoms of V, Cr, Mn, Fe and Co on Nb(110) that compares their topographic appearance, spatially resolved multi-orbital YSR spectra, impact on super-conducting order parameter and normal conducting spectra. Data is interpreted by con-

sidering theoretical results about basic properties of those elements on Nb(110) like their density of states, magnetic moment, substrate screening effect and magnetic anisotropy as well as a recently developed theory about unconventional spin excitations. Judging from the obtained information about the orbital occupation dependent differences, chromium is then chosen as being the most versatile element platform to continue with a systematic study about interacting impurity spins.

Section 4.2 reports a superconducting substrate-mediated indirect interaction and hybridization of YSR states. A sensitive effective measure of the coupling strength is proposed which is found to oscillate with remarkable distance and directionality between impurities.

By quenching superconductivity, a sharp normal conductance feature of Cr adatoms is scrutinized in section 4.3 in the framework of unconventional spin excitations evaluated by first-principles calculations with time-dependent density functional theory. Its dependence on magnetic field and temperature is measured as well as the evolution in dimers and trimers.

Continuing with superconductivity, the emergence of Shiba bands in one dimensional assemblies is followed in section 4.4 building a chain atom-by-atom. The systematic approach probing direction, spacing and length dependence is consistently pursued. Observations matching the patterns predicted for Majorana zero modes are found to be nicely reproduced by tight-binding calculations explicitly done in the trivial regime, pointing out the difficulty for unambiguous interpretation in any such measurement.

Section 4.5 presents spin-resolved data on different Cr chains finding both *ferro-* (FM) and *antiferromagnetic* (AFM) order consistently concluded from three distinct spin-polarized STM techniques.

Finally, two dimensional magnetic nanostructures are explored in section 4.6. Boundary modes and 2D Shiba band formation is recorded and compared to lower dimensional data. Experiments on this topic remain still incomplete.

Lastly, conclusions shall be summarized and discussed in chapter 5 under the reservation that not all obtained data are well understood. The presented work is believed to be a valuable contribution for the field of quantum spin-to-superconductor interfaces.

2 Superconductivity and magnetism down to the atomic scale

Since the dawn of superconductivity more than $100^{[42]}$ years ago, it seems inextricably connected to magnetism in one way or the other. Shortly after he discovered the vanishing electrical resistivity of $4.2\,\mathrm{K}$ cold mercury in $1911^{[2]}$, Heike Kamerlingh Onnes envisioned superconducting magnet coils that could reach fields of $10\,\mathrm{T}$ which requires currents unthinkable for usual Cu coils with finite resistance. However, he found out that besides a critical temperature T_c there is a critical current density j_c and critical magnetic field H_c. Exceeding one of these values leads to a loss of zero-resistance superconducting properties. These limitations proved obstacles very hard to overcome and therefore prolonged the technical strive for magnet coils producing high fields to about 50 years of research[43]. Meissner and Ochsenfeld understood in $1933^{[44]}$ that rather than zero resistivity, diamagnetism is the more fundamental property of a superconductor. The well-known effect that inherited their names demonstrated how a magnetic field below H_c is expelled from the bulk of a superconductor up to a thin surface layer suggesting that superconductivity and magnetism are mutually exclusive. Not giving up the efforts, Shubnikov and de Haas[45,46] focused their research on alloys instead of pure metals and found superconductors with two separate critical fields: H_c1 where perfect diamagnetism is lost, and H_c2 when finite resistance sets in. The transition between these so-called Type-II superconductors and those of Type-I, where both values fall together, can be identified by the relation between two fundamental properties: the London penetration depth $\lambda^{[47]}$ of magnetic fields and the Ginzburg-Landau coherence length ζ_GL of the superconducting state, expressed as the parameter κ in the 1950 formulated phenomenological Ginzburg-Landau theory of superconductivity[48]. Solving the equations derived in this theory, Abrikosov could explain the partial penetration of magnetic field in Type-II superconductors by quantized flux tubes running through the material while keeping superconductivity intact in between those normal conducting vortices[49]. Around that time, in 1957, Bardeen, Cooper and Schrieffer came up with an all-embracing microscopic theory of superconductivity[10], explaining its origin in the coupling of electrons to pairs, so-called *Cooper pairs*, occupying a collective quantum state and hence, the creation of a macroscopic wave function. Up to date, it provides the best fundamental understanding of superconductivity and could also explain the competition with magnetic phases microscopically[11–13]. However, it was only

20 years later that experiments again got ahead of theory in finding superconductors with unexpectedly high T_c. The most peculiar problem is the coupling mechanism forming Cooper pairs. It was nicely shown for most metallic, later called conventional, superconductors that this mechanism is explained by electron-electron interactions via phonons. As more materials with unprecedented values of T_c were found, most prominently the cuprates in 1986[50] with up to 135 K, 2008 Fe based compounds[51] or just recently in 2020 hydrogen based superconductors with T_c of 15 °C under extremely high pressure[52], their properties could not be explained with the BCS theory so that they are called unconventional. Interestingly, magnetic interaction seems to be a likely candidate to facilitate Cooper pairing based on the observations of immediate proximity of the superconducting to an antiferromagnetic phase in both the cuprate as well as the Fe based compounds[53]. Moreover, modern research even forces the marriage of magnetism and superconductivity by creating artificial interfaces on the nanoscale where exciting physics occurs. It was found that Cooper pairs can indeed carry spin current[4] by forming spin triplets which is called p-wave instead of the conventional spin singlet s-wave superconductivity, that way spintronics devices could greatly benefit from spin supercurrents. Finally, theoretical research realized the potential of low dimensional magnet-superconductor hybrid structures to bear topological phases, e.g. inside vortices of proximitized topological insulators[54] or in chains of magnetic atoms embedded in a superconductor[6]. In particular, exotic quasiparticles called Majorana fermions, predicted 1937 by Ettore Majorana[55] to be both particle and its own antiparticle, are expected to appear in such topological superconductor systems, attracting great interest for the use in fault-tolerant quantum computation by utilizing their non-Abelian exchange statistics[5,56].

2.1 BCS Theory

The BCS theory is a milestone in the history of superconductivity. It is treated with all its complexity in several textbooks[57–59]. Here, some basic idea shall be given providing relevant results for the understanding of tunneling experiments involving superconductors and quantum magnets that are a major part of this work. The description will be restricted to a conventional s-wave isotropic superconductor[60,61].

2.1.1 Cooper pairing and energy gap

Thinking of forces between electrons, what comes to mind is Coulomb repulsion due to their negative charge. However, the fundamental origin of superconductivity according to the BCS theory is an attractive potential V between electrons inside a solid matter. This intuitively concerns only electrons at the Fermi level E_F since the rest reside around their atomic nuclei. What causes the attractive force is not essential for superconductivity. In

the conventional materials, mostly elementary or alloyed metals, it was shown that the interaction between electrons through exchanging quantized lattice vibrations, phonons, can lead to such an attraction. A prominent analogy is the bond between two protons via exchange of their electrons to the H_2 molecule[53]. It can be shown that however small the attractive potential, it is energetically favorable for two electrons at the Fermi level to form a bond, a Cooper pair. Under the condition that the momentum of their center of mass is at rest, they should occupy states with opposite momentum $\mathbf{k}$ and their Cooper pair wave function must fulfill the Pauli principle, hence for even (odd) spatial symmetry a spin singlet (triplet) state is occupied. Here, the more common case of opposite spins is considered, so that the Cooper pair is described as $\{\mathbf{k}\uparrow, -\mathbf{k}\downarrow\}$. Further, the attractive potential has a characteristic length scale which is defined as the BCS coherence length ζ_0 and can be interpreted as the average size of a Cooper pair, usually in the order of $100\,\mathrm{nm}$. The effective Hamiltonian of the system can be written as

$$H_{\mathrm{BCS}} = H_0 + H_{\mathrm{int}} \tag{2.1}$$

with the Hamiltonian for an electron band with dispersion relation $\epsilon_{\mathbf{k}}$

$$H_0 = \sum_{\mathbf{k}\sigma}(\epsilon_{\mathbf{k}} - \mu)c_{\mathbf{k}\sigma}^{\dagger}c_{\mathbf{k}\sigma} \tag{2.2}$$

where μ is the chemical potential and $c_{\mathbf{k}\sigma}^{\dagger}$ is the fermionic creation operator for an electron of momentum k and spin σ. The interaction part is given by

$$H_{\mathrm{int}} = \frac{1}{2}\sum_{\mathbf{k}\mathbf{k}'}V_{\mathbf{k}\mathbf{k}'}c_{\mathbf{k}\uparrow}^{\dagger}c_{-\mathbf{k}\downarrow}^{\dagger}c_{-\mathbf{k}'\downarrow}c_{\mathbf{k}'\uparrow} \tag{2.3}$$

and can be decoupled by the mean-field approximation, so that

$$H_{\mathrm{int}} \approx \sum_{\mathbf{k}}\Delta_{\mathbf{k}}\left\langle c_{\mathbf{k}\uparrow}^{\dagger}c_{-\mathbf{k}\downarrow}^{\dagger}\right\rangle - \sum_{\mathbf{k}}\left(\Delta_{\mathbf{k}}c_{\mathbf{k}\uparrow}^{\dagger}c_{-\mathbf{k}\downarrow}^{\dagger} + \Delta_{\mathbf{k}}^{*}c_{\mathbf{k}\uparrow}c_{-\mathbf{k}\downarrow}\right) \tag{2.4}$$

where $\langle\rangle$ denotes the mean value and the function

$$\Delta_{\mathbf{k}} = -\frac{1}{2}\sum_{\mathbf{k}'}V_{\mathbf{k}\mathbf{k}'}\left\langle c_{-\mathbf{k}'\downarrow}c_{\mathbf{k}'\uparrow}\right\rangle \tag{2.5}$$

has been defined. The resulting Hamiltonian H_{BCS} from equation 2.1 can be solved in different ways, one is to employ the so-called Bogoliubov transformation

$$c_{\mathbf{k}\uparrow} = u_{\mathbf{k}}^{*}\gamma_{\mathbf{k}\uparrow} + v_{\mathbf{k}}\gamma_{-\mathbf{k}\downarrow}^{\dagger} \qquad\qquad c_{-\mathbf{k}\downarrow} = u_{\mathbf{k}}\gamma_{-\mathbf{k}\downarrow}^{\dagger} - v_{\mathbf{k}}^{*}\gamma_{\mathbf{k}\uparrow} \tag{2.6}$$

with the fermionic operators $\gamma_{\mathbf{k}\sigma}, \gamma_{\mathbf{k}\sigma}^{\dagger}$ and the coefficients $u_{\mathbf{k}}$, $v_{\mathbf{k}}$ satisfying the condition

$$|u_{\mathbf{k}}|^2 + |v_{\mathbf{k}}|^2 = 1 \ . \tag{2.7}$$

A physical interpretation is that Cooper pairs constitute a mixed state around the surface of the Fermi sphere where a pair state is simultaneously unoccupied with probability $|u_{\mathbf{k}}|^2$ and occupied with $|v_{\mathbf{k}}|^2$. The function $\Delta_{\mathbf{k}}$ containing the potential $V_{\mathbf{k}\mathbf{k}'}$ after the transformation becomes

$$\Delta_{\mathbf{k}} = -\frac{1}{2} \sum_{\mathbf{k}'} V_{\mathbf{k}\mathbf{k}'} u_{\mathbf{k}'}^* v_{\mathbf{k}'} \left(\langle \gamma_{-\mathbf{k}'\downarrow} \gamma_{-\mathbf{k}'\downarrow}^{\dagger} \rangle - \langle \gamma_{\mathbf{k}'\uparrow}^{\dagger} \gamma_{\mathbf{k}'\uparrow} \rangle \right) \ . \tag{2.8}$$

Substituting 2.6 into 2.1 leads to the Bogoliubov-de Gennes equations (de Gennes 1989) in momentum space

$$(\xi_{\mathbf{k}} - E_{\mathbf{k}})u_{\mathbf{k}} + \Delta_{\mathbf{k}} v_{\mathbf{k}} = 0 \tag{2.9a}$$

$$(\xi_{\mathbf{k}} + E_{\mathbf{k}})v_{\mathbf{k}} + \Delta_{\mathbf{k}}^* u_{\mathbf{k}} = 0 \tag{2.9b}$$

with $\xi_{\mathbf{k}} = \epsilon_{\mathbf{k}} - \mu$ being the non-interacting quasiparticle energy with respect to the chemical potential. The solution yields the probability functions

$$\begin{pmatrix} u_{\mathbf{k}}^2 \\ v_{\mathbf{k}}^2 \end{pmatrix} = \frac{1}{2} \left(1 \pm \frac{\xi_{\mathbf{k}}}{E_{\mathbf{k}}} \right) \tag{2.10}$$

and with $|\Delta_{\mathbf{k}}|^2 = \Delta^2$ in the isotropic superconductor the quasiparticle energy relation

$$E_{\mathbf{k}} = \sqrt{\xi_{\mathbf{k}}^2 + \Delta^2} \ . \tag{2.11}$$

The latter expression has interesting implications on the spectrum of interacting electrons shown in figure 2.1. Their energy E never reaches zero but has a minimum value Δ, below which no states exist any more in an unperturbed superconductor. In other words, conduction electrons condense into Cooper pairs with binding energy Δ and in order to break them a minimum energy 2Δ is needed recreating two quasiparticles. For the density of states in a superconductor, this means that there appears an energy gap of 2Δ around the Fermi level. The BCS result for the *density of states* (DOS), i.e. the number of quasiparticle states per energy interval, is given by

$$\rho_{\mathrm{BCS}}(\xi) = \begin{cases} \rho_0 \frac{|\xi|}{\sqrt{\xi^2 - \Delta^2}} & |\xi| \geq \Delta \\ 0 & |\xi| < \Delta \end{cases} \tag{2.12}$$

with the normal conducting state DOS $\rho_0 = \rho(\xi = 0)$ which is taken as constant in a small energy interval around the Fermi level. It is depicted in figure 2.1c. Integrating over
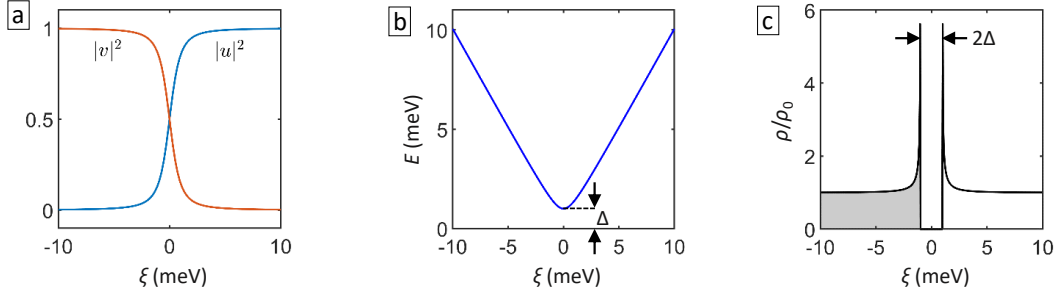
Fig. 2.1: **Important BCS results: a** The functions $|u|^2$ and $|v|^2$, **b** the unpaired electron
energy and **c** the density of states over the normal state electron energy $\xi = \epsilon - \mu$
in a range of ± 10meV and with $\Delta = 1$meV.

the function gives the same result as would be obtained in the non-superconducting state
which means that the missing states inside are redistributed to outside the gap, resulting
in the so-called quasiparticle coherence peaks at the gap edges. This characteristic shape
can be nicely observed in tunneling experiments and defines the energy range of interest
for the present work, where the energy spectrum is "clean" of fermionic states.

The BCS theory describes a state where all Cooper pairs have equal quantum numbers,
hence they have the same wave function and form a macroscopic matter wave. The
probability of scattering events on normal non-magnetic scattering potentials is extremely
low making the Cooper pair wave function insensitive to defects, thus accounting for zero
resistance. What happens at magnetic impurities, however, shall be sketched in the
following.

2.1.2 Magnetic impurity induced states

When a local magnetic impurity, e.g. lattice defects such as interstitials or substitutions
as well as surface adsorbates, with a residual spin moment $\boldsymbol{S}$ is positioned inside a su-
perconducting condensate, the exchange interaction J between the impurity spin and the
spin of the conduction electrons potentially aligns the spin of electrons that form a Cooper
pair. This mechanism is called the paramagnetic effect and results in breaking the Cooper
pair, however, without supplying the elsewise needed excitation energy 2Δ. Therefore,
magnetic moments pose an effective scattering potential for Cooper pairs and quasiparti-
cle states are created inside the energy gap of the superconductor. They are named after
the persons who first investigated this scenario theoretically, Yu-Shiba-Rusinov (YSR)
states[11–13]. Here, a derivation of their energy and eigenstates given in Balatsky *et al.*[60]
shall be outlined. The impurity is chosen at the origin of a BCS *s*-wave superconductor
with the unperturbed Hamiltonian of the form

$$H_0 = \sum_{\mathbf{k}\alpha} \xi_{\mathbf{k}} c^{\dagger}_{\mathbf{k}\alpha} c_{\mathbf{k}\alpha} + \Delta_0 \sum_{\mathbf{k}} \left\{ c^{\dagger}_{\mathbf{k}\uparrow} c^{\dagger}_{-\mathbf{k}\downarrow} + c_{-\mathbf{k}\downarrow} c_{\mathbf{k}\uparrow} \right\} \tag{2.13}$$

with spin index α and the scalar gap size Δ_0. Additionally, a scattering potential U and
the magnetic scattering term

$$H_{\text{ex}} = \frac{1}{2N} \sum_{\mathbf{kk'}\alpha\beta} J(\mathbf{k} - \mathbf{k'}) c_{\mathbf{k}\alpha}^\dagger \boldsymbol{\sigma}_{\alpha\beta} \boldsymbol{S} c_{\mathbf{k'}\beta} \tag{2.14}$$

are considered where $\boldsymbol{\sigma}$ denotes the Pauli operator. Only the classical spin case is considered for the moment where $S \gg 1$ or $T \gg T_{\text{K}}$ with T_{K} being the Kondo temperature[62],
i.e. the unscreened spin regime. In this limit the localized spin acts as a local magnetic
field. After a Bogoliubov transformation like in 2.6, expanding the impurity potentials in
spherical harmonics in $\mathbf{k}$ space, U_l and J_l, and the introduction of scattering phase shifts
δ_l for spin up (+) and spin down (-) electrons in each angular channel

$$\tan \delta_l^{\pm} = \pi \rho_0 (U_l \pm J_l S/2) \,, \tag{2.15}$$

the energies of the in-gap states become

$$\varepsilon_l = \Delta_0 \cos(\delta_l^+ - \delta_l^-) \,. \tag{2.16}$$

The following cases can be identified: (i) Non-magnetic scattering ($\delta_l^+ = \delta_l^-$, $\varepsilon_l = \Delta_0$) leads
to bound states at the gap edge, (ii) weakly magnetic scattering ($|\delta_l^+ - \delta_l^-| \ll 1$, $\varepsilon_l \cong \Delta_0$)
still gives energies very close to the gap edge, (iii) critical scattering ($|\delta_l^+ - \delta_l^-| \sim \pi/2$, $\varepsilon_l \sim 0$)
yields localized states deep in the superconducting gap and (iv) very strong scattering
($|\delta_l^+ - \delta_l^-| \sim \pi$, $\varepsilon_l \simeq -\Delta_0$) when the state reaches the opposite gap edge. An equivalent
result is obtained by a Green function formalism, yielding the bound state energy as

$$\varepsilon = \Delta_0 \frac{1 - (JS_{\text{imp}}\pi\rho_0)^2}{1 + (JS_{\text{imp}}\pi\rho_0)^2} \tag{2.17}$$

and the wave functions obtained from the Bogoliubov transformation are found to vary
as

$$u(r), v(r) \propto \frac{\sin(k_{\text{F}}r - \delta_0^{\pm})}{k_{\text{F}}r} \exp\left[-r|\sin(\delta_0^+ - \delta_0^-)|/\zeta_0\right] \tag{2.18}$$

for particle and hole part and with the superconducting coherence length ζ_0 governing
the characteristic length scale of the YSR wave function exponential decay

$$r_0 \sim \frac{\zeta_0}{|\sin(\delta_0^+ - \delta_0^-)|} \,. \tag{2.19}$$

Note that the injection of an electron with $s_{\text{p}} = -1/2$ at energy ε_0 is equivalent to the
extraction of a hole with $s_{\text{h}} = 1/2$ at $-\varepsilon_0$ and lead to the same quantum mechanical state,
therefore YSR states come in pairs symmetric around the Fermi level. Their intensities, however, are generally different due to the Coulomb potential and energy-dependent
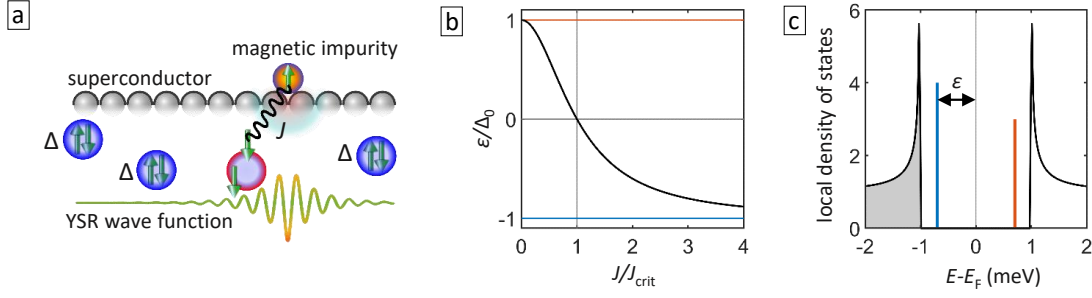
Fig. 2.2: **Yu-Shiba-Rusinov states:** **a** A magnetic impurity couples to a superconducting condensate with exchange coupling J, breaks Cooper pairs due to spin alignment and induces YSR quasiparticles. **b** The YSR quasiparticle energy ε depending on J. **c** Local density of states with energy-symmetric YSR state pair and different spectral weight.

normal state DOS ρ. Moreover it implies that the pair is fully spin polarized with opposite spin. In conclusion, the magnetic impurity locally suppresses superconductivity by aligning Cooper pair spins. The situation is summarized in figure 2.2. This induces quasiparticle resonances called YSR states particle-hole symmetric inside the superconducting gap at energies depending on the impurity spin state S and particularly on the superconductor-impurity magnetic coupling strength J. The YSR wave functions oscillate in space with the Fermi wave vector k_F. Their spatial decay is governed by $1/(k_\mathrm{F}r)$ for short distances and on the long range by an $\exp\left[-r|\sin(\delta_0^+ - \delta_0^-)|/\zeta_0\right]$, hence it can range longer than ζ_0 in this model.

2.1.3 Many-body ground state and quantum phase transition

In a conventional (BCS-like) s-wave superconductor, within the quasiparticle energy gap at $T = 0$ the many-body ground state $|\Psi_0\rangle$ has the quantum spin $S_\mathrm{QP}^0 = 0$. As described above, a magnetic impurity locally induces quasiparticle states inside the gap that can be excited, thus adding or removing a spin 1/2 from the system and changing the spin quantum number. Note that only the quasiparticle quantum spins are considered, the impurity spin can be a classical spin with $S_\mathrm{imp} > 1$, however this is not essential for the discussion. The fundamental question is which total spin number has the ground state of the superconductor in the presence of a magnetic impurity, i.e. whether it has integer or half-integer value. It was found[63] that it can be either way depending on the exchange coupling strength J between the impurity spin and the superconducting condensate. Since the quantum spin state distinguishes only two possible configurations, $S_\mathrm{QP}^0 = S$ and $S_\mathrm{QP}^0 = S \pm 1/2$[1], a first order transition occurs at a critical value of J, also called *quantum phase transition* (QPT). This value is found to be at the crossing of the

---

[1] (+) and (-) sign for FM and AFM coupling, respectively. Only AFM exchange is considered here.

YSR quasiparticle energy through zero which means (from equation 2.17)

$$J_{\mathrm{crit}} = 1/\left(S_{\mathrm{imp}}\pi\rho_0\right) . \tag{2.20}$$

At this point there is a balance between magnetic exchange and superconducting pair potentials. The situation is sketched in figure 2.3. For weaker coupling $J < J_{\mathrm{crit}}$ the ground state remains the BCS-like $S_{\mathrm{QP}}^0 = 0$ where all electrons are paired. The YSR state induced by the impurity can be excited by applying the energy ε to $S_{\mathrm{QP}}^1 = -1/2$. For stronger coupling $J > J_{\mathrm{crit}}$, an electron is bound to the impurity by magnetic exchange thus prohibited to form a Cooper pair. That means for the ground and excited state that $S_{\mathrm{QP}}^0 = -1/2$ and $S_{\mathrm{QP}}^1 = 0$, hence at $J = J_{\mathrm{crit}}$ they cross and change roles. The QPT crossing is expressed in the density of states as a continuous approach of particle- and hole part of the YSR resonance towards the Fermi level as J increases, merging at zero energy for $J = J_{\mathrm{crit}}$ followed by separation with exchanged roles, i.e. retaining their spectral weight imbalance despite not staying strictly constant[60].

Noteworthy, a closely related phenomenon is the screening of the impurity spin by the so-called Kondo effect[62]. In a normal metal, conduction electrons in an energy interval of approximately $k_{\mathrm{B}}T_{\mathrm{K}}$ around the Fermi level, where k_{B} denotes the Boltzmann constant and T_{K} the Kondo temperature, reduce the impurity spin moment by antiferromagnetic coupling, thus screening it. However, if this energy interval competes with the gap size in a superconductor the screening is suppressed due to a depleted density of states leading to YSR states inside the gap. In the weak coupling regime, i.e. $k_{\mathrm{B}}T_{\mathrm{K}} \ll \Delta$, one speaks therefore as of a free spin state. Correspondingly, the strong coupling regime $k_{\mathrm{B}}T_{\mathrm{K}} \gg \Delta$ where a particle is bound antiferromagnetically to the impurity, thus (partially) screening its spin, is referred to as the screened spin state[15].

More theory on YSR states

The analytical results given in this section can provide a good grasp about basic concepts and dependencies within the single magnetic impurity-superconductor system. A fully quantum mechanical, more general approach requires more complex and numerical methods to account for realistic scenarios. In several theoretical works, mean-field calculations[65,66], perturbation theory[67,68], numerical renormalization group theory[69–71] are employed. Further, complex scenarios are considered including Andreev processes[66,72], spin-orbit coupling[26,73,74], skyrmions[75], external magnetic fields[76], crystal field splitting[76,77], temperature[78] and vibrational degrees of freedom[72]. Consequently, calculations went beyond single impurities and studied the interaction between individual quantum spins[79–83], e.g. pointing out the enhancing effect of superconductivity in substrate mediated coupling between magnetic impurities[82] compared to conventional Ruderman-Kittel-Kasuya-Yosida (RKKY)[84–90] interactions in metallic substrates.
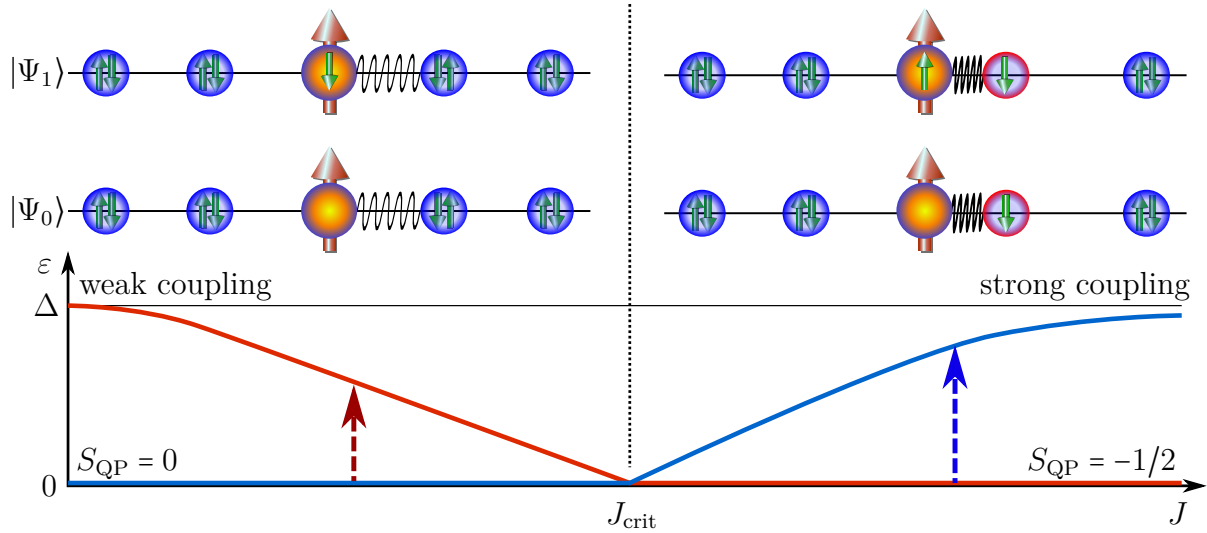
Fig. 2.3: **Many-body quantum state:** Ground state $|\Psi_0\rangle$ and excited state $|\Psi_1\rangle$ for
weak and strong (antiferromagnetic) impurity-superconductor coupling J. At
critical coupling J_{crit}, i.e. when the YSR resonance energy ε crosses zero, a first
order quantum phase transition occurs between free and screened impurity spin
state with quasiparticle spin $S_{\mathrm{QP}} = 0$ and $S_{\mathrm{QP}} = -1/2$, respectively, exchanging
their role as ground and excited state. Figure adopted from Heinrich *et al.*[64]

2.2 Quantum spins at superconductor surfaces probed by STM

Early experiments with paramagnetic impurities in superconductors showed that T_{c} grad-
ually decreases with increasing impurity concentration, eventually suppressing supercon-
ductivity in favor of a paramagnetic or ferromagnetic phase[91]. Tunneling experiments
with superconductors between metal plates could verify ideas of the BCS theory showing
effects of magnetic impurities on the quasiparticle spectrum spatially averaged over the
whole superconductor[92].

However, while the elaborate theory on localized single impurities outlined in the pre-
vious section was formulated already in the 1960's shortly after publication of the BCS
theory, experimental techniques at that time had very limited means to put them to test.
Only the development[93] and advances[94] of scanning tunneling microscopy (STM) gave
researchers the possibility to access physical properties like the electron density of states
at the atomic scale. It became possible to measure clean surfaces prepared in ultra-high
vacuum at the temperature of liquid helium to improve the energy resolution below 1 meV,
so that in 1997 enhanced spectral intensity inside the superconducting gap around single
Mn and Gd atoms adsorbed to an *in vacuo* prepared superconducting Nb crystal sur-
face at 4 K could be observed[14]. Another ten years passed before the next investigation
of YSR states were published observed around Mn and Cr adatoms on superconduct-

ing Pb[95,96], invigorated by new STM technical standards like commercial instruments reaching 400 mK temperature and combined with the use of a superconducting tip probe, demonstrating ultra-high energy resolution of ∼ 0.1 meV. That way, Franke *et al.* were capable to experimentally trace the coexistence and competition of magnetic and superconducting coupling mechanisms as well as the two ground states (see section 2.1.3) determined by the balance of Kondo screening and pair-breaking interactions[15]. The intrinsic potential to achieve ultimate energy resolution limited only by energy exchange of tunneling electrons with the electromagnetic environment[97], at that on the nanometer scale, makes STM the perfect tool to study atomically localized effects happening within the small energy intervals typical for superconductivity.

However, the true awakening of wide experimental interest in this field of research happened 2013 when "easy-to-build easy-to-detect scheme[s] for realizing Majorana fermions"[6] were proposed, following the seminal work of the so-called *Kitaev*-chain[98] and giving prospects to make quantum computation more fault-tolerant[5,56]. Hybridization of YSR states in ferromagnetic or helical spin wires was identified as a viable route to topological superconductivity with p-wave pairing, thus regarded as spinless, and hosting Majorana zero-energy boundary modes[6–9,74,99–101]. Shortly after, enhanced zero-bias intensity at the end of self-assembled Fe chains on a Pb single crystal could be observed and were interpreted as signatures for Majorana zero modes in agreement with theoretical predictions[32]. Whether these findings evidence the observation of Majoranas is a matter of debate in the community[33]. Anyhow, although an elegant way of creating ferromagnetic wires on Pb where it is unfeasible to use tip atomic manipulation, the self-assembly approach strictly limits the experimental parameter space and gives rise to clustering of surface contaminants at the adatom chain, creating disorder and uncontrollable variables in the experiment.

In order to get a fundamental understanding of the problem and with the goal to effectively manipulate YSR states to create topological in-gap bands, ultimately to realize braiding concepts for Majorana modes[5,102], it is inevitable to take a step backward and to start with in-depth investigations on single impurities. Combining theoretical analysis with measurements of isolated Mn adatoms on Pb(111), specific sub-gap features like Andreev reflections and YSR peak thermal replica were characterized as relaxation and excitation channels for the STM tunneling current[16]. Eliminating all such spectral features by measuring at outrivaling low temperatures and in the single-electron current limit, recently, direct tunneling between YSR states was demonstrated and finding the relative spin orientation between them freely rotating down to 7 mK[30]. Researchers found even more information in the sub-gap structure arising from Cooper pair instead of quasiparticle tunneling[103], the so-called Josephson effect[104], and directly demonstrated, atomically resolved, a weakening of the superconducting pairing interaction around magnetic impurities by reduced Josephson current between Pb tip and Pb(110) substrate[105].

Further, the already mentioned quantum phase transition, fundamentally intriguing and relevant also for the emergence of topological superconductivity, has been intensively studied and controllably crossed using the spin anisotropy in Mn-phthalocyanine molecular arrays on Pb(111)[106,107], the attractive force of the STM tip on Fe-porphyrin molecules[19,20] or varying the normal state conductance having a magnetic impurity on a superconducting vanadium tip on V(100)[108].

It was again on the Pb(111) substrate where invaluable insight into the spatial shape of YSR states was obtained, ascribed to atomic d-orbitals of the transition metal elements Mn[17] and Cr[21]. The orbital nature of spatially resolved YSR states became very clear despite the influence of the substrate crystal field that lifts degeneracy and modifies their shape in correspondence with the substrate Fermi surface. It further supported the identification of multiple bound states on one impurity, each related to an individual orbital with non-vanishing magnetic moment coupled to the superconductor and creating a scattering channel for quasiparticles.

In contrast to the observed orbital shapes within barely 1 nm radius, theoretically expected was a lateral extend of the YSR wave function comparable to the superconducting coherence length. It turns out that the direct trace of the decaying wave function is only detectable under certain conditions. It has indeed been observed for Mn on Pb(111)[17] up to 4 nm along certain crystallographic directions due to focusing effects of an anisotropic Fermi surface[109,110]. Probably the best way to visualize the long range oscillations of YSR wave functions is to use a quasi 2D superconductor like NbSe$_2$[24] or a proximitized La(0001) layer with intrinsic magnetic impurities[27]. An anisotropic Fermi surface combined with reduced dimensions available for decay, i.e. changing the lateral factor $1/k_\mathrm{F}r$ (3D) to $1/\sqrt{k_\mathrm{F}r}$ (2D), allowed for the observation of phase shifted particle and hole parts up to several tens of nm away from the embedded impurity sites.

A natural consequence of the lateral extend is an interaction of the impurities by overlap and hybridization of their YSR states. It results in a shift of YSR energies and a split into bonding and antibonding states. Moreover, it can mediate magnetic exchange as a form of RKKY interaction. Such coupling was studied for Mn dimers on Pb(111)[18], Co-phthalocyanine on NbSe$_2$[23], Cr adatoms on β-Bi$_2$Pd[22], Gd adatoms on a six monolayer proximitized Bi film on Nb(110)[111] and Mn adatoms on Nb(110)[29].

Among the above mentioned experiments on impurity dimers, only the first was done without employing atomic manipulation with the STM tip. This technique was first demonstrated in 1990[112] and is perfectly suited, in contrast to self-assembly methods, for a bottom-up approach to study artificially and precisely designed adatom configurations and to tailor their, i.e. magnetic, properties[90,113–115]. However, not on every substrate it is feasible since the adsorbates need to be sufficiently decoupled from the substrate in order to move them. For example, Pb has a large superconducting gap well suited to study YSR states, yet the cohesive energy between lattice atoms is relatively weak so that

adsorbates relax deeply into the surface unable to move without damaging the surrounding substrate lattice. Similarly, weakly coupled layers in Van-der-Waals materials make them less favorable for atomic manipulation since flakes of substrate material itself can be drawn to the STM tip. Therefore, the trend for investigating adatom nanostructures consisting of multiple impurities went towards substrates that allow rather easy adatom manipulation, initially forcing experimentalists to make compromises regarding the gap size or surface defects.

Most experiments performing atom-by-atom construction of spin chains on superconducting surfaces have been published very recently, bearing high hopes to finally find unambiguous evidence for Majoranas and to be capable of manipulating them. Although suffering from aforementioned drawbacks regarding gap size, exploring Fe chains on oxidized Ta[34] and Fe+Co chains on Re[35] paved the way for manipulating end states of proximitized magnetic chains, being of trivial or topological origin. Even on the layered NbSe$_2$ chains assemblies have recently been realized[38], taking advantage of the slow spatial decay of YSR states in 2D superconductors to craft dilute impurity chains that retain their quantum nature while a sufficient YSR hybridization is ensured. Ultimately, however, the presence of the well-known NbSe$_2$ charge density wave, despite exhibiting interesting effects, is a limiting factor for the controlled parameter tunability of herein assembled chains.

Finally in 2019, the preparation of sought-after clean Nb(110) surfaces was demonstrated[116] and made the highest-T_c elemental superconductor available as a substrate which combines a large gap (Δ = 1.53 meV) and easy atomic manipulation, featuring an anisotropic Fermi surface and Type-II behavior in external magnetic fields. Since then several groups focused on Nb(110), depositing Mn[28,29,36,37] and Fe[31,39] adatoms on the surface. Momentum resolved analysis of the close-packed ferromagnetically coupled Mn chain along the crystallographic [001] direction[28] was found to exhibit a topologically non-trivial p-wave gap[36] providing strong indications for the realization of topological superconductivity. Recently, a substrate spin-orbit-coupling dependence was investigated by direct comparison of Mn atoms on Ta(110) and Nb(110)[117,118].

The latest reviews and studies on the progress of finding topologically protected zero-bias end modes in spin chains on superconductors[40,41,64,119,120] acknowledge accumulating evidence for Majorana zero modes, ultimately conclude that there are still many open questions and a long way to go before these first steps can bear fruit in the application for quantum computation.

As a final remark, predictions for topological boundary modes in two dimensional magnetic nanostructures coupled to superconductors[25,121–124], even proposals for Majorana state manipulation[102], have been thought of, however, so far they were not experimentally investigated on artificially crafted assemblies.

3 Methods

This chapter will mainly cover experimental techniques used in this work and provide a brief description of the numerical calculations that yielded valuable insight to interpret experimental results. After a basic introduction to scanning tunneling microscopy (STM), essential features of the employed laboratory system shall be presented including the cryostat and ultra-high vacuum (UHV) components indispensable for surface science. Next, for the present work particularly important tip functionalization methods will be shown together with examples of their respective effect on STM measurements. After that, the process of sample preparation, including *in situ* surface cleaning, adatom deposition as well as atomic manipulation, will be explained in detail. Finally, theoretical methods employed by collaborators from Forschungszentrum Jülich and University of Basel shall be mentioned without going into detail.

3.1 The scanning tunneling microscope

The idea of STM dates back to the 1980s when Binnig and Rohrer at IBM Zurich observed electron tunneling between a sharp tungsten tip and a platinum sample in vacuum[93]. Quick advancement as a tool to study conductive solid matter sensing structural properties with ultra-high resolution lead to the Nobel prize 1986 awarded to its developers. The widespread fascination for STM stems from visualizations of physical properties in real space and on the nanometer scale, i.e. atomic lattices, oscillations of interfering electronic wave functions, magnetic textures to name just a few, the precision to characterize single atoms and molecules, only outrivaled by the ability to manipulate and move them in order to craft self-designed artificial nanostructures. The working principle, aside from the classically unthinkable quantum mechanical tunneling effect, is not hard to understand and became an inspiration to numerous scanning probe microscopy (SPM) techniques. Yet STMs are complex machines that could only succeed through engineering ingenuity, combining utmost vibrational decoupling from the environment and sophisticated electronic low-noise circuitry sensing currents on the femto scale, not least to mention the enormous effort necessary to reach sub-Kelvin temperatures at the tip-sample junction for ultimate energy resolution. Despite limitations with regard to sample conductance and surface roughness, it can be operated not only in vacuum but also in air or even in liquid, a general advantage of SPM compared to other common ultra-high resolution scanning

microscopy techniques using electron currents like scanning electron (SEM) and tunneling electron (TEM) microscopy. Offering a rich workbench of spectroscopy techniques probing electronic, magnetic, even optical properties etc., makes STM a powerful tool for interdisciplinary research. Aside from being a natural choice for solid state physics, it is attractive for surface characterization on chemistry and biology samples as well. Nowadays, ultra-low temperature ultra-high vacuum STM systems are commercially available making nanoscale high-energy resolution measurements a research standard.

3.1.1 Working principle

Detailed descriptions about STM and other scanning probe methods can be found in various literature[125,126] as well as condensed summaries[127,128]. Here, a short introduction to the basics of STM shall be given, focusing on essential aspects for the interpretation of results presented in chapter 4.

Tunneling junction

The tunneling effect is one of the most prominent quantum mechanical phenomena. Often metaphorically depicted as macroscopic objects going through walls, it applies however only to microscopic particles like electrons. Their position in space is given by a probability amplitude $|\Psi(\boldsymbol{r})|^2$, determined by their wave function $\Psi(\boldsymbol{r})$, which can be rather smeared out, e.g. around atomic nuclei referred to as electron orbitals. At the interface of a metal to an insulator, i.e. vacuum, electrons in the metal with the Fermi energy E_{F} would usually need an energy supply given by the work function Φ to exit the metal and enter vacuum. Otherwise their probability amplitude decays exponentially away from the metal surface. If, however, within this exponential tail another metal is present which offers unoccupied electronic states at the corresponding energy, there is a non-vanishing probability that the particle can cross the vacuum barrier without losing energy. For very small distances z between both metals and with an applied potential difference, or bias voltage U_{t}, this results in a detectable electrical current I_{t} between both electrodes without mechanical contact or any electrons actually existing in the vacuum in between. One can say they remain quasiparticles, leaving one crystal band structure and entering another without ever being free electrons. From the above considerations, the following assumptions about the tunneling current can be made: (i) it depends exponentially on z, (ii) particles tunnel only within the energy window where occupied states on the one and unoccupied states on the other side overlap, determined by E_{F} and $E_{\mathrm{F}} + eU_{\mathrm{t}}$ (e is the elementary charge) and (iii) it depends on the number of available states on each side, i.e. the energy dependent density of states $\rho(E)$.

A quite general situation is depicted in figure 3.1 with a tunneling junction between metallic tip and sample with non-trivial density of states. In the following, indices for
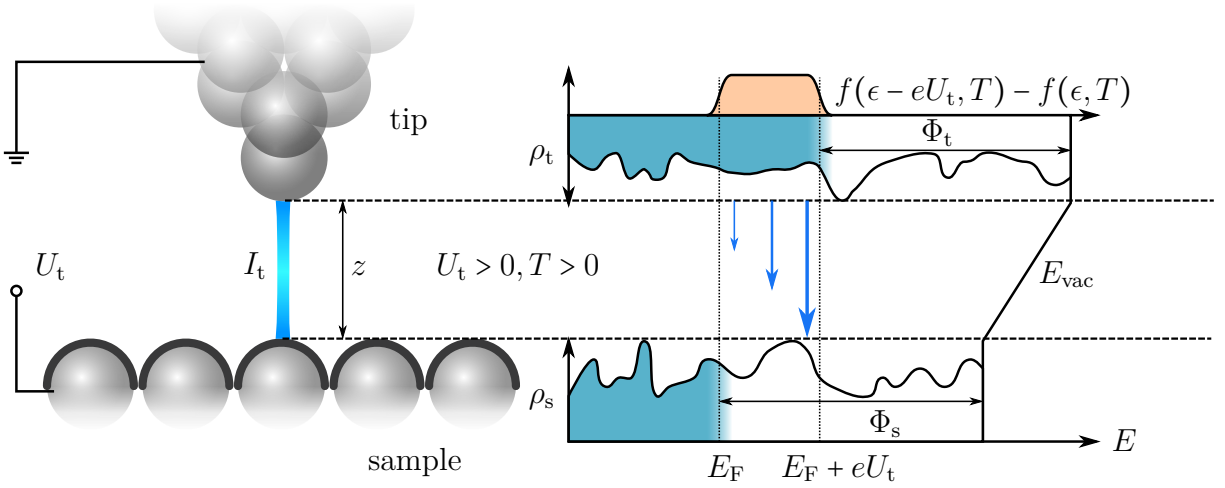
Fig. 3.1: **STM tunnel junction:** A bias voltage U_t between metallic tip and sample results in a measurable tunneling current I_t for small tip heights z. Example density of states $\rho_t(E)$ and $\rho_s(E)$ for tip and sample, respectively, are occupied up to the Fermi level E_F which has the offset eU_t between tip and sample. Electrons tunnel elastically from occupied to unoccupied states within the energy interval framed by the temperature dependent Fermi functions $f(E,T)$ through the vacuum barrier with E_{vac} over the work functions Φ_t and Φ_s.

bias voltage and tunneling current will be omitted, indices t and s for tip and sample, respectively, are used, and $\epsilon = E - E_F$. The tunneling current can be calculated by first-order perturbation theory to[129]

$$I = \int_{-\infty}^{\infty} d\epsilon \, \rho_s(\epsilon)\rho_t(\epsilon - eU) \times [f(\epsilon - eU, T) - f(\epsilon, T)] \times \mathbb{T}(z, \epsilon, eU, \Phi_{eff}, \Psi_s, \Psi_t). \qquad (3.1)$$

The first factor is a convolution of tip and sample density of states. The second defines the energy window for the integral with the Fermi function $f(E,T) = (1 + \exp[E/k_B T])^{-1}$, which is essentially a step function with values $f(\epsilon < 0) = 1$ for occupied states, $f(\epsilon > 0) = 0$ for unoccupied states and $f(\epsilon = 0) = 1/2$, however, the step is progressively smeared out with increasing temperature T, allowing unoccupied states below the Fermi level and vice versa. The third factor is, what makes the situation more complicated, the tunneling matrix element or transfer function $\mathbb{T}$ and includes a weighting of the integral with respect to energy, the exponential z-dependence and other geometrical factors like the shape of tip and sample as well as the wave function distributions of tip and sample states participating in the tunneling process. An analytical solution for $\mathbb{T}$ can only be obtained by simplification through assumptions about the system. For example, in a one-dimensional case, it can be written as

$$\mathbb{T} = \exp\left[-2z\sqrt{\frac{m_e}{\hbar^2}\Phi_{eff}}\right] \qquad \text{with} \qquad \Phi_{eff} = \Phi_t + \Phi_s - (2\epsilon - eU) \qquad (3.2)$$
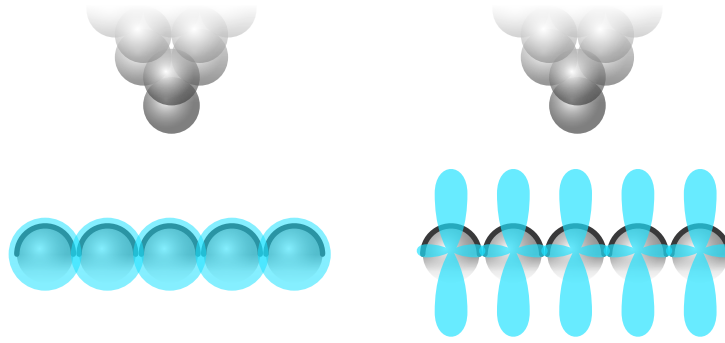
Fig. 3.2: **Wave function geometries:** Intuitive picture of s-(left) and d_{z^2}-level (right) states on sample atoms. The d_{z^2} geometry reaches farther into vacuum and favors atomic resolution. Figure adapted from C. Julian Chen[131].

with the free electron mass m_e. The z-dependence is recovered and the integral 3.1 is weighted with respect to energy so that the highest contribution is obtained for the maximum ϵ possible, corresponding to the Fermi level of sample or tip for $U < 0$ and $U > 0$, respectively. This is suggested in figure 3.1 with different sizes of the blue arrow that indicates elastic electron tunneling. As a consequence, this means that for high bias voltages $eU \lesssim \Phi$ information about the energy dependent density of states is obtained with higher signal in the unoccupied states in both directions. As a consequence for real measurements when the sample DOS is of interest, results at positive bias yield a more accurate projection whereas at negative bias the highest contribution comes from the sample's Fermi level and the tip DOS has bigger influence. In the limit $eU \ll \Phi$, variation of $\mathbb{T}$ with ϵ can be neglected.

A more practical assumption for STM application is a sharp tip, which after all determines the lateral resolution of the microscope, featuring a single atom on the apex which is solely responsible for the tunneling current due to the exponential z-dependence. It can be modeled by an s-orbital-like spherical shape at $\boldsymbol{r}_0$ with radius R[130]. Further simplifying by setting zero temperature $T = 0$, constant tip density of states $\rho_{\text{t}}(\epsilon) = \rho_{\text{t}}(0)$ and considering the low bias limit, the tunneling current condenses to

$$I = C \int_0^{eU} d\epsilon \, \rho_{\text{s}}(\epsilon, \boldsymbol{r}_0) \tag{3.3}$$

with $C = \text{const}$. $\rho_{\text{s}}(\epsilon, \boldsymbol{r}_0)$ is the *local density of states* (LDOS) of the sample at the position of the tip. Note that

$$\rho_{\text{s}}(\epsilon, \boldsymbol{r}_0) = \sum_\nu |\Psi_{\text{s},\nu}(\boldsymbol{r}_0)|^2 \delta(\epsilon_\nu - \epsilon) \quad \text{with} \quad |\Psi_{\text{s},\nu}(\boldsymbol{r}_0)|^2 \propto \exp\left[-\sqrt{\frac{8m_e\Phi}{\hbar^2}}(z+R)\right] \tag{3.4}$$

retains the exponential z-dependence.

Finally the influence of wave function geometries shall be discussed based on a, not

accurate but intuitive, picture shown in 3.2. The example of atomic s- and d_{z^2}-levels are shown on the sample side, $|\Psi_{s,s}(\boldsymbol{r})|^2$ and $|\Psi_{s,d}(\boldsymbol{r})|^2$, respectively. Assuming equal tip-sample distance and non-local density of states, i.e. $\int d\boldsymbol{r}\,|\Psi_{s,s}(\boldsymbol{r})|^2 = \int d\boldsymbol{r}\,|\Psi_{s,d}(\boldsymbol{r})|^2$, their separate contributions to the tunneling current would be different: $I_s < I_d$, just because the d_{z^2} state has a larger extension in the z-direction, i.e. into the vacuum between the electrodes. In particular, the long and thin shape of a d_{z^2} orbital favors the resolution of single atoms in STM which can be intuitively grasped from figure 3.2 and has been shown by theory[131]. This is equally valid for the orbital wave function at the tip apex and is crucial for ultimate lateral resolution, e.g. with a tungsten tip which is a d-shell metal.

Reducing noise

One of the biggest challenges that has to be faced in experiments is noise of vibrational and electronic origin that would render STM operation impossible if not strongly damped. Especially floor vibrations, acoustic and electromagnetic noise have to be considered. By mechanical decoupling from the environment, z-noise can be very effectively reduced to the order of 1 pm. In short, the combination of a rigid STM head mechanically connecting tip to sample stage and a suspension with long springs results in strong damping of both low and high vibrational frequencies, respectively. On the electronic side, sophisticated STM controllers are constructed especially for low-noise application. The ground-potential must be well distributed in order to avoid ground loops, i.e. by individual direct connections from all electronics to a central mass. Moreover, voltage signals entering the microscope system should be low-pass filtered and wires effectively shielded, e.g. by coaxial cables. Finally the outgoing current signal is amplified as close as possible to the STM junction by the so-called preamplifier usually attached directly to the STM system. It converts I_t into a voltage signal. This reduces the noise level and facilitates detection of tunneling currents around 1 pA.

Scanning operation

The above repeatedly highlighted relation $I \propto e^{-\kappa z}$ ($\kappa =$ const.) is responsible for the incredibly high topographic sensitivity of the STM. For typical metallic work functions, 1 Å tip height difference changes the tunneling current by an order of magnitude resulting in sub-picometer vertical resolution. A sufficiently sharp tip scanning the sample surface can thereby easily detect mono-atomic steps and even the protrusions of individual atoms inside the surface lattice.

To move the tip over the surface it is mounted on a tube exhibiting the piezoelectric effect translating an applied voltage into spatial extension or contraction. Electrodes are attached in a way that three separate high voltage supplies can control x, y and z co-

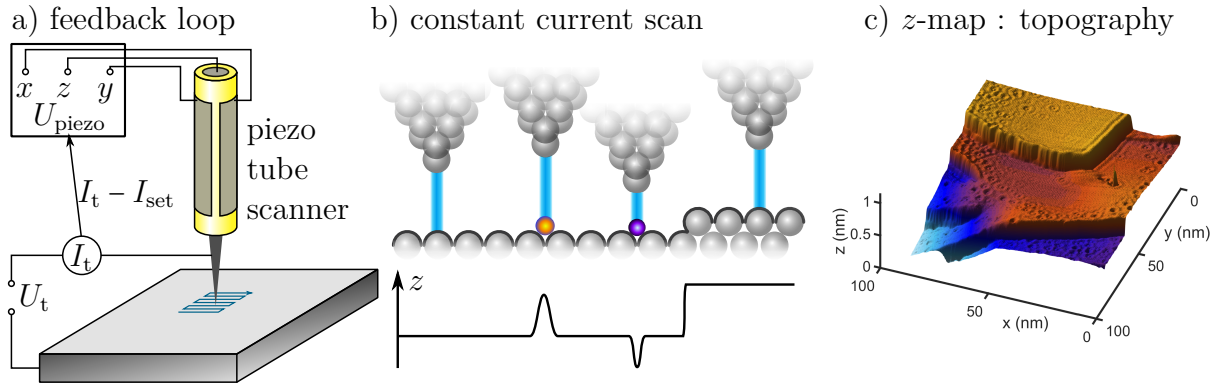a) feedback loop   b) constant current scan   c) z-map : topography

Fig. 3.3: **Scanning operation: a** The STM tip is mounted on a piezo tube scanner. An electronic real-time feedback loop compares the measured tunneling current I_t to the setpoint I_set and gives a corresponding voltage to the z-electrode of the piezo tube. x and y electrodes are used to scan the tip over the sample surface. **b** Constant current mode: the tip is moved along a line on the sample while the feedback controls z to keep $I_\mathrm{t} \simeq I_\mathrm{set}$. Adsorbates can either enhance or reduce ρ_s in the relevant energy interval, appearing as protrusion or depression, respectively. **c** A two dimensional matrix of recorded z-values generates a topography map, here a 100x100nm area on Ag(111) with mono-atomic steps. Notice that electronic effects appear in topography as well (Friedel oscillations).

ordinates individually and with sub-picometer precision[1]. Before the tip is in tunneling contact to the sample, which happens only at distances in the order of $z \sim 1\,\mathrm{nm}$ for measurable currents well above the noise limit ($I \sim 30\,\mathrm{pA}$), it requires a controlled approach. This is done by a coarse motor moving the whole tube scanner in steps smaller than the z-range of the tube. In most cases the coarse motion is realized by piezo stacks in so-called slip-stick operation. After each coarse step the scanner sweeps the whole z-range before the coarse motor continues. This is repeated until a tunneling current is established. In order to stabilize the z position of the tip, a fast electronic feedback controls the z scanner voltage such that the tunneling current is kept at a certain setpoint.

An image of the surface topography is then usually acquired in the so-called constant current operation depicted in figure 3.3. The x and y piezo voltages produce a raster movement of the tip over the sample surface where a 2D area is scanned line-by-line along which is the fast scan direction ($\sim 100\mathrm{nm\,s^{-1}}$). At any time, the feedback aims to stabilize I_t around I_set by acting on the tip height z. For very fast scan speeds the feedback might not react fast enough to avoid mechanical contact between tip and sample so that an appropriate choice of operation parameters is essential. An example line profile of tip height z is sketched in figure 3.3b. An atomically flat surface is scanned featuring two adsorbates of different species and a mono-atomic step. As long as the sample density of states does not change locally and the tip is a point probe, the topographic structure

---

[1]It is also possible to mount the sample on a tube scanner instead.

of the surface is caught exactly. However, chemically different defects can change the LDOS such that a topographic protrusion might even appear as a depression in the z-profile. There are generally many possible effects that spatially modulate the LDOS and become visible in STM images. For example, scattering at steps and defects of surface state quasiparticles in Ag(111) lead to Friedel oscillations[132] like seen in figure 3.3c. The computer generated image corresponds to a 2D matrix of recorded z values during an STM constant current scan referred to as topography.

Spectroscopy

It became clear that by changing the bias voltage U one can control at which energies around the Fermi level electronic states of tip and sample contribute to the tunneling current I. Therefore, measuring how much the current varies with an incremental change dU, i.e. dI/dU, should yield information about energy dependent local density of states on the sample. That is the main interest of *scanning tunneling spectroscopy* (STS). Taking equation 3.3, then obviously $\partial I/\partial U(eU) = C\rho_s(eU, \boldsymbol{r}_0)$, i.e. dI/dU is directly proportional to the sample density of states. However, for real measurements this might be oversimplified. Therefore the derivative of equation 3.1 shall be analyzed by staying in the low-bias limit:

$$\frac{\partial I}{\partial U} = -\mathbb{T}\int_{-\infty}^{\infty} d\epsilon\, \rho_s(\epsilon) \left\{ \frac{\partial \rho_t(\epsilon - eU)}{\partial U} \left[f(\epsilon - eU) - f(\epsilon) \right] + \rho_t(\epsilon - eU)\frac{\partial f(\epsilon - eU)}{\partial U} \right\}. \quad (3.5)$$

From there, again assuming the desirable scenario of ρ_t = const., $\partial \rho_t/\partial U$ vanishes and what remains is a convolution of ρ_s with $\partial f/\partial U$. The derivative of the Fermi-Dirac distribution corresponds to a peak around eU with its width depending on T. Therefore this yields basically ρ_s broadened by finite temperature. If $T = 0$, then $\partial f/\partial U$ becomes a $\delta(\epsilon - eU)$ and again $dI/dU \propto \rho_s$. This ideal scenario is of course never reached in experiments. In order to get accurate information about the sample electronic structure with best possible energy resolution, STM measurements are done at lowest possible temperature and the tip is usually prepared and characterized before the measurement. If ρ_t and T are known, one can numerically calculate a matrix that corresponds to the expression in braces in equation 3.5:

$$A_{ij} = \frac{\partial \rho_t(E_j - eU_i)}{\partial U} \left[f(E_j - eU_i) - f(E_j) \right] + \rho_t(E_j - eU_i)\frac{\partial f(E_j - eU_i)}{\partial U}. \quad (3.6)$$

Then the convolution is evaluated by a matrix multiplication of A_{ij} with a column vector $[\rho_s]$ and a measured dI/dU signal can be deconvoluted like

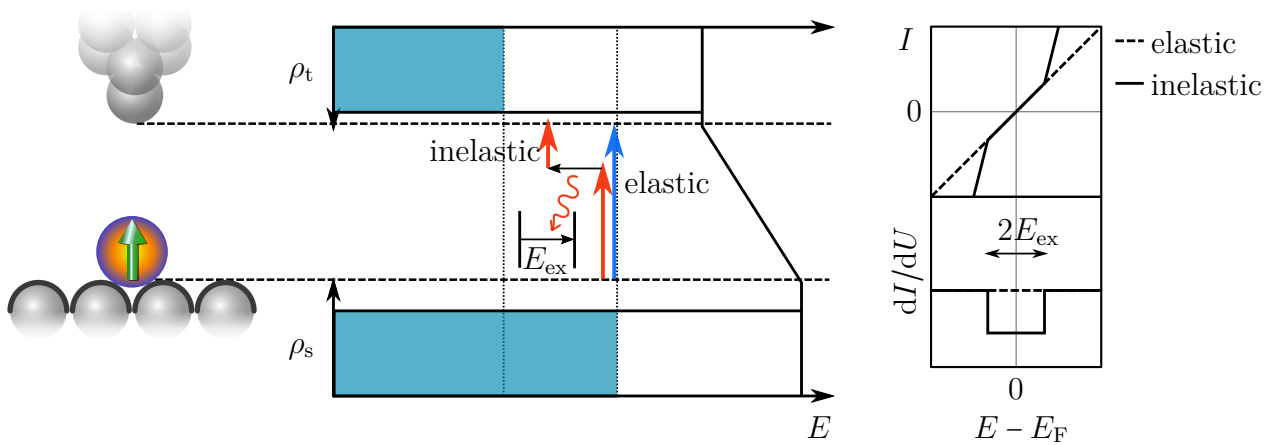$$[\rho_s] \sim A_{ij}^{-1}\,[dI/dU]. \quad (3.7)$$

Fig. 3.4: **Inelastic tunneling:** Excitation of spin-flip events in magnetic adsorbates with energy E_{ex} can lead to inelastic tunneling giving an extra contribution to the current. Tip and sample DOS are assumed constant and $T = 0$. Purely elastic (dashed line) and combined elastic and inelastic spectra (solid line) are compared. The latter shows two symmetric steps around E_F in dI/dU.

However, exact knowledge of the tip density of states is nearly impossible so that a deconvolution is often not very useful. Still, the numerical convolution can be used to simulate effects of different tips that might produce very useful results. This will be shown in section 3.2 about the preparation of tips.

Further, in addition to hitherto considered elastic tunneling, electrons can also partly lose their energy during a tunneling process by exciting a state existing between tip and sample states, referred to as inelastic tunneling. Those states can be vibrational modes, e.g. in a molecule on top of the sample surface, or spin-flip events in magnetic adsorbates. In the simplest picture shown in figure 3.4 with non-saturated relaxation paths, this affects the dI/dU spectroscopy measurement by introducing step-like increases symmetrically around the Fermi level when the excitation energy E_{ex} is overcome. Much more complex scenarios are possible, potentially hampering data interpretation. In-depth studies can be found in the literature[133,134].

Data recording

In the following, the acquisition of spectroscopy data shall be explained. To obtain an I-U curve, first the tip is positioned at a desired spot on the sample surface and stabilized by the piezo feedback loop with parameters I_0, U_0. Then feedback is opened, z is held constant and the bias is ramped in linear steps while recording the current readout. After ramping the bias back to U_0, the feedback is switched back on.

Despite all efforts, a computational derivation of I in typical measurements leads to rather low signal-to-noise ratio which would necessitate lengthy averaging of numerous
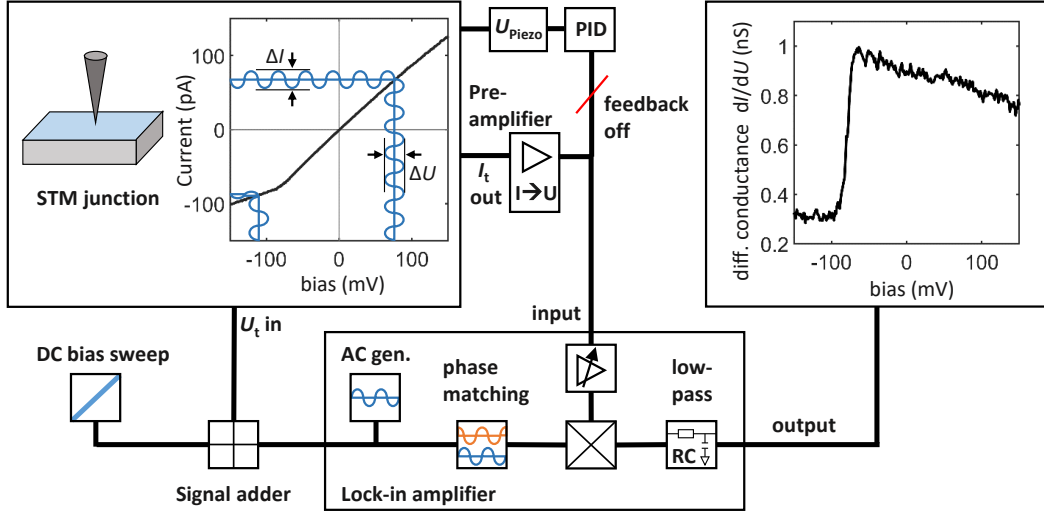
Fig. 3.5: **Signal detection in tunneling spectroscopy via lock-in technique:** Feedback control is turned off, tip height is held at initial stabilization parameters. Bias voltage is ramped to acquire an $I_t - U_t$ curve (upper left box). Lock-in: an AC modulation U_{mod} with frequency f_{mod} is added to the bias which modulates I_t with f_{mod}. Phase matching the resulting I_t signal with the U_{mod} reference and subsequent multiplication yields a DC signal proportional to dI_t/dU_t. A low-pass suppresses all higher frequencies to generate a low-noise dI/dU output signal. It is proportional to the sample LDOS, here the onset of the Ag(111) surface state around $\epsilon = -60\text{meV}$ is observed.

sweeps. Therefore it became STM standard to use the *lock-in* technique. It offers significantly enhanced signal-to-noise ratio and has the advantage of directly measuring dI/dU without data processing. A schematical picture of the lock-in principle is given in figure 3.5. Basically, the bias voltage becomes modulated by an added AC signal[2] U_{mod} which defines the interval $U \pm \Delta U/2$. The modulation is transferred to the tunneling current $I \pm \Delta I/2$ and shifts the desired signal in frequency space to f_{mod} where it is separated from uncorrelated signals. Multiplication with phase matched U_{mod} selectively picks the frequency f_{mod} in the power spectrum and shifts back to zero producing a DC signal proportional to $\Delta I/\Delta U$. Subsequent filtering of higher frequencies yields a low-noise dI/dU measurement. To successfully use the lock-in technique, two crucial factors have to be considered: (i) Capacitive coupling at the STM junction and parasitic capacities between wires produce out-of-phase components at f_{mod} so that a correct phase matching is essential. (ii) The variation of junction bias induces a lower limit for the energy resolution of approximately $e\Delta U$. Therefore it should be chosen appropriately so that $\Delta U \ll U_0$. Presented data in this work shall be labeled with respective parameters for U_0, I_0, ΔU.

The lock-in measurement additionally enables the simultaneous acquisition of dI/dU dur-

---

[2]The modulation frequency should be chosen to be much higher than the rate of piezo feedback control and below the preamplifier cut-off frequency. For this work it was always set to $\approx 730\text{Hz}$.

ing an area scan, thereby visualizing the sample LDOS at the energy given by eU in real space, so-called dI/dU maps. In flat areas, it can be helpful to switch off the feedback and operate in constant height mode. That way, z-induced intensity changes in the dI/dU signal can be avoided, referred to as the setpoint effect. Alternatively, a grid of full point-spectroscopy sweeps in one or two space dimensions can be taken acquiring full spectral information on a specific line or area. These powerful but lengthy measurements necessitate a great stability in x and y coordinates.

Energy resolution

In low-temperature STM the energy resolution in STS is crucial for the performance. If $\Delta U \ll U_0$ is fulfilled, the limit is given by finite junction temperature and remaining electromagnetic noise, e.g. coupling in from piezo voltages close to the tunneling junction or ground carrying 50 Hz mains frequency. In the sub-Kelvin regime they are often at a comparable level.

In conclusion, both the realization and interpretation of STM measurements is not straight forward and requires knowledge about the individual instrumental setup, data acquisition parameters and the different physical properties that influence the tunneling current. In turn, the variety of information about the sample that can be extracted is one of the big advantages of STM.

3.1.2 The laboratory system

For all presented experiments, a low temperature ultra-high vacuum (UHV) STM system has been used shown in figure 3.6. A commercial high-performance STM head from *Scienta Omicron* in the "Tribus"-design is installed into an *Oxford Instruments* bath cryostat featuring a 100L ^{4}He tank, 1 Kelvin pot and ^{3}He refrigerator[135,136]. This is schematically depicted in figure 3.7. It allows 6 days of measurement without interruption to refill helium at a base temperature of 1.9 K and roughly 8 h at 500 mK in ^{3}He single shot mode. Inside the helium tank superconducting solenoids are installed for applying external magnetic fields of up to 1 T in the measurement plane (B_{xy}) and up to 6 T out of plane (B_z).

The cryostat is connected to a UHV chamber. The whole insert can travel down via a motorized vertical manipulator into the UHV chamber where the thermal shield around the STM head is opened and a wobble stick is used to exchange tip and sample. In that position also *in situ* material deposition can be performed via two electron-beam evaporators directly shooting at the sample stage inside the STM.

Clean sample surfaces can be prepared using an ion gun for sputtering and e-beam heating stage inside a preparation chamber connected by a gate valve to the STM chamber. Epitaxial films can be grown using several e-beam evaporators. In order to preserve clean
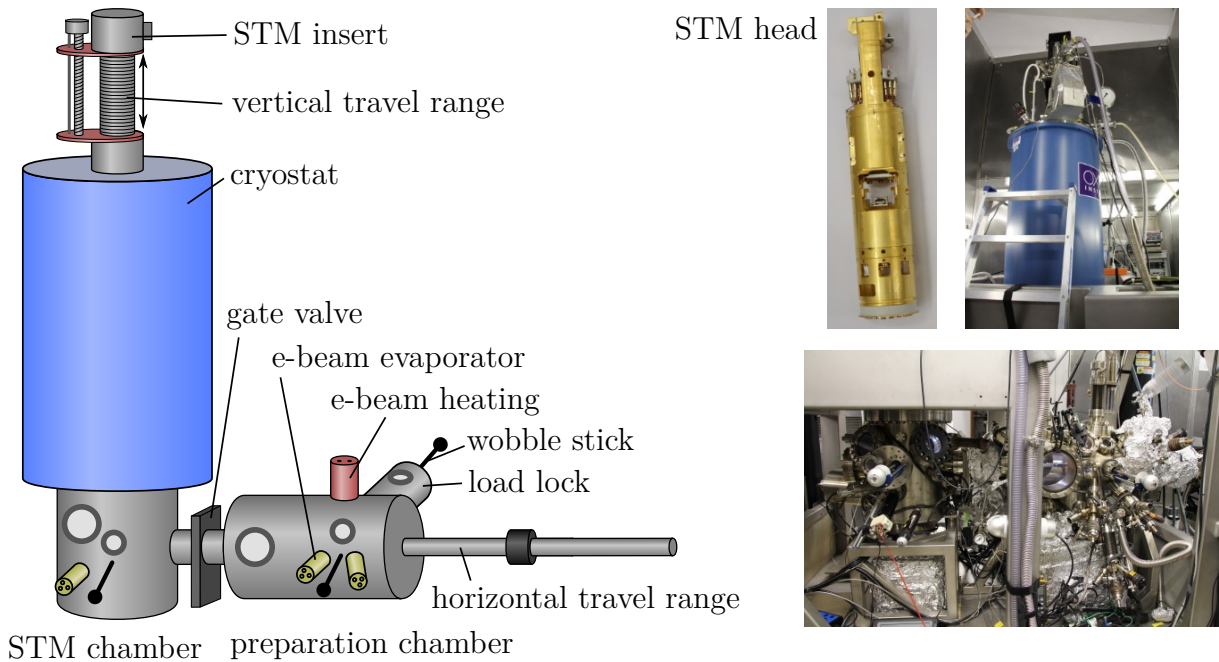
Fig. 3.6: **The UHV system:** Schematical view of the used laboratory system together with photographies of STM head, cryostat and connected UHV chambers for sample exchange and basic preparation. The whole system stands inside a housing for acoustical damping, on a separated flooring, and can be lifted by air damping legs for mechanical decoupling.

surfaces during transfer and measurement, ultra-high vacuum has to be maintained at all times. A combination of turbo molecular pumps, ion getter pumps and titanium sublimation pumps keep the pressure at around 3×10^{-10} mbar in both UHV chambers. The horizontal travel range was chosen specifically to reduce degassing during sample transfer. An additional small ion getter pump is installed on top of the cryostat to pump the long tubular volume inside which is thermally shielded by gate flaps at its bottom. The inner cryostat wall is thermally connected to the so-called UHV sock which is cooled by pumping on liquid helium below 4 K so that it creates a powerful cryo vacuum pump. The actual pressure around tip and sample during measurement is therefore expected to be significantly lower, ensuring that even reactive samples can be measured up to several months without notable contamination from adsorbates.

The STM is operated using the combined controller electronics and software package *Nanonis* sold by *SPECS*. Data analysis has been done using *MATLAB*.

3.2 Tip preparation

Large-scale laboratory systems are built in order to reach lowest possible pressure, temperature and to apply high magnetic fields, requiring much effort to reduce mechanical and electronic noise. Having achieved all that, eventually it is time to take a closer look at
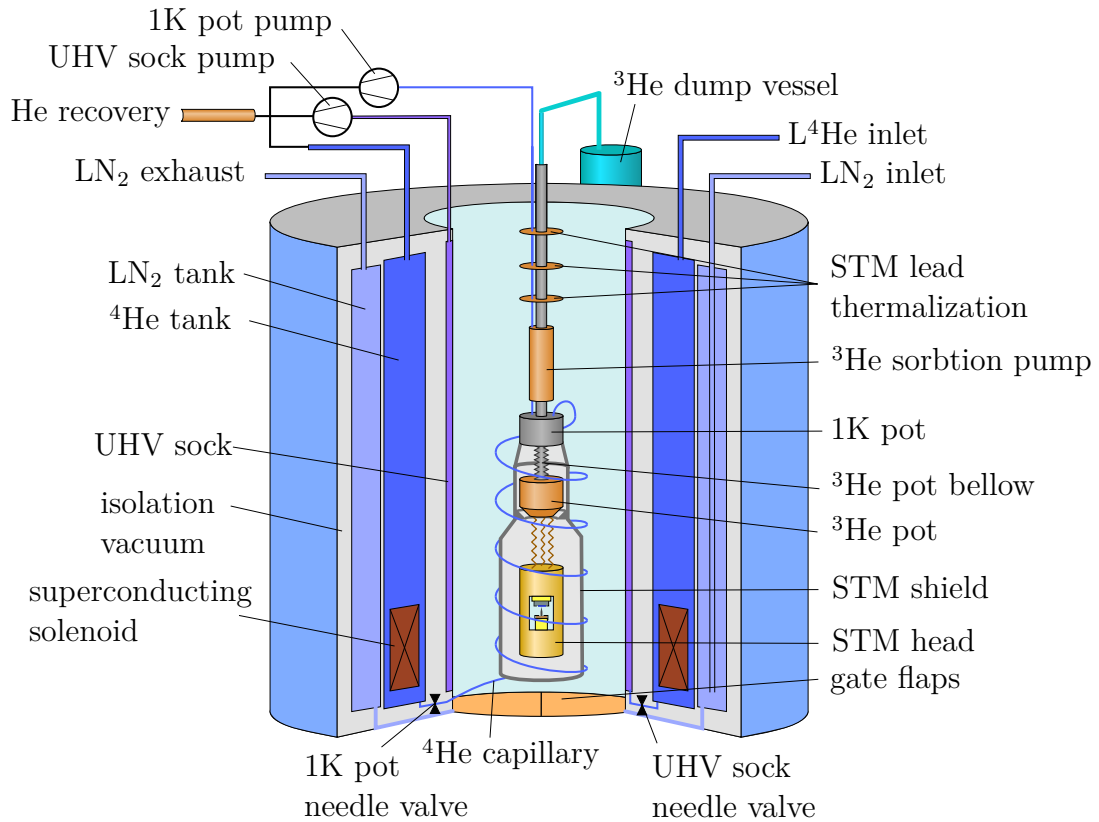
Fig. 3.7: **³He cryostat system:** ⁴He system: 100L bath cryostat provides LHe to UHV sock (directly at the inner wall to UHV) and 1K pot (connected to STM shield, sorption pump). Both are cooled below 4 K by combination of needle valve and pump. ³He system: ³He condenses in ³He pot (connected to STM head) cooled by 1K pot through STM shield. Sorption pump is held at 40 K by heating and keeps pressure in ³He volume high. When switching off heat, it cools down and pressure is reduced, causing bellow to contract, lifting thermal contact of ³He pot to shields. ³He evaporates and cooles ³He pot to 500 mK until it is empty after some hours. LN₂ provides thermal shielding against radiation from the side and below by cooled gate flaps. Heat load from STM leads is reduced by baffles in contact to the ⁴He exhaust capillary.
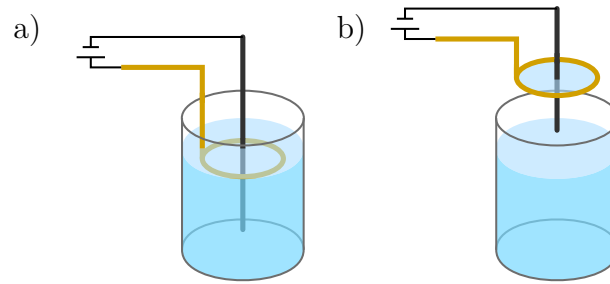
Fig. 3.8: **Making STM tips by electrochemical etching:** Metal wire is connected to a ring electrode by NaOH solution. Applied voltage leads to local etching and yields sharp tips. a) For tungsten wires placing the ring electrode inside the solution works fine. b) Cr rods could only be etched locally with a lamella of solution.

the actual microscopic tool to collect information about the sample surface, the tip probe. First, the geometrical shaping will be shortly discussed, before tip functionalization methods, acting on the tip density of states, shall be introduced, particularly superconducting and also magnetic tips.

It was pointed out previously that the ideal probe geometry is only a point in space, so that it should be made as sharp as possible in real experiments for good lateral resolution. The majority of tip probes in this work were made by electrochemically etching a tungsten wire[3] in 8 % NaOH solution and using a ring electrode immersed in the liquid. In order to make Cr bulk tips used for spin-polarized measurements, pure Cr rods have been etched which works much better, although more tedious, by using the lamella method (see figure 3.8) where only a thin section of the rod is in contact to the solution. Resulting tips are perfectly sharp under optical microscopes and even scanning electron microscopes (SEM) cannot distinguish the shape of the very last atomic cluster at the apex which is ultimately the decisive part for STM. Therefore probe characterization and also final shaping is best done *in situ* inside the STM head on well-known samples. Here, in the case of tungsten tips, the Ag(111) surface has been used (already shown in figures 3.3 and 3.5) which is rather easily cleaned to show atomic steps suited for testing the tip sharpness and features a Shockley-like surface state[137] producing a characteristic step in the otherwise quite featureless DOS close to the Fermi level. As an alternative to topography steps, single surface adsorbates are a good test for the apex shape. Anisotropic apex clusters distort surface features systematically like shown in figure 3.9a.

Feasible *in situ* preparation techniques on most metal surfaces are (i) short ($\sim 200\,$ms) bias voltage pulses of ± 3 to $\pm 10\,$V, (ii) poking the tip into the surface mechanically or (iii) picking up single atom or molecular (e.g. CO) surface adsorbates to the tip apex. The more frequently used methods (i) and (ii) are repeated until a satisfying quality is obtained. Figure 3.9 gives an example before-and-after tip shaping STM topography on

---

[3]Wires with 0.375 mm and 1 mm diameter have been used without significant differences.
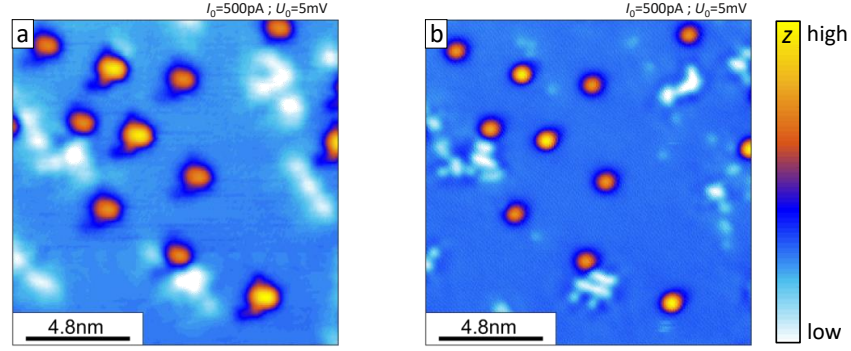
Fig. 3.9: **Shaping the tip *in situ*:** Two STM topography images of the same sample area containing several adsorbates. **a** Before and **b** after an intentional change of the tip apex shape induced by bias voltage pulse or picometer scale tip-sample mechanical contact (poke). Lateral resolution is significantly improved indicating a sharper and more sphere-like apex in **b**.

the same sample area.

Those methods are of course not restricted to topographic imaging quality, they can also influence the tip DOS. An energy independent ρ_t is often aimed for to obtain scanning tunneling spectroscopy (STS) dominated by the sample. Methods (i) and (ii) can be applied e.g. on Ag(111) until the dI/dU signal recovers the reference curve sufficiently well. However, in some cases it can be advantageous to intentionally manipulate the tip DOS, e.g. to gain spin-sensitivity or to improve the energy resolution beyond the Fermi-Dirac limit.

The latter is not quite intuitive and shall be clarified by an example. Consider a constant tip DOS with a delta peak at the Fermi level: $\rho_t(\epsilon - eU) = \rho_0 + \delta(\epsilon - eU)$. Then from equation 3.5 and using the relation $\int dx\, \delta'(x - x_0)F(x) = F'(x_0)$

$$\frac{\partial I}{\partial U} \propto \left(\frac{\partial I}{\partial U}\right)_{\rho_0} - \frac{\partial \rho_s(eU)}{\partial U}\left[f(0) - f(eU)\right] - \rho_s(eU)\frac{\partial f(eU)}{\partial U}\,. \tag{3.8}$$

The first term is the usual temperature broadened sample DOS. The third term gives only a temperature broadened peak around zero for non-vanishing sample DOS. The most interesting is the second term. It adds a contribution proportional to the derivative of the sample DOS while the Fermi functions only change the sign around zero. Remarkably, this contribution is not broadened, only damped around zero, by finite temperature and therefore breaks the Fermi-Dirac resolution limit. For the measurement with such a tip and a fictive sample DOS, the resulting dI/dU signal is compared in figure 3.10 to a standard constant DOS tip at two different temperatures using the numerical convolution matrix expressed in equation 3.6. A pair of peaks that is not resolved with the standard tip at elevated temperature retains the double-peak information with the delta-peak tip DOS. Such a tip surely does not exist, however, the example shows that any sharp peak
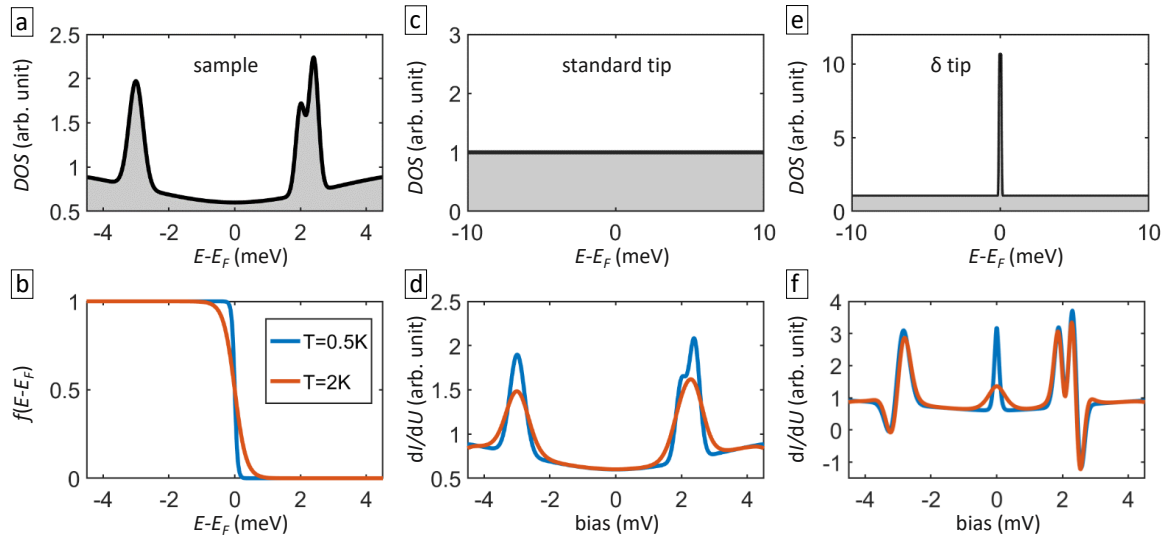
Fig. 3.10: **Tip DOS peak effect on STS: a** Fictive sample DOS with two peaks closeby. **b** Fermi function plotted for two different temperatures. **c** Energy independent constant tip DOS yields **d**, the numerical result for $\mathrm{d}I/\mathrm{d}U$ using this tip at two different temperatures. At $2\,\mathrm{K}$, the double peak cannot be resolved. **e,f** Tip DOS with δ peak at E_F and resulting $\mathrm{d}I/\mathrm{d}U$ signal. Temperature broadened peak at zero appears and peaks originating from sample DOS derivation are not broadened.

in the tip DOS can enhance energy resolution by partially circumventing temperature broadening. For peaks that are not at the Fermi level the whole sample DOS becomes shifted in $\mathrm{d}I/\mathrm{d}U$ by the difference[4]. Therefore to correctly interpret measured data, the exact knowledge of such impacting tip DOS features is crucial. Actually, this hypothetical situation is indeed similarly found when using superconducting tips which will be demonstrated in the following.

3.2.1 Superconducting tips

For all measurements with superconducting tips in this work, etched tungsten tips have been functionalized with a superconducting Nb cluster by deeply ($\sim$ µm) driving them into a Nb sample. An insufficient cluster size does not establish superconductivity, therefore this was repeated until approximately bulk-like gap size was detected. Nevertheless, shape anisotropy leads to slightly different density of states for each individually prepared tip, in particular different gap sizes $2\Delta_\mathrm{t}$. As outlined above, sharp quasiparticle coherence peaks at $\pm\Delta_\mathrm{t}$ improve the effective energy resolution for probing the sample DOS beyond the Fermi-Dirac limit by a formally temperature independent contribution[5]. Another advantage for probing with a gap is the vanishing density of states around zero which

---

[4]A peak in the unoccupied tip states only affects the occupied sample states and vice versa.

[5]The gap function itself is somewhat temperature dependent, however, sufficiently far below T_C the influence is small.
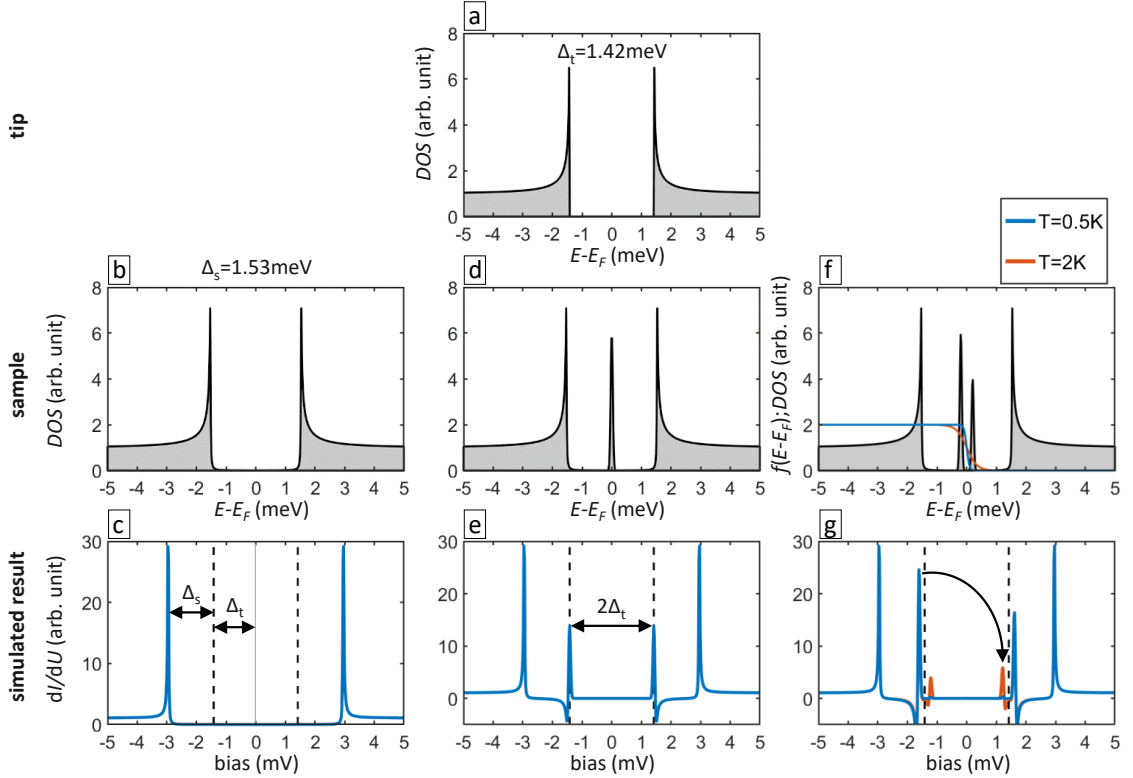
Fig. 3.11: **Simulating STS with a superconducting tip: a** Modeled tip DOS with 1.42 meV gap. **b,d,f** Model sample DOS for pure superconductor, additional peak at zero and two peaks symmetrically around zero, respectively. **f** plots additionally Fermi functions for 0.5 K and 2 K multiplied by 2. **c,e,g** Respective result of dI/dU signal simulation. **c** Coherence peaks shift to $\Delta_t + \Delta_s$, **e** zero bias peak is split to $\pm\Delta_t$ and **g** thermally excited states appear inside $\pm\Delta_t$ at $\pm(\Delta_t - \epsilon_0)$ as replica of states at $\mp(\Delta_t + \epsilon_0)$.

suppresses the first temperature broadened term. Additionally, all spectral features of the sample are thereby also shifted about $\pm\Delta_t$ away from the Fermi level.

According to the relevance of this aspect for the understanding of measurement data, the characteristic shapes in superconductor-insulator-superconductor (SIS) junction spectroscopy is presented in figure 3.11 from numerical simulation, before in figure 3.12 actual STS data is shown. Predicting the outcome by simulation is especially instructive since all input ingredients are known from equation 3.6. Superconducting gap functions are calculated using a Dynes-formula[138]

$$N(E) = \left| \frac{E - i\Gamma}{\sqrt{(E - i\Gamma)^2 - \Delta^2}} \right| \tag{3.9}$$

with a broadening factor Γ. Figure 3.11a depicts the modeled tip DOS with $\Delta_t = 1.42$ meV and $\Gamma_t = 0.1$ μeV. It probes a superconducting sample with $\Delta_t = 1.53$ meV and $\Gamma_t = 0.1$ meV having three different sub-gap structures plotted in panels b,d and f featuring a flat DOS, a Gaussian peak exactly at E_F and two peaks close to E_F, respectively. Below, the
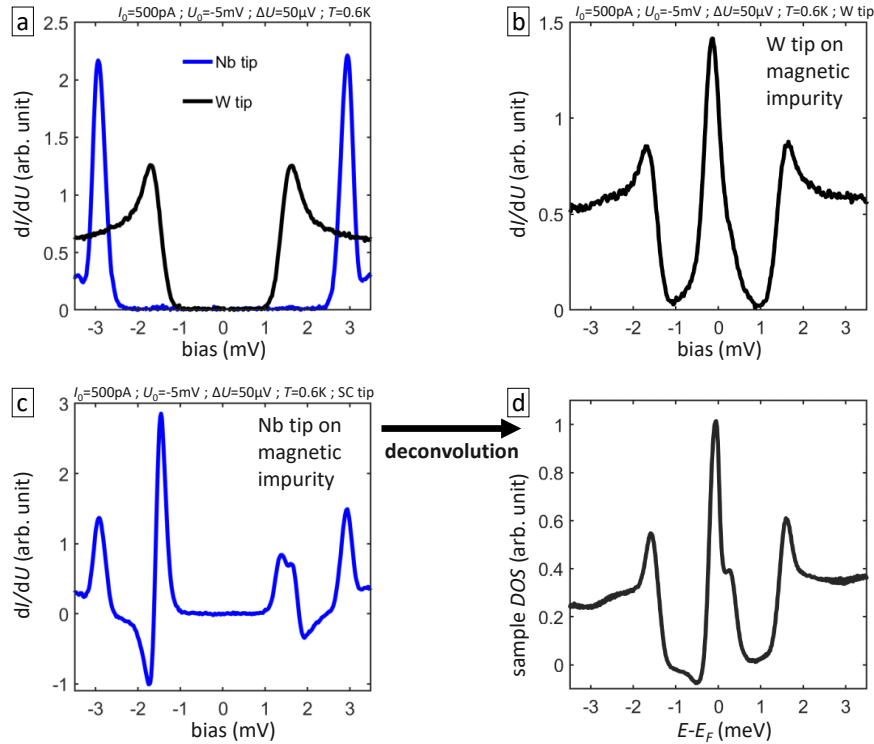
Fig. 3.12: **Metallic vs superconducting tip on superconducting sample with single magnetic impurity:** **a** STS on Nb away from impurities with tungsten (black) and Nb (blue) tip. **b** Metallic tungsten tip probing a magnetic Cr adatom showing in-gap YSR states. **c** Equivalent STS with superconducting Nb tip. **d** Result of deconvolution of **c**. Data was published on arXiv (2021)[139].

corresponding dI/dU signal is shown illustrating the effects described above. Note that due to the convolution involving sharp peaks dI/dU can become negative which is not interpreted as a (unphysical) negative density of states. Panel f,g further distinguish $T = 0.5\,\mathrm{K}$ and $T = 2\,\mathrm{K}$. States above the Fermi level can thereby be partially occupied and vice versa, giving rise to thermal replica peaks in dI/dU, i.e. peaks at $U = \pm(\Delta_\mathrm{t} - \epsilon_0)/e$ appear as replica of states at $U = \mp(\Delta_\mathrm{t} + \epsilon_0)/e$. Those vanish for $T \to 0$.

Measurement data on a superconducting Nb(110) with a superconducting Nb cluster at the tip yields results very similar to the presented simulation. It is compared to STS taken with a normal metallic tungsten tip in figure 3.12. The width of coherence peaks is predominantly limited by finite temperature and electromagnetic noise for the metallic and superconducting tip, respectively. Panel b shows STS taken on a Cr magnetic impurity with a tungsten tip. Within the Fermi-Dirac limited energy resolution it suggests an asymmetric peak around the Fermi level. The enhanced resolution of the Nb tip reveals at least one additional peak and clearly gives a means to quantify the particle-hole asymmetry of the overlapping YSR pair at the Fermi level by splitting it away from zero bias, in that, with particularly high sensitivity. Finally, a deconvolution can be done using equa-
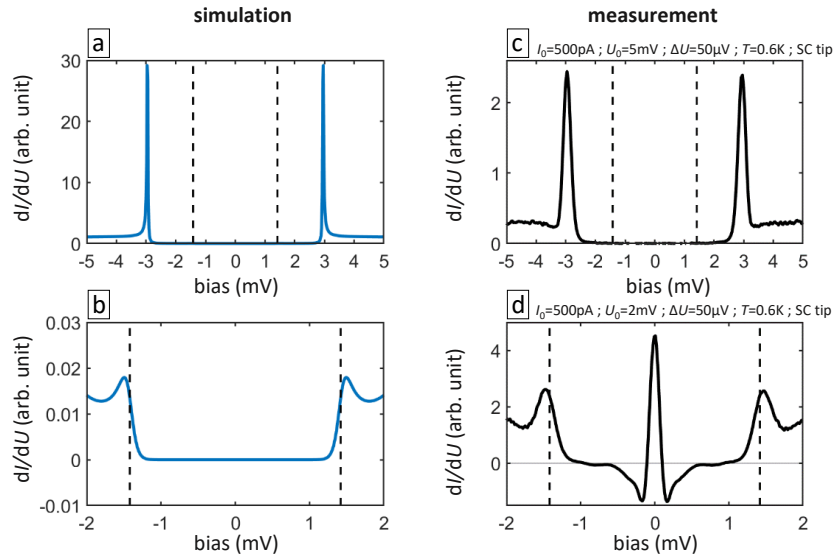
Fig. 3.13: **Josephson current around zero bias:** **a** Simulated superconductor-superconductor junction not considering Cooper pair tunneling. **b** Same data like in **a** zoomed to a small signal within ±2 mV. **c,d** Corresponding measurement shows additional zero bias peak originating from Josephson current.

tion 3.7 and a modeled tip DOS like in figure 3.11a. The result should be proportional to the sample DOS only and take advantage of the improved resolution beyond temperature broadening. Indeed, in contrast to the W tip measurement, two peaks close to zero are resolved and sharper. However, one part of the deconvolution still produces negative values which is unphysical for a signal that should purely depend on density of states of the sample. Despite a quite accurate estimation of the tip superconducting gap can simply be extracted from the position of the coherence peaks, i.e. $\Delta_{\mathrm{t}} = \Delta_{\mathrm{coh}} - \Delta_{\mathrm{Nb}}$, only small mismatches in the modeled shape produce incorrect signals in the deconvolution that could be misleading the interpretation as ρ_{s}. Therefore, in this work processing of raw data shall be reduced as much as possible, i.e. also data taken with superconducting tips is not deconvoluted. Hence it is important to always keep the effects explained in figure 3.11 in mind for presented data in chapter 4, especially since the term *zero energy* is used for signals appearing at a bias of $\pm\Delta_{\mathrm{t}}/e$.

Cooper pair tunneling

So far, only quasiparticle tunneling was considered in $\mathrm{d}I/\mathrm{d}U$ simulations of SIS junctions. The 1962 predicted Josephson effect[104], however, describes the possibility of tunneling Cooper pairs. A resulting supercurrent between superconducting electrodes alternates with a frequency depending on the junction bias U[53]:

$$f_{\mathrm{J}} = U \frac{2e}{h} \, . \tag{3.10}$$

Therefore an effective DC current signal can be measured at $U = 0$. It was calculated to be proportional to the superconducting order parameter of the involved superconductors, i.e. the gap size Δ, and to the inverse junction resistance $1/R_0 = I_0/U_0$ [140]:

$$I_J = \frac{\pi}{2e}\frac{\Delta}{R_0} \qquad (3.11)$$

assuming identical Δ for both electrodes. This expression was demonstrated to be in good agreement with STM results [105].

Figure 3.13 compares the previously shown unperturbed finite temperature SIS junction simulation to measurement dI/dU data. Zooming in to investigate the sub-gap structure, one finds maxima close to $\pm\Delta_t$ corresponding to the Fermi-Dirac broadened tip gap. The data clearly features an additional peak at zero whose physical origin was not considered in the simulation. It is the dI/dU representation of the Cooper pair supercurrent. Its intensity is therefore also a sensitive indicator for the superconducting order parameter. It can be used to measure variations of Δ with high precision.

3.2.2 Magnetic tips

Using magnetic tips in STM to obtain a spin-polarized tunneling current is an intriguing way to investigate magnetic nano-textures. Detailed information about this technique can be found in the literature [141].

For a tunnel junction between two electrodes with non-vanishing spin polarization P_t, P_s and corresponding magnetization vectors $\boldsymbol{m}_t$ and $\boldsymbol{m}_s$, respectively, the tunneling current has been derived in the vanishing-bias limit and under the assumption of free electrons to [142]

$$I = I_0(1 + P_t P_s \boldsymbol{m}_t \boldsymbol{m}_s) \qquad (3.12)$$

with the non-polarized current I_0. This simple equation clearly describes the increase or decrease of the normal tunneling current for parallel or antiparallel alignment, respectively, by the amount $P_t P_s$ following a cosine function from 0° to 180° depending on the angle between $\boldsymbol{m}_t$ and $\boldsymbol{m}_s$.

In this work, magnetic tips were made from pure Cr rods by etching them to sharp tips like shown in figure 3.8. After inserting them to the STM, their spin sensitivity has been tested on the well-studied iron double layer on W(110) [127] like depicted in figure 3.14b-d before using them on samples of interest. Alternatively, picked-up magnetic atoms also yielded tip magnetization. This will further be discussed in section 4.5.
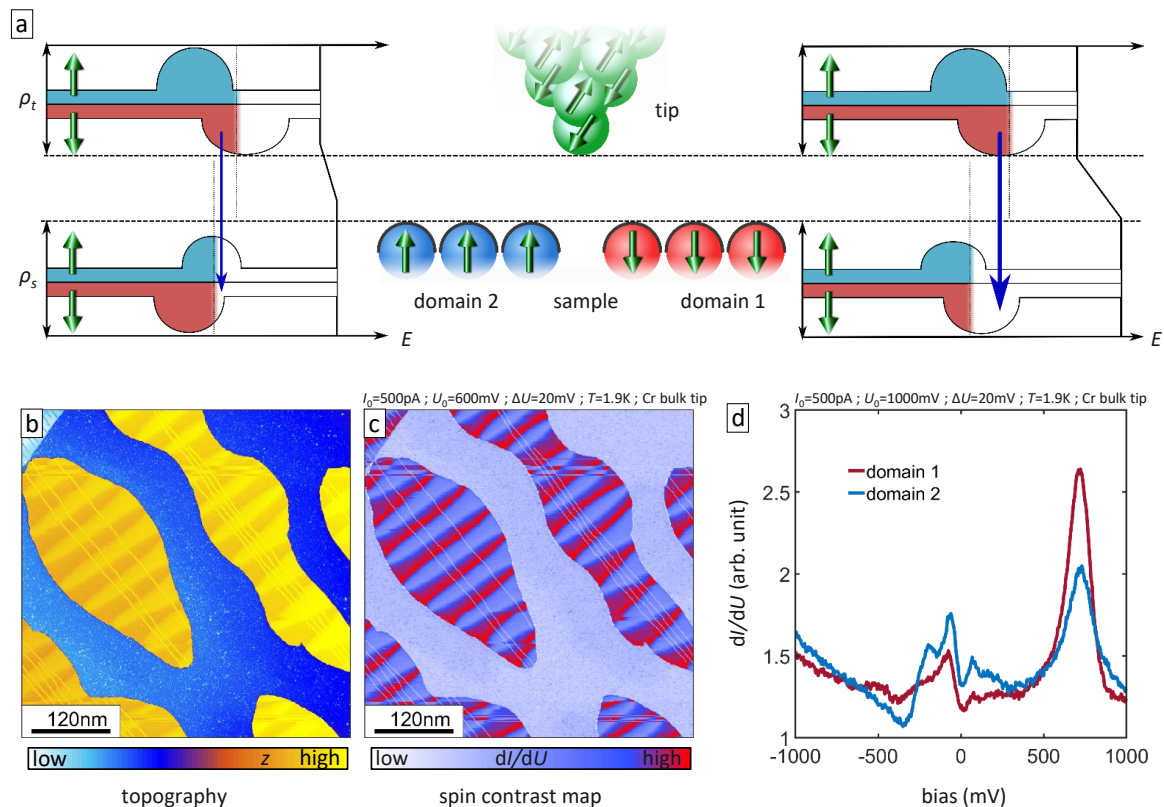
Fig. 3.14: **Spin polarized measurements using magnetic tips: a** Simplified picture
of spin polarized tunneling. The last tip atom is magnetized and two magnetic
domains with opposite magnetization on the sample are drawn. Density of
states is dissimilar for electrons of opposite spin in both tip and sample leading
to higher tunneling current for parallel magnetization. **b,c** Topography and
dI/dU map with a Cr bulk tip on islands of 2 monolayer Fe on W(110) showing
spin sensitivity on red and blue magnetic domains. **d** STS on the two monolayer
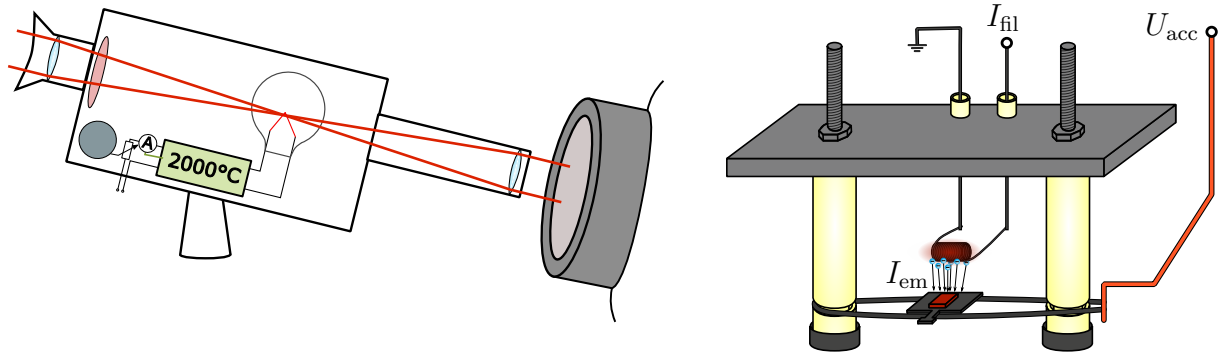Fe on neighboring domains.

Fig. 3.15: **Sample cleaning:** Electron beam heating stage (right) with sample surface facing the filament, filament current I_fil, acceleration voltage U_acc and emission current I_em. Disappearing-filament pyrometer (left) for temperature measurement.

3.3 Sample preparation

In this section the experimental steps necessary to study magnetic impurity adatoms on the Nb(110) surface by low temperature STM will be explained, including the cleaning of Nb(110) substrates after introducing them to UHV, basic characterization in accordance with previous work and deposition as well as manipulation of adatoms on the surface.

3.3.1 The substrate surface

A surface of clean Nb is a crucial requirement for the experiments performed in this work. Despite being a natural substrate choice for the field, with the largest gap among elemental superconductors, experimentalists failed to obtain clean surfaces until as recent as in 2019. The preparation of a clean Nb(110) surface by heating a single crystal close to the melting point (2477 °C) has been demonstrated nicely and described in detail by Odobesko *et al.*[116].

For this work, niobium single crystals with (110) surface normal aligned with an accuracy <0.5°, polished to a roughness of <0.03 μm and cut to the dimensions $7 \times 7 \times 1$mm have been commercially purchased from *Surface Preparation Laboratory*. They were fixed to a tungsten flag style sample plate featuring a 5 mm hole below the crystal to reduce heat dissipation. Four small pieces of tantalum foil between plate and sample prevented the alloy formation at the Nb to W interface, reducing also the imminent strain due to fast heating. Wire of either tungsten or niobium was used to rigidly strap crystals to the holder.

To reach sufficiently high temperatures the sample was mounted on a home-built electron beam heating stage like depicted in figure 3.15 where it rests on top of only two straight pieces of tungsten wire providing the high DC voltage U_acc necessary to accelerate electrons emitted from a tungsten filament to the sample. When electrons hit the

surface they rapidly dissipate their kinetic energy eU_{acc} and thereby heat up the target. Very limited thermal contact to colder parts supports the accumulation of heat in the sample. A commercial halogen lamp filament provided free electrons by heat induced emission at typical supplied filament power between 25 to 35 W. High vacuum is a strict requirement for an efficient electron beam current I_{em} to hit the target where high temperatures are quickly reached at relatively low power. The temperature on the sample surface was measured using a disappearing-filament pyrometer which is an analog technique relying on the human eye to compare the color of the glowing specimen to a calibrated filament in the optical line of the pyrometer (see Figure 3.15). Depending on the sample temperature, the black body radiation spectrum shifts according to Planck's law so that the setpoint temperature is reached when the filament optically vanishes into the background of the glowing sample. However, it turned out that measurements underestimate the real temperature, presumably because of additional wavelength selective absorption at the UHV chamber's viewport which the light has to pass before measurement. The values given correspond to the pyrometer readout and do not represent the real temperatures on the sample.

Initially a careful degassing at moderate annealing temperatures of about 1300 °C over several minutes and keeping the pressure below 10^{-8}mbar is done, followed by a series of short heating flashes up to 1900...2000 °C in 12 s yielded an ordered Nb(110) crystal surface suited for STM study, the obtained STM topography image is shown in Figure 3.16a. However, the observed structure does not correspond to a pure Nb crystal lattice (compare Figure 3.16j). Instead, a superstructure of linear rows consisting of niobium atoms surrounded by oxygen atoms forms a highly stable surface reconstruction of NbO type[144,145]. Oxygen will only dissociate when the surface temperature reaches a value close to the Nb melting point. Subsequent electron bombardment was applied to the sample in many short flashes limited to 12 s with 3 min separation in order to reduce the heating of surrounding parts and resulting bad vacuum pressures. Temperatures above 2000 °C were achieved by high voltages $U_{acc} \approx 2.2$kV and electron beam currents of $I_{em} \approx$ 240 mA. After several tens of flashing cycles, a topography image (Figure 3.16b) reveals a partially clean surface with big patches of oxygen arranged in stripe-like structures still covering about 50 % of the surface. Only after more than a hundred cycles sufficiently clean Nb as shown in Figure 3.16c was obtained, however, some surface contaminants, very likely oxygen and hydrogen, remain and appear as depressions in the topography scan. They presumably adsorb to the surface during transfer of the sample from the preparation chamber to the STM head in the analysis chamber. Hydrogen remains rather mobile even at the cold surface and can be removed from an area by applying a bias voltage pulse of around −2 V, whereas oxygen contaminants limit the maximum clean square area to typically 12 × 12 nm . Larger areas (see Figure 3.16d) feature parallel atomic steps typical for metal surfaces with flat terraces over tens of nanometer width. A line profile over a
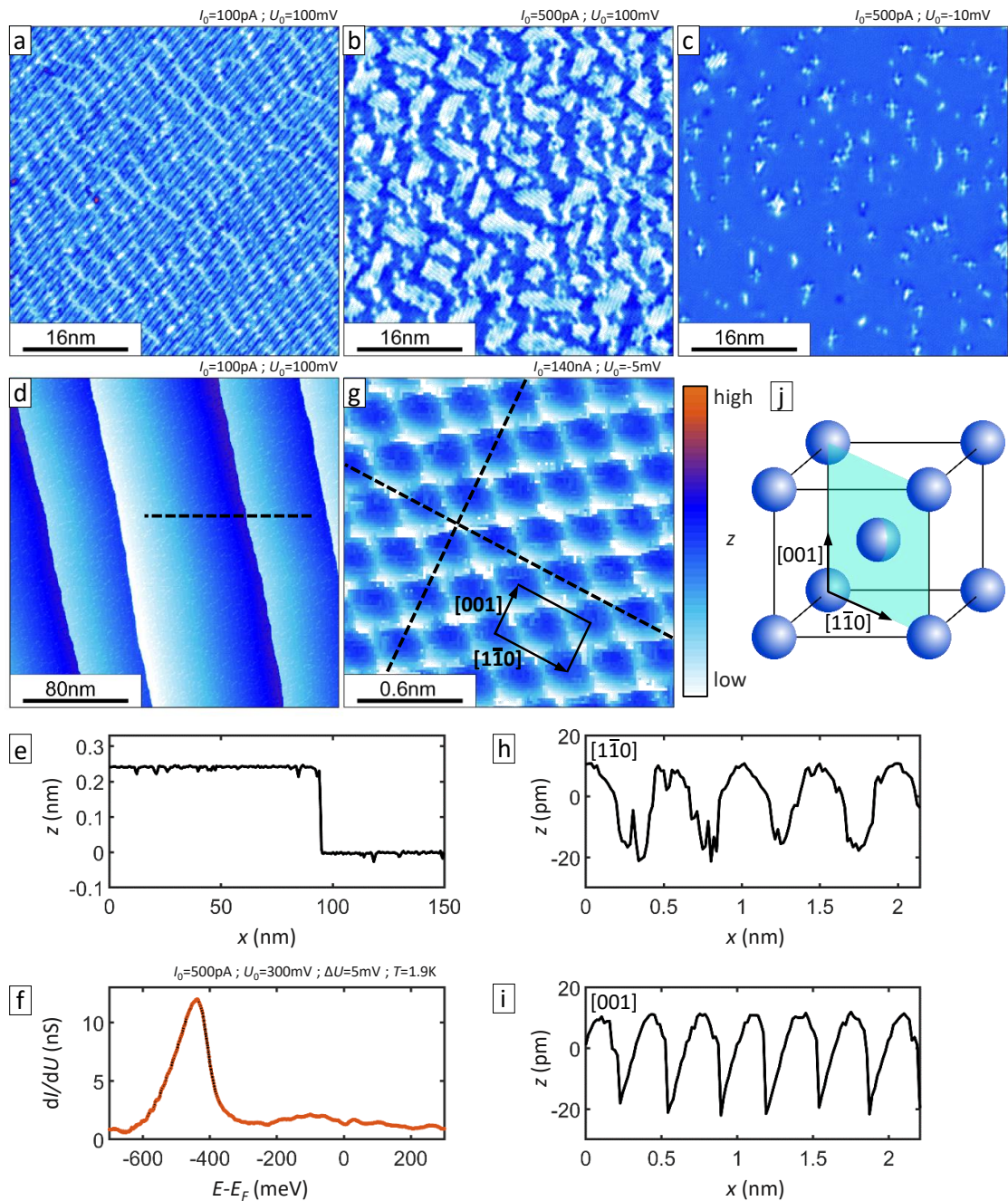
I_0=100pA ; U_0=100mV I_0=500pA ; U_0=100mV I_0=500pA ; U_0=-10mV

I_0=100pA ; U_0=100mV I_0=140nA ; U_0=-5mV

I_0=500pA ; U_0=300mV ; ΔU=5mV ; T=1.9K

Fig. 3.16: **Nb(110) preparation: a-c** STM topographic images of a 50nm × 50nm flat area on the Nb(110) surface, after: **a** flashing with T<2000°C (100mV/100pA), **b** with T>2000°C about 50 times, **c** more than 100 times. **d** Cleaned surface area with several atomic steps. The dashed line indicates the position of the height profile in **e**. **f** STS in a clean area[143]. **g** Atomic resolution image[139] with indicated unit cell and high symmetry directions, line profiles along dashed lines are shown in **h** and **i**. **j** Bulk unit cell of the bcc lattice with indicated (110) plane and crystallographic directions.
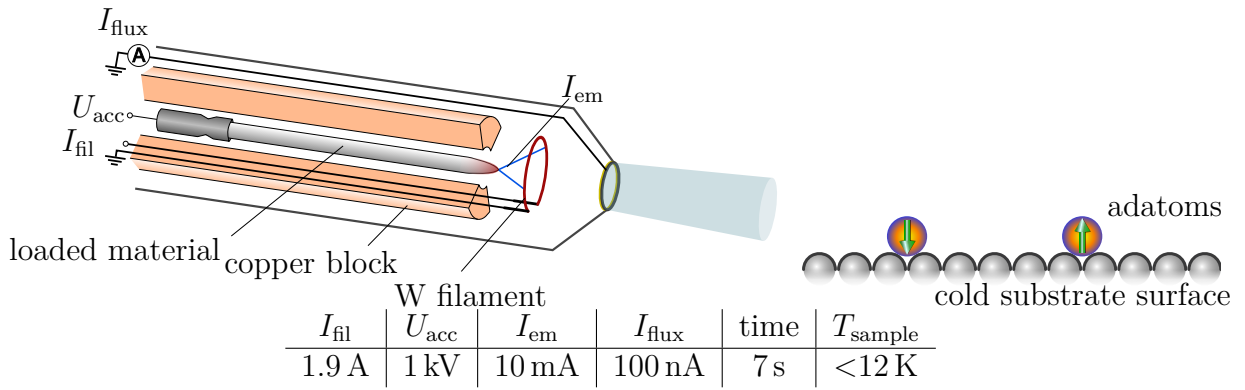
I_{fil}	U_{acc}	I_{em}	I_{flux}	time	T_{sample}
1.9 A	1 kV	10 mA	100 nA	7 s	<12 K

Fig. 3.17: **Adatom deposition.** Schematic illustration of an electron beam evapora-
tor used for depositing single atoms. The loaded material to be evaporated is
drawn as a rod but can also be inside a Mb crucible. A voltage U_{acc} accelerates
electrons emitted from a tungsten filament by heat induced from a current I_{fil}
towards the rod which creates an emission current I_{em} leading to very high
temperatures at the end of the rod. The resulting vapor flux is partially ion-
ized and measured at the exit as I_{flux}. To prevent contamination from heated
surrounding parts, a water cooled copper block encloses the rod. Atoms hitting
the cold surface of the substrate rapidly relax to an energetically favorable po-
sition and lack the thermal energy to migrate. Typical values for the deposition
are listed in the table.

step can be seen in Figure 3.16e, where the step height of 2.4±0.1Å matches the bulk value
$a_{\text{Nb}}/\sqrt{2}$ = 2.3Å with a_{Nb} = 3.3Å. Additionally, STS over clean areas (see Figure 3.16f)
feature a characteristic peak in the density of states at −435 meV corresponding to the
d_{z^2} state of Nb(110)[116]. Further evidence for a clean surface is provided by the observed
atomic lattice shown in Figure 3.16g with two high symmetry directions featuring lattice
constants 4.9 ± 0.2 Å (see line profile in Figure 3.16h) and 3.3 ± 0.2 Å (Figure 3.16i) in
agreement with the crystallographic directions [1$\bar{1}$0] with $\sqrt{2}a_{\text{Nb}}$ = 4.7 Å and [001] with
a_{Nb} = 3.3 Å of the Nb(110) plane highlighted in Figure 3.16j.

3.3.2 Deposition of single adatoms

The next step after acquiring a clean surface is the deposition of a sub-monolayer of
isolated adatoms. Figure 3.17 shows a sketch of the electron beam evaporator technique,
employing the similar heating principle used in the e-beam heater. Five different elements
have been loaded for evaporation, i.e. vanadium, chromium, iron and cobalt as a rod and
manganese inside a molybdenum crucible. By controlling the emission current I_{em}, a vapor
stream is stabilized creating a flux current I_{flux} = 100 nA, a value used for all elements.
Typically this yields a concentration of approximately 6 to 12 adatoms per 100 nm^2. In
order to prevent a migration of adsorbed atoms resulting in the formation of clusters, the
surface temperature must not overcome 20 K during the process. Therefore the Nb(110)
sample is inserted into the microscope head and cooled down to 1.9 K before the deposition
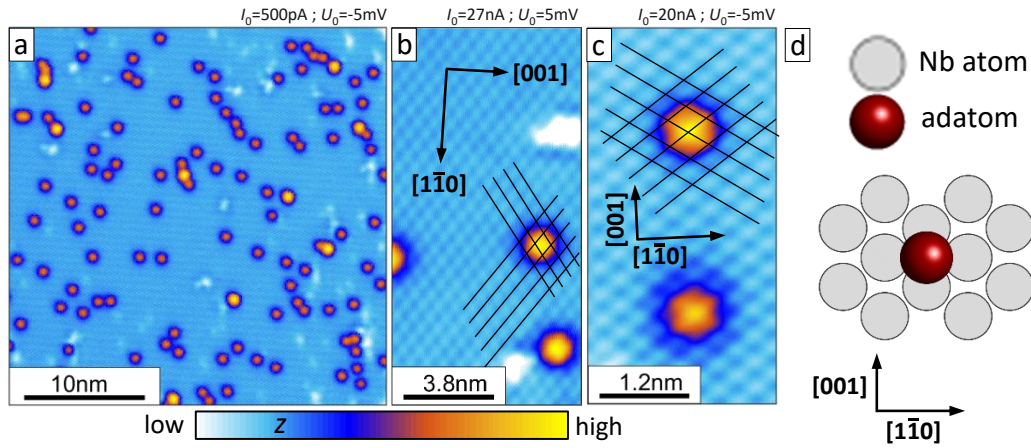
I_0=500pA ; U_0=-5mV I_0=27nA ; U_0=5mV I_0=20nA ; U_0=-5mV

Fig. 3.18: **Adsorbtion of single atoms: a** STM topography image showing Cr adatoms on the clean Nb(110) surface. **b** Atomic resolution image showing the adsorption site as the hollow site , **c** as the top site. Images **b** and **c** have been processed by Fourier filtering and enhancing the Nb lattice corrugation[143]. **d** Illustration of the hollow site configuration assumed throughout the thesis.

is done *in situ* by traveling out from the cryostat and shortly opening the radiation shield for about 7 s. Temperature reading close to the tunnel junction indicates that during this process the sample does not warum up to more than 12 K.

An example topography image is given in Figure 3.18a with a concentration of 11 atoms/100nm², all of which are chromium atoms. One observes the same appearance for all isolated adatoms of a single element. Enhanced apparent height occurs for atoms in immediate proximity to oxygen, or for clusters of two or more atoms in nearest neighbor position due to a different electronic configuration. Moreover, STS taken on the adatoms is consistent throughout all isolated single impurities of equal species. These facts strongly indicate that all adatoms relax into a single adsorption site after deposition that is energetically most favorable. Theory predicts this is to be the hollow site in the center of 4 Nb surface atoms illustrated in Figure 3.18d in agreement with reported data in the literature[28]. However, STM scans over adatoms while simultaneously resolving the atomic lattice of Nb seen in Figure 3.18b,c can be misleading, showing adatoms in either top or hollow site. This is due to the so-called corrugation reversal effect, i.e. atom sites appear as depressions in STM imaging. It was theoretically predicted for (110) surfaces of bcc lattices in metals due to their electronic orbital structure close to the Fermi level[146] and can occur depending on the tip apex configuration and the setpoint used for tunneling, especially for low biases that are needed to get sufficient sensitivity to observe the atomic lattice.
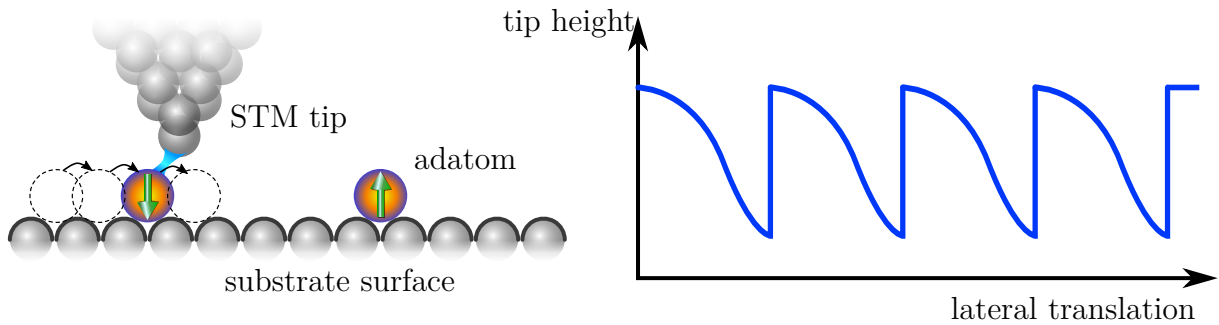
Fig. 3.19: **Adatom manipulation:** Illustration of the atom manipulation process. The STM tip is brought close to an adatom by using a low bias and high current setpoint (typical −5 mV and >40 nA). Attractive forces enable the tip to drag the adatom laterally in the form of consecutive jumps from one stable site to the next. The right diagram shows the typical tip height feedback behavior during this process. First the tip height lowers continuously while moving away from the protrusion center of the adatom followed by a sudden tip retraction when the adatom moves to the available lattice site closest to the tip.

3.3.3 Moving adsorbates over the surface

An intriguing way to craft nanostructures at the atomic scale is the use of an STM tip to manipulate atoms on top of a surface as was first demonstrated by Eigler *et al.*[112]. Nb features a high cohesive energy preventing adatoms from relaxing far into the surface and therefore making their manipulation feasible. To illustrate the process as observed in the experiment, Figure 3.19 sketches a typical tip height profile when a single adatom is dragged over the surface. It becomes clear that only specific stable lattice sites are occupied by the adatom, indicated by jump-like behavior during the manipulation. On the one hand, this poses a limitation in the positioning of atoms to specific sites, on the other hand brings the big advantage of exact knowledge over relative atom distances, fail-proof even under slight miscalibration of the piezo scanner or lateral drift between tip and sample.

3.4 Theoretical methods

Theoretical results shown in sections 4.1 as well as 4.2 are first-principles calculations based on density functional theory (DFT) in the framework of the scalar-relativistic full-electron Korringa-Kohn-Rostoker (KKR) Green function augmented self-consistently with spin-orbit interaction[147,148]. Details are described in corresponding publications[143,149]. Section 4.1.4 and 4.3 about anomalous spin excitations have been treated by time-dependent DFT including spin-orbit interaction. Many-body effects triggered by the presence of spin excitations are approached via the many-body perturbation theory ex-

tended to account for relativistic effects. It was used to successfully describe spectral shapes for magnetic adatoms on noble metals[134]. Details are found in the publication by Brinker *et al.*[150]. In section 4.4, a tight-binding model is used to calculate the LDOS on magnetic impurity chains by neglecting spin-orbit interaction, details can be found online[139].

4 Results

In this chapter, experimental findings of the actual STM study will be presented and discussed following an order where subsequent results build on top of each other for a better understanding of follow-up experiments wherever possible. A coherent picture of magnetic impurity adsorbates on Nb(110) shall be established, systematically starting from zero dimensions, progressively expanding to one and ending with two dimensional structures.

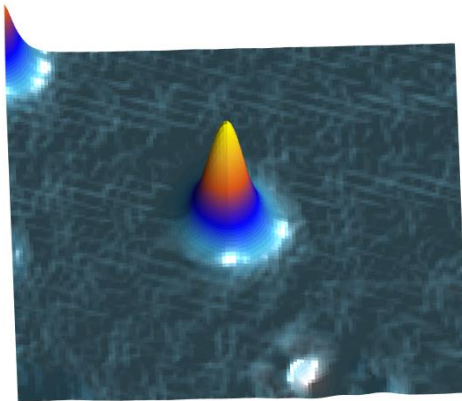## 4.1 Single magnetic adatoms on Nb(110)

Figure: STM image of an isolated chromium adatom on Nb(110).

This section contains a detailed investigation of five different $3d$ transition metal elements on Nb(110) illustrated in figure 4.1, namely vanadium V, chromium Cr, manganese Mn, iron Fe and cobalt Co. Each element progressively adds one electron to the orbital structure, all of them feature a partially filled atomic $3d$ shell, thus they bear the potential to retain magnetic moment when interfaced to a metal surface. They are found diluted with sub-monolayer coverage which allows to study single isolated adatoms.

After a basic topographic comparison of apparent height, mainly three distinct ways to scrutinize the coupling between magnetic impurities and the superconducting condensate are employed, all of them rely experimentally on STS. First, the spectral fingerprints and orbital dependent spatial distributions of YSR in-gap states were measured. Second, the reduction of the Josephson current and hence the superconducting order parameter was quantified and third, for observed metallic responses in a non-superconducting regime different possible interpretations are considered, i.e. either attributing measured dI/dU signals to inelastic spin excitation tunneling events or assuming a Kondo resonance and assigning a Kondo temperature by fitting the curves with Frota functions. At the end, a preliminary evaluation of inter-impurity coupling behavior is shown and the element choice for continued exploration is justified. The majority of Data shown here was published in *Nature Communications*[143].

	V	Cr	Mn	Fe	Co
	$3d^3 4s^2$	$3d^5 4s^1$	$3d^5 4s^2$	$3d^6 4s^2$	$3d^7 4s^2$

Fig. 4.1: Elements used for single atom deposition. The table shows respective electron configurations after [Ar]. The colorcode for the elements will be used consistently throughout this section.
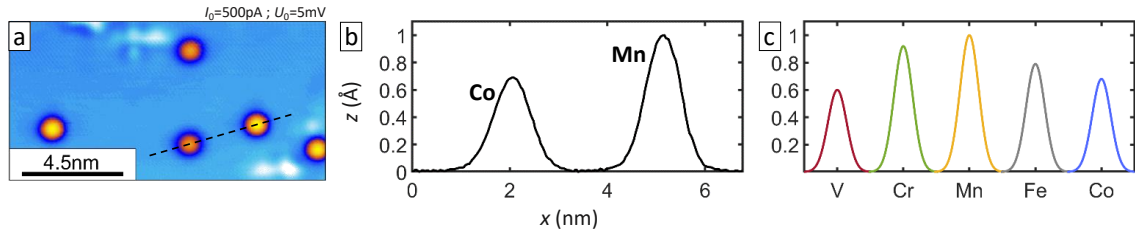
Fig. 4.2: Adatom height profiles: a Topography scan showing Co and Mn adatoms on Nb(110). **b** Height profile corresponding to dashed line in **a**. **c** Height profiles for all five elements. Measured raw values have been adjusted by keeping ratios of elements measured in one run to account for different microtips.

4.1.1 Adatom apparent height

By simultaneous deposition of more than one atomic species, a direct comparison of their properties becomes possible while excluding the influence of different tip conditions. Since a deposition of all five elements on one surface was not practicable because of inevitable disorder and simply because only two evaporators are attached to the STM chamber, usually two different species were deposited on the same surface. Cross-referencing the results and checks of reproducibility made sure that comparability is maintained and that the observed trends are real. The first observation from topography scans is a varying apparent height for all five elements shown in figure 4.2. Note that here the corrugation does not only depend on the setpoint used for stabilization in constant current mode but also the tip shape can have significant influence on the measured height. Therefore each element has been referenced to Mn, which was measured several times with different tips yielding an average height value of $1\,\text{Å}$, the highest corrugation, followed by Cr, Fe, Co and V. Different heights are a consequence of individual electronic configuration as well as surface relaxation to minimize the energy of the adatom-substrate system through formation of hybridized states. It will become evident in the following that this can already be an indication for the adatom's coupling strength to the superconductor, however, there is not an unambiguous correlation to the magnetic properties of the adatom-substrate system.

4.1.2 YSR spectroscopy

The energy ε_{YSR} of induced in-gap resonance pairs is governed by the spin magnetic moment and coupling strength, SJ, to the superconducting condensate (see section 2.1.2).
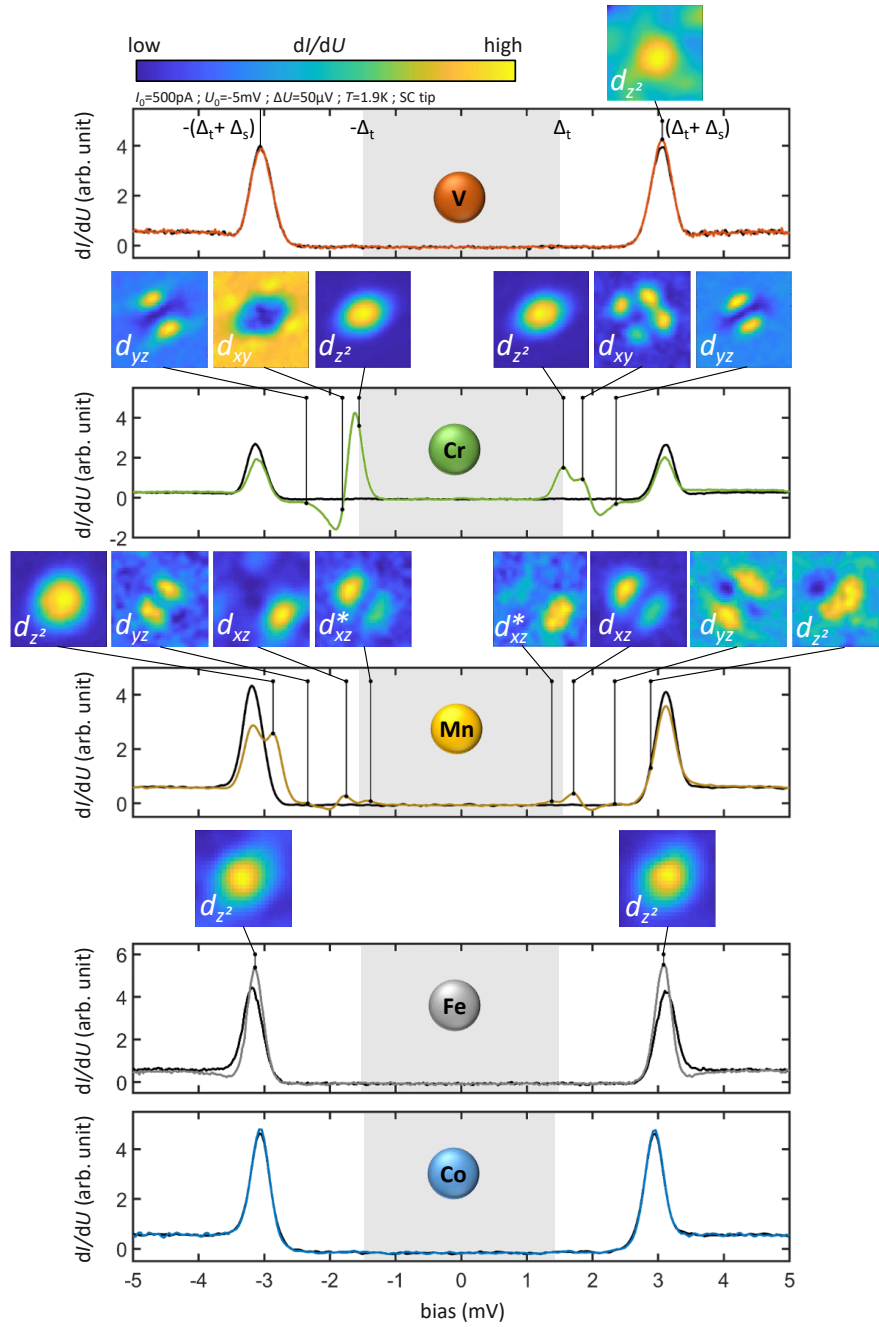
Fig. 4.3: **YSR spectroscopy:** STS measured on top of five different adatoms. Gray areas mark the tip superconducting gap. Above, corresponding dI/dU maps are depicted at specific energy positions indicated by thin black lines. Spatial distributions in dI/dU maps resemble atomic d orbitals.

Since multiple d orbitals of each adatom contribute to the overall spin, consistent with theoretical predictions shown in figure 4.6 finding high spin states for all elements except Co, it is possible to observe several YSR pairs as long as each spin S has an appropriate J to result in an energy inside the superconducting gap. With the spatial resolution of the STM the shapes of YSR states can be visualized that strongly resemble atomic d orbitals[17]. Regarding intensities, particle-hole asymmetry in energetically symmetric pairs is expected[15]. Additionally, the STM technique favors orbital geometries that extend further into vacuum away from the surface, in this case especially the d_{z^2} orbitals that are therefore showing a higher $\mathrm{d}I/\mathrm{d}U$ signal intensity. Note also that these measurements have been conducted at temperatures as low as $1.9\,\mathrm{K}$, yet thermal replica peaks within the elsewise forbidden tip gap zone $[-\Delta_\mathrm{t}, +\Delta_\mathrm{t}]$ are detected[16].

Considering those effects it is possible to understand the results summarized in figure 4.3, where $\mathrm{d}I/\mathrm{d}U$ spectra over the center of each of the five different adatoms are plotted, together with $\mathrm{d}I/\mathrm{d}U$ maps showing the intensity distribution of respective YSR peaks in real space. All spectra are very reproducible and could be detected over tens of atoms of the same kind without large deviations. Starting from both ends of the investigated selection of elements, i.e. V and Co, the sub-gap signal is featureless. Co shows no difference to the substrate at all within the limit of our experimental resolution and sensitivity, while the data for V suggests a weak enhancement at the edge of the superconducting gap in the unoccupied states with a circular shape indicative of a d_{z^2} orbital. In contrast to that, clear traces of magnetism induced YSR pairs can be detected on Cr, Mn and Fe. The latter has only one set of peaks far away from the Fermi level and nearly overlapping with the coherence peaks of the superconductor, signaling either very weak or strong J. The shape is again d_{z^2}-like with approximately isotropic shape. Next in line is Cr featuring 3 non-degenerate pairs detected within experimental limits, corresponding to d_{z^2}, d_{xy} and d_{yz} orbital shapes. A comparison of their intensities verifies the expectation that d_{z^2} orbitals dominate the signal. Particularly its low energy, almost exactly at $\pm\Delta_\mathrm{t}$, i.e. corresponding to the Fermi level or zero energy, identifies a coupling very close to the critical value J_crit of a quantum phase transition and will become important later on. Finally, Mn also induces YSR states from three orbitals, i.e. d_{z^2}, d_{xz} and d_{yz}, however, in the data an additional set of peaks d_{xz}^* appear because of thermally populated states at energies $E_\mathrm{rep} = \pm(\Delta_\mathrm{t} - \varepsilon_{xz})$ that replicate the d_{xz} states at $E = \mp(\Delta_\mathrm{t} + \varepsilon_{xz})$ as described in section 3.2.1. Once more the d_{z^2} peaks appear with the highest intensity, yet in contrast to Cr, far away from the Fermi level. The less intense d_{xz} signal is again deeper in the gap, yet still clearly distinct from zero. A thorough investigation of Mn adatoms on Nb(110) can be found in the publication by Beck *et al.*[29].

Concluding from YSR spectroscopy data, there are significant differences in the magnetic impurity-to-superconductor coupling between the elements and, in case of Cr and Mn, between different angular wave functions carrying spin moment where degeneracy is
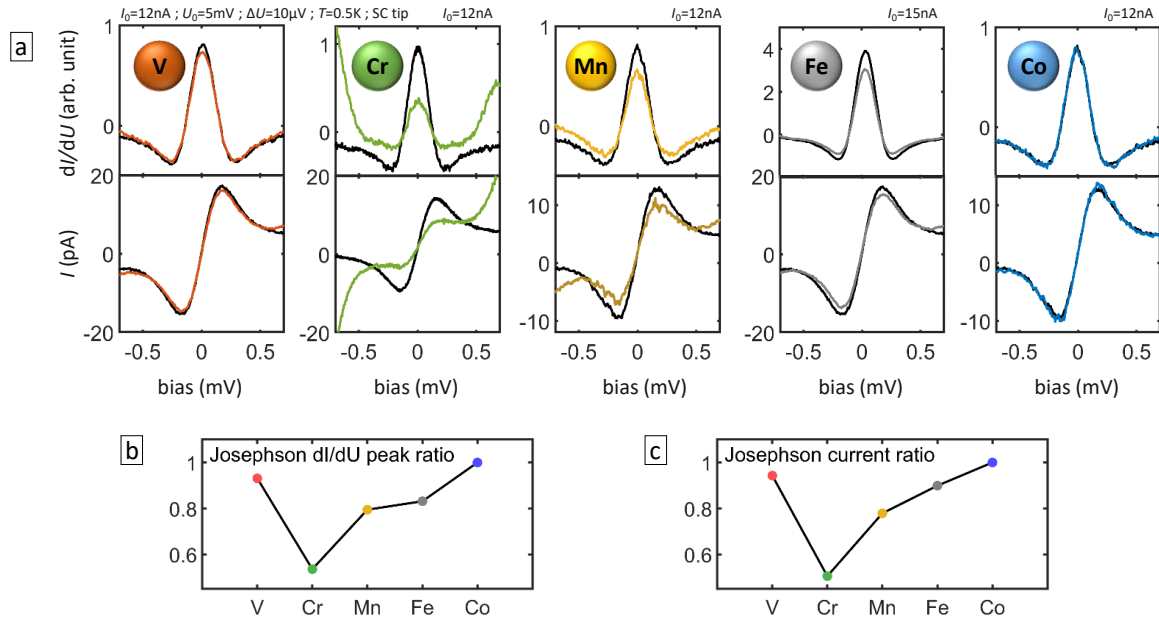
Fig. 4.4: **Josephson spectroscopy: a** dI/dU signals (upper) and tunneling current (lower) on the adatom (color) and on substrate (black). **b** Reduction of Josephson dI/dU peak and **c** of Josephson current.

lifted by the substrate. Deep YSR states have been found on Mn and Cr, particularly intense is the Cr d_{z^2} resonance having particle and hole part overlapping at the Fermi level. If and how these observations are related to direct magnetic influence on Cooper pair tunneling shall be elucidated in the next section.

4.1.3 Josephson spectroscopy

In this part, the Josephson supercurrent at zero bias between tip and sample has been measured and quantified on magnetic impurities relative to the bare superconductor. As explained in section 3.2.1, the reduction of Josephson currents caused by magnetic impurities is a direct consequence of a weakened Cooper pair coupling and thus a reduced order parameter Δ. Hence, by quantification it is possible to compare all five elements in their direct suppression of superconductivity. Note that this effect is not measurable on coherence peaks which do not change their position within the energy resolution.

Current and dI/dU signals in a small window ± 0.7 mV around zero are depicted in figure 4.4. Measurements were taken by stabilizing the tip in a central position over an adatom with high current setpoint of ~ 12 nA and outside the superconducting gap at 5 mV to avoid setpoint effects. Calculating the ratio between impurity and substrate peak heights $([\mathrm{d}I/\mathrm{d}U]_{\max}^{\mathrm{atom}} - [\mathrm{d}I/\mathrm{d}U]_{\min}^{\mathrm{sub}})/([\mathrm{d}I/\mathrm{d}U]_{\max}^{\mathrm{sub}} - [\mathrm{d}I/\mathrm{d}U]_{\min}^{\mathrm{sub}})$ and maximum current values $(I_{\max}^{\mathrm{atom}} - I_{\min}^{\mathrm{atom}})/(I_{\max}^{\mathrm{sub}} - I_{\min}^{\mathrm{sub}})$ results in panels b and c of figure 4.4, respectively. The two plots show a very similar trend which is in general consistent with the observations in YSR spectroscopy. Starting from V with a weak dI/dU peak (current) reduction of 93 % (94 %) , maximum reduction is observed for Cr with 54 % (50 %), before lowering to 79 %

(78 %) for Mn followed by Fe with 83 % (90 %) and arriving at Co with no reduction at all. Moreover, spatially resolved maps yield an isotropic distribution of reduced current around adatoms. Further, a tip height related origin correlated to the distance between both superconducting electrodes can be ruled out for two reasons: First, despite a connection between magnetic properties and apparent height can be assumed when comparing results to figure 4.2, current reduction is not directly correlated to corrugation. Second, an identical Josephson signal is observed both on the bare substrate and on top of Co adatoms, thereby confirming a non-magnetic configuration. In conclusion, the elements V and Co that feature no YSR states consistently exhibit the lowest impact on Cooper pair tunneling. Remarkably, Cr induces by far the strongest reduction of the superconducting order parameter. The monotonic trend from Cr over Mn to Fe seems in good qualitative agreement with the energetic position of their d_{z^2} states from very deep inside the gap to more towards the gap edge. Regarding the overall trend, it suggests an oscillatory behavior with increase in orbital occupation.

4.1.4 Metallic regime

After scrutinizing the effect of magnetic impurities on superconductivity, it is meaningful to investigate the pure metallic response as well and to compare it to previous works where dI/dU measurements explored Kondo resonances[15,151,152] and spin excitations[133,134,153,154] traced through inelastic tunneling events. On a superconductor the gapped density of states around the Fermi level strongly hinders detection of the above mentioned signals, therefore it becomes necessary to suppress superconductivity to facilitate their investigation. This can be done by raising the temperature above T_c or by application of an external field $H_{ext} > H_{c2}$. In the present case the former is not feasible due to losses in energy resolution and a lack of temperature stability at elevated temperatures in the used system, thus an external field of 1 T was applied out of plane so that the critical field of Nb (~ 0.5 T) is well exceeded.

The results are summarized in figure 4.5. Panel a shows experimental data for each element normalized to the substrate background. Once more, V and Co do not differ from the background significantly. Cr, Mn and Fe turn out to raise the dI/dU signal around the Fermi level with a very asymmetric shape resembling a step. Particularly Cr features a sharp step-like increase, Mn a broader step with considerably lower intensity and Fe a very broad monotonic increase. A comparison of Cr, Mn and Fe is shown in panel c with a larger energy range in their respective colors, revealing a strong broad signal on Fe.

First-principles calculations of spectra shown in panel b follow a theoretical approach that was recently used successfully to explain signals obtained on Co adatoms on noble metal surfaces[134] by unconventional spin excitations induced by finite magnetic anisotropy energy, challenging previous interpretation as Kondo resonances[151]. It re-
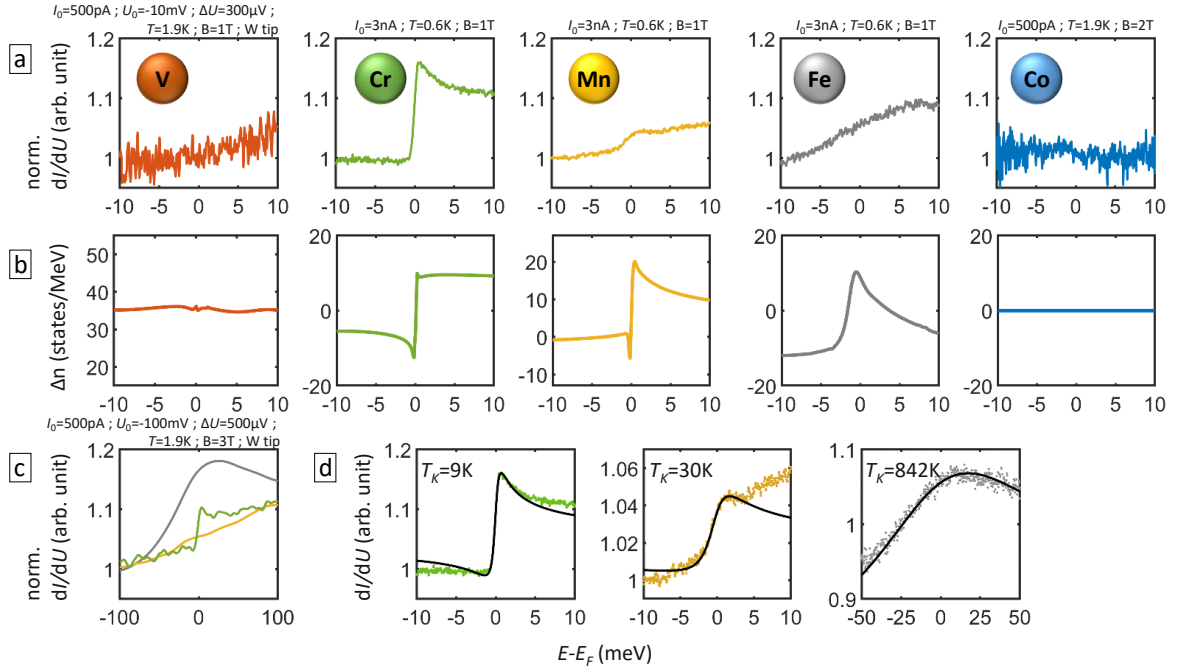
Fig. 4.5: **STS in the metallic regime: a** Experimental dI/dU spectra normalized to the substrate signal. **b** Theoretical inelastic tunneling spectra calculated from *ab initio*. **c** Experimental data for Cr, Mn and Fe in a larger bias range. **d** Frota fits (black) to experimental data with corresponding Kondo temperature.

produces vanishing signals on V and Co as well as, with good agreement, the sharp step on Cr. Spectra for Mn and Fe turn out being an order of magnitude broader in the experimental data. However, theoretical spectra rely on very exact knowledge of the magnetic anisotropy energy and any slight underestimation of the calculated value can result in considerable changes of width in the dI/dU curve predictions. A generally good agreement justifies the consideration of this quite recent theory, especially since it is intrinsically independent of experimental input or fitting parameters.

A more conventional approach would be the interpretation as a Kondo resonance when Kondo screening competes with the formation of Cooper pairs[15]. The extracted Kondo temperature T_{K} then gives the energy scale for the screening of magnetic impurities. A Frota function for fitting can be written like

$$F_{\mathrm{Frota}} = F_0 + A \times \mathrm{Re}\left(e^{i\phi}\sqrt{\frac{i\Gamma}{eU - E_0 + i\Gamma}}\right) \tag{4.1}$$

with the background offset F_0, the amplitude A, phase ϕ, width Γ, energy offset E_0 and bias U. The Kondo temperature can then be extracted with a proportionality constant from the Frota width Γ

$$T_{\mathrm{K}} = \frac{\Gamma}{1.455 k_{\mathrm{B}}} \tag{4.2}$$

with the Boltzmann constant k_{B}[152]. Best fits for Cr, Mn and Fe are shown in figure 4.5d with corresponding Kondo temperatures $9\,\mathrm{K}$, $30\,\mathrm{K}$ and $842\,\mathrm{K}$, respectively, meaning an

increase in Kondo screening energy scale from Cr to Fe which is in qualitative agreement with both YSR and Josephson spectroscopy. A consistent interpretation would then be that an increase in adatom-substrate coupling J from Cr to Fe leads to a more effective screening of magnetic moments, limits the Josephson current reduction and shifts the YSR energy towards the lower edge of the superconducting gap. However, while the discrepancy in signal intensity between Cr, Mn and Fe could be explained by the difference in their density of states at the Fermi level (theory calculation in figure 4.6), the exceedingly large Kondo temperature obtained for Fe would be expected to result in vanishing YSR states due to perfect screening rather than the magnetic fingerprints detected. One could argue that multiple Kondo screening channels exist, in analogy to multi-orbital YSR scattering. Then the broad Fe background signal might cover sharper resonances. Interestingly, Fe dimers (compare figure 4.7a,e) feature lower YSR states and show a sharper peak in the metallic regime[1].

At the present stage, it is not clear whether one or the other approach describes best what is observed in the experiment. Together with the group of Samir Lounis at *Forschungszentrum Jülich* who performed all of the first-principles theory calculations, the spin excitation approach was pursued and further explored in section 4.3. In the following, a summary of their theory results concerning the magnetic state properties of surface adatoms shall be shown that, together with the above experimental data, allow to draw a comprehensive picture about the scrutinized five elements posing single magnetic impurities on Nb(110).

4.1.5 Theory results and single impurity summary

Despite the experimental focus of this work, some theoretical results shall support, supplement and help the interpretation of observations made in the measurements. Values shown in figure 4.6b-e are published[143] and were graphically summarized. Panel a is a spin resolved fully ab initio calculated energy dependent density of states for the previously discussed five elements as single adatoms on a Nb(110) surface. All elements except Co differ in their majority and minority spin channel. It means that theory predicts Co to be non-magnetic and the other elements to be magnetic which agrees well with experimental findings. The insert is a zoom around the Fermi Level and panel b depicts the extracted number of states at zero, ρ_0 which can influence the signal intensity of features measured in a small range around this energy. For example, a high DOS at the Fermi level would be a possible explanation for vanishing or weak signals in the metallic regime on V and Mn, respectively, and as well for the strong signal detected for Cr with a low DOS at the Fermi level. Further it can impact the YSR energy or critical coupling $J_{\text{crit}} = (SJ\pi\rho_0)^{-1}$ which would also be consistently in favor of a deep YSR state on Cr even

---

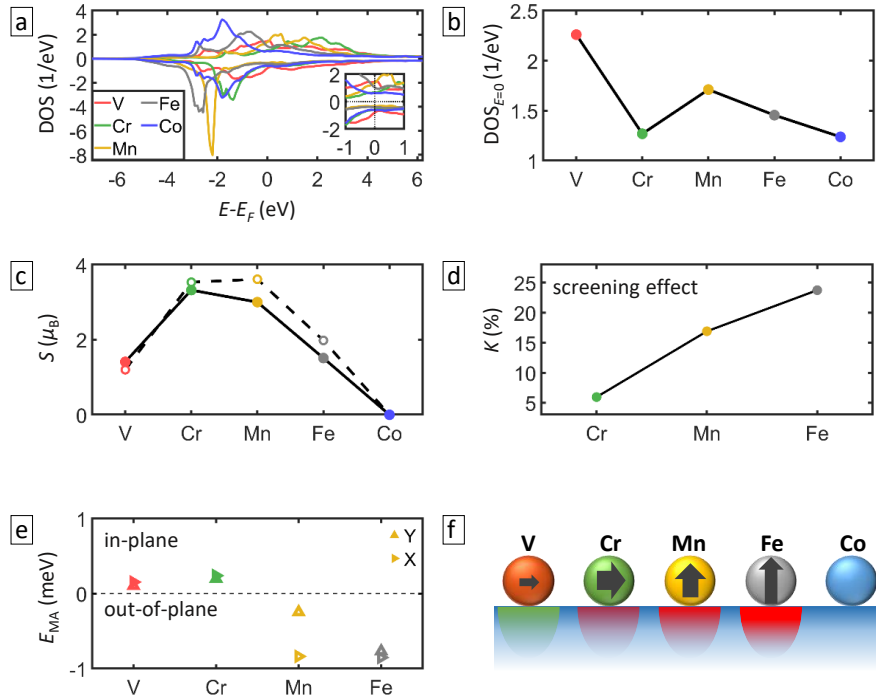[1]No data is shown since the focus in this work is not on Fe adatoms.

Fig. 4.6: **Theoretical results from ab initio calculations: a** Spin-resolved local density of states for five atomic species on Nb(110) with minority and majority spin channel drawn above and below zero, respectively. Inset: Zoom around the Fermi Level. **b** Density of states at the Fermi level. **c** Spin magnetic moments calculated with (solid) and without (dashed) considering adjacent Nb surface atoms. **d** Resulting screening effect of the Nb cluster for antiferromagnetically coupled elements. **e** Magnetic anisotropy energy indicating in plane or out of plane orientation for positive and negative values, respectively along x and y direction. **f** Summary of calculated magnetic properties. Arrow thickness, direction and length: magnetic moment value, orientation in or out of plane and magnetic anisotropy. Half ellipses: Nb surface response: FM (green) or AFM (red) with different transparency indicating magnetic coupling strength.

assuming similar values of J for d_{z^2} states of Cr and Mn. Panels c and d theoretically scrutinize magnetic moments both without the coupling to the underlying Nb cluster (dashed line) and with consideration of the full interacting system (solid line). It can be seen that the magnetic moment for V increases due to ferromagnetic coupling to the substrate while it becomes reduced for the other elements because their initial magnetic moment is partially screened by the antiferromagnetically coupled Nb cluster. On the one hand this can explain vanishing YSR states on V since they are predicted to only appear in the antiferromagnetically coupled case[60], on the other hand the reason for the small reduction of Josephson current measured on V remains unclear. Nevertheless, the trend observed in the reduction of the superconducting order parameter decreasing from Cr to Fe does agree nicely with a decrease of magnetic moment after consideration of the whole cluster. The screening effect, extracted from the ratio between filled and empty circles in panel c, is plotted in panel d and shows a trend similar to the experimental increase

in Kondo temperature fits from Cr to Fe, however, as already stated it does not fit the large value of T_K that results from the Fe signal. Another important theory result is the magnetic anisotropy energy E_{MAE}. It provides information about the preferred direction of magnetic moments in the ground state and how strong this preference is. The graphic in panel e is interpreted as follows: positive values mean in plane orientation, negative values out of plane, the orientation of the triangular marker stands for x or y direction in plane. Therefore V as well as Cr should be weakly in plane oriented, Mn and Fe strongly out of plane while the Mn moment is easier to cant in y direction that corresponds to the crystallographic [001] direction. Finally, panel f shows an illustration to qualitatively and graphically summarize the results. Arrows point in the magnetization direction, i.e. either in plane or out of plane, their length means the strength of magnetic anisotropy and their thickness corresponds to the magnetic moment. The more screened the moments are, the more intense is the red semicircle inside the Nb crystal, whereas green means FM coupling to the substrate. These calculations are in many aspects consistent and in good agreement with trends in the experiment such as the oscillatory behavior of impurity spin moment with orbital occupation from weak to strong and subsequently back to weak, observed in Josephson spectroscopy and correlated to the measured YSR state energies. They play an important role in understanding the measured signals and yield additional information like the magnetic anisotropy.

Overall, Cr exhibits the YSR pair closest to the Fermi level, poses the strongest perturbation to superconductivity and shows the sharpest feature on metallic Nb(110) which enables a sensitive investigation of its behavior. It indicates a balance of Kondo screening and Cooper pair breaking interactions and bears the potential to develop energetically low-lying Shiba bands in coupled structures. The next milestone, namely providing flexibility in nanostructure creation through long-range interaction, shall be demonstrated in the following.

4.1.6 Adjacent and non-adjacent dimers

Following the study of single adatoms, one naturally asks if, and in which way, the magnetic impurities can interact between each other. Since the more interesting case is an interaction of indirectly coupled impurities that are not nearest neighbors in order to gain higher tunability, here, only two contrasting examples are given, i.e. Fe and Cr.

After adatom deposition, round protrusions appearing higher than hitherto presented single atoms, such as shown in figure 4.2, were usually also found on the surface (see figure 4.7a,b) that featured additional different YSR spectra. As an explanation, unequal adsorption sites would be thinkable, however, the observations could be reproduced in most cases by controllably merging two single adatoms by atomic manipulation which identifies those structures as nearest neighbor dimers or clusters of adatoms that are not
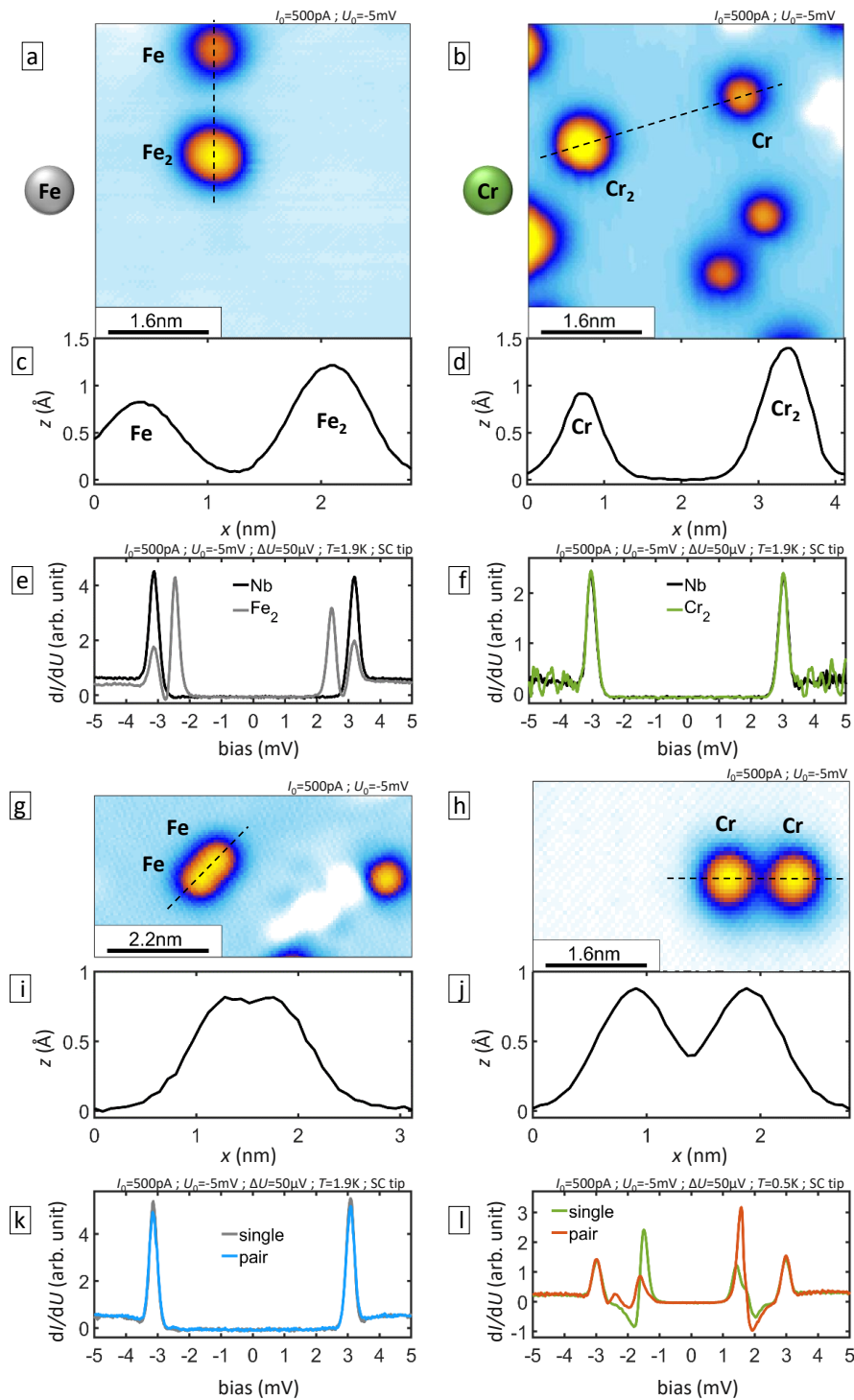
Fig. 4.7: **Investigating dimers:** Fe left, Cr right. **a,b** topography of single atoms and a close distance dimer. **c,d** line profiles corresponding to dashed lines in a/b. **e,f** STS on dimers compared to bare Nb. Fe YSR states shift towards zero while Cr YSR states completely vanish. **g,h** Topography of spaced adatom pairs. **i,j** Corresponding line profiles for dashed lines in g/h. **k,l** STS on adatom pairs compared to single adatoms[149]. Fe shows negligible differences while Cr spectrum changes remarkably.

atomically resolved in the topography scan.

Figure 4.7 compares them to the case of close-distance adatoms that are not positioned on adjacent lattice sites (panels g-l). The line profiles for adjacent and non-adjacent pairs are given in panels c,d and i,j, respectively, showing a significant enhancement of apparent height at the closest distance for both Fe and Cr while only marginal changes are observed for pairs with a small spacing. Very interesting are the quite opposite effects of dimer formation on sub-gap states. In the case of Fe dimers (panel e), at closest distance the YSR pair clearly shifts towards the Fermi level. From equation 2.17 a shift of $\varepsilon_{\mathrm{YSR}}$ is expected since the second impurity changes the total spin moment S_{imp}. Looking at the merged Cr adatoms (panel f), however, all in-gap states disappear, at that together with Josephson current reduction and metallic response, making it spectroscopically indistinguishable from the substrate. This indicates a complete canceling out of all spin moments between the single Cr impurities rendering the dimer non-magnetic.

The situation is turned upside down once there is a small distance between the impurities. Now Fe adatoms (panel k) appear non-interacting yielding just the single impurity spectrum with a separation of less than 5 Å whereas the Cr pair (panel l) shows a remarkable change of its YSR features. Because of the strong perturbation that Cr creates in the superconducting condensate it can influence other impurities by interaction mediated through the superconductor over surprisingly large distances. This indirect coupling of Cr adatoms is a very promising finding and shall be explored thoroughly in the next section.

As a remark, the study is limited to dimers consisting of only one unique element. Mixing of species would largely exceed the time frame of the present work, despite surely posing an intriguing topic for a future investigation, potentially demonstrating even more tunability of these microscopic quantum systems containing just a small number of magnetic impurities coupled to a superconductor.
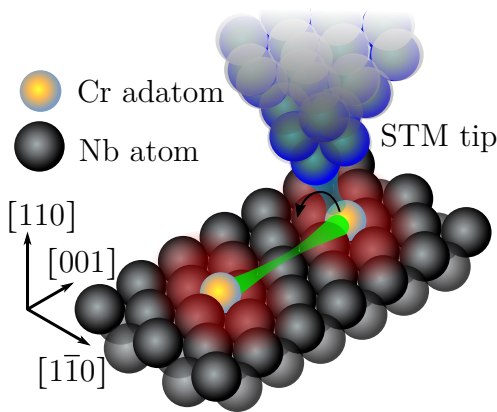
4.2 Indirectly coupled impurity spins

Figure: Coupled Cr atoms on Nb under the STM tip.

From single non-interacting impurities in the previous section the attention is now turned towards their mutual influence that becomes detectable when the distance between the adatoms is reduced. This is particularly interesting because it enables one to tune the magnet-superconductor interaction resulting in energy shifts of the induced YSR quasi-particles to create a wide variety of possible scenarios on demand through controlled manipulation. Long-range distance dependent and directional interaction favor a maximum flexibility.

As reasoned in the previous section, among studied $3d$ transition metal elements, Cr seems to be the most promising candidate to explore a wide parameter space. First, in analogy to YSR spectroscopy of single adatoms, hybridized Cr next-nearest neighbor dimers will be characterized via spatial mapping of their sub-gap states. In order to systematically evaluate the interaction as a function of dimer angle and spacing, a measurement and analysis protocol will be introduced before results are presented. Non-negligible coupling to oxygen defects shall be mentioned and additional insights from theory calculations are discussed, particularly with respect to the role of superconductivity in mediating an indirect magnetic coupling as was predicted by Yao *et al.*[82] Presented data has been published in *Nature Communications*[149].

4.2.1 Hybridization of YSR orbitals

To be able to identify interaction induced deviations with a maximum sensitivity and to correctly interpret them, it is meaningful to take another detailed look at the YSR states of single isolated chromium given in figure 4.8. Like already seen previously (figure 4.3), three different shapes of YSR states occurring in pairs symmetric around zero could be resolved resembling d_{z^2}, d_{xy} and d_{yz} orbitals with d_{z^2} being the dominating signal located very close to $\varepsilon_{\mathrm{YSR}} = 0$. Not separately detecting the d_{xz} and $d_{x^2-y^2}$ orbitals does not mean that they are necessarily without residual spin moment. The Nb crystal field may either leave them degenerate, push them into the quasiparticle continuum, or the experimental resolution and sensitivity is insufficient to detect them. By changing the measurement position relative to the adatom center, indicated here by **p1**, **p2** and **p3**, the detected intensity for YSR resonances changes for the three orbitals individually. Nevertheless, d_{z^2} which is most intense over the center remains the dominating peak even when measuring over the maxima of other orbitals located in outer rim positions as can be seen from figure
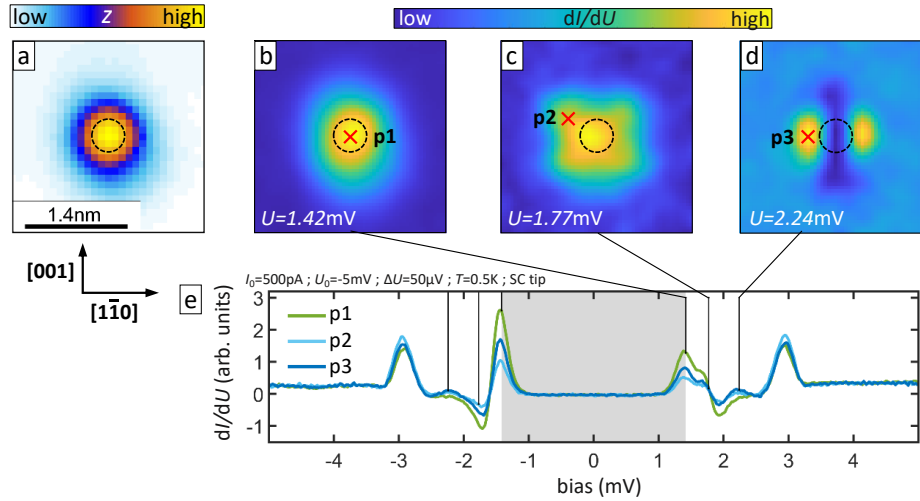
Fig. 4.8: **YSR orbitals of isolated Cr adatoms: a** STM topography of the measured
Cr atom. **b-d** dI/dU maps showing the same area like **a** at the respective
indicated energies. **e** STS at positions **p1**, **p2** and **p3** indicated by red crosses
in **b-d**. The grey area shows the energy range of the tip superconducting gap.

4.8e. Further one can note that particle and hole part of the d_{z^2} resonance are reduced
equally when moving away from the center, so that their relative spectral weight remains
unchanged.

An equivalent mapping has been done for pairs of close distance chromium atoms. Hy-
bridization of atomic orbitals generally leads to a shift plus a split in energy that poten-
tially results in a multiplet of peaks from bonding and antibonding states not symmetric
around the Fermi level[18,22]. Figure 4.9 shows three different dimers, created by controlled
atomic manipulation and aligned along crystallographic directions $[001]$, $[1\bar{1}0]$ and $[1\bar{1}1]$,
each of them exhibiting very different spectra reflecting the low symmetry of the (110)
surface lattice. An assignment of bonding and antibonding states can be done by the
dI/dU signal distribution being either more intense between the pair or away from its
center, respectively. However, ascription to the original single atom orbitals is hindered
by limitations in energy resolution and the resulting strong overlap between individual
peaks preventing a complete reconstruction of all shifts and splits. It is expected that
in the majority of cases d_{z^2} derived YSR signals maintain higher intensity due to their
longer extension into vacuum which allows to track their shifted energy position inside the
gap. Starting from the $[001]$ dimer in figure 4.9a, the dominant peak shifts remarkably
far towards negative energies suggesting significant impact of hybridization on impurity-
substrate coupling strength. In striking contrast, the orthogonal $[1\bar{1}0]$ dimer in panel
b shows opposite behavior. The strongest peak appears now in the unoccupied states
indicating a shift towards positive energies. It thereby crosses with its lower-intensity
counterpart through zero which signals a quantum phase transition between a free-spin
and a spin-screened ground state. An *a priori* determination of the initial state is not
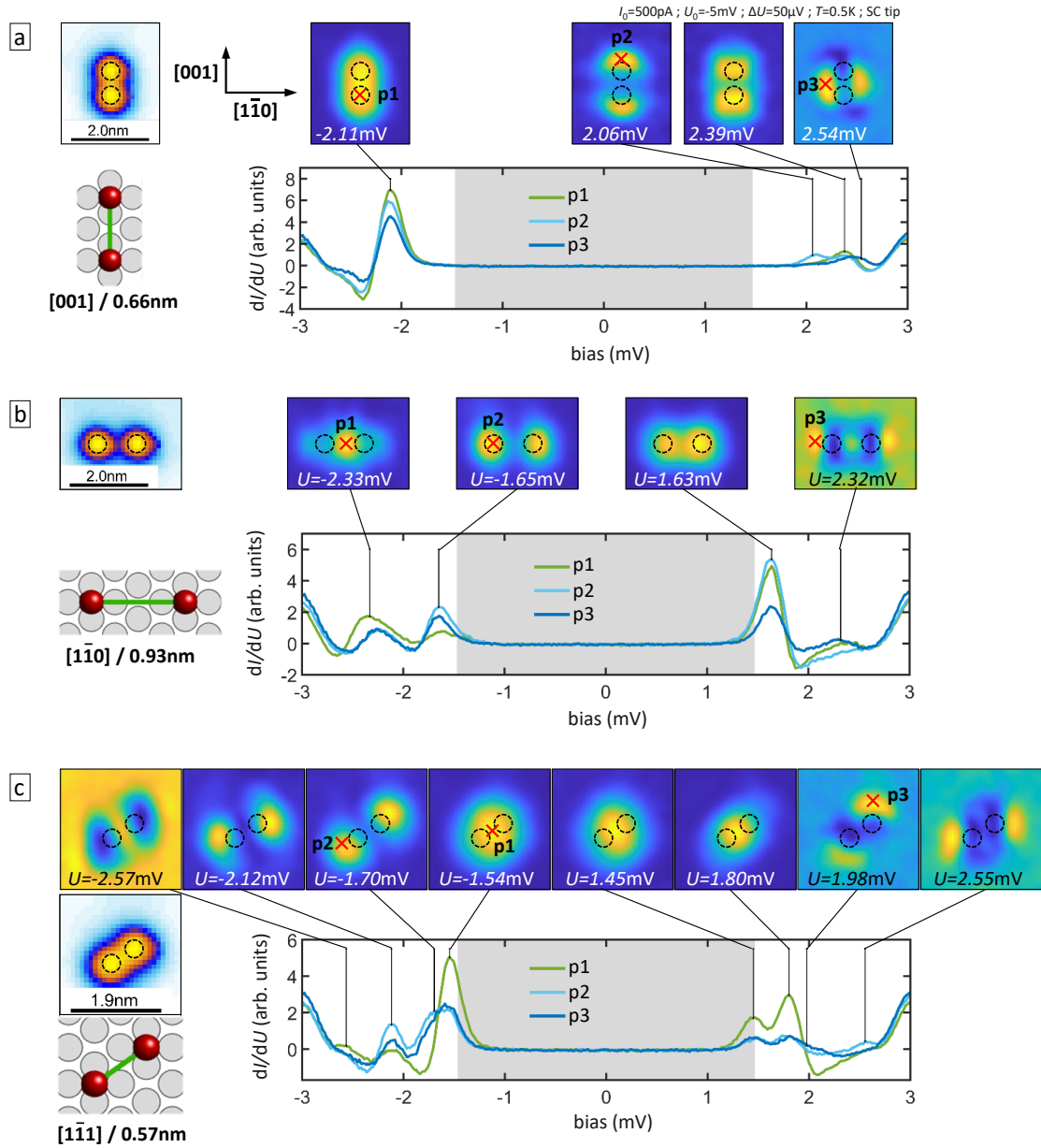
Fig. 4.9: **Hybridization of YSR orbitals in next-nearest-neighbor dimers:** Topography, lattice positions, dI/dU maps and STS in different positions around the dimer along directions **a** [001] ,**b** [1$\bar{1}$0] and **c** [1$\bar{1}$1] . Red crosses indicate STS coordinates **p1-3** and thin black lines respective energy positions of the dI/dU maps.

possible from spectral weight asymmetry[108] which is not essential here, however, it will be further discussed in section 4.3. Finally, the $[1\bar{1}1]$ dimer in panel c features a more complex sub-gap structure after hybridization with many resulting states at different energies. This scenario may partially be enforced by a smaller adatom spacing, however, the crystallographic direction alignment moreover brings different orbitals into play. While the d_{z^2} peak appears to be shifted only slightly negative in this case, in particular the d_{xy} state undergoes a stronger shift and gains in intensity. This seems consistent by considering the diagonal alignment.

To analyze a large number of dimer configurations, a limitation to the most intense d_{z^2} peak seems feasible by keeping in mind that multi-orbital effects can give rise to minor deviations. The error is small along high symmetry directions $[001]$ and $[1\bar{1}0]$, however needs to be considered along mixed directions. The concept of systematic evaluation of indirect dimer interaction via relative particle-hole intensities will be explained in the following.

4.2.2 Indirect coupling

Observations of mutual influence between dilute magnetic adatoms are interpreted as an indirect interaction mediated by the superconducting condensate of the Nb substrate where the induced quasiparticle wave functions overlap, reaching higher length scales compared to the direct magnetic exchange interaction which is rather short ranged[113] or conventional RKKY interaction on metallic substrates[90]. Remarkable findings have been made on 2D superconductors[24,27] visualizing the YSR wave function with the STM up to tens of nm around magnetic impurities embedded into the substrate due to a reduced decay into the third dimension, however, lacking the possibility to control impurity positions.

Figure 4.10a-c shows an illustration describing the principle of substrate mediated coupling. A single magnetic adatom sitting atop the surface of a superconductor induces quasiparticle resonances inside the superconducting gap that can be described in quantum mechanics by wave equations given in section 2.1.2. Due to their strong decay in three dimensions they are not detectable more than a nanometer away from the impurity within present experimental limits by just probing the bare Nb substrate. However, when a second adatom is closeby their similar wave functions overlap, creating an interference which results in an energy shift of the observed in gap resonance. The sharp and intense local peaks on adatoms therefore serve as antennas with their sensitivity to small interaction being orders of magnitude larger than the signal of actual quasiparticle traces in the substrate. That way the YSR wave function originating from one adatom can be probed with enhanced sensitivity by moving a second adatom to specific places around it, even at distances up to several lattice constants. Adatoms in close proximity, i.e. only separated
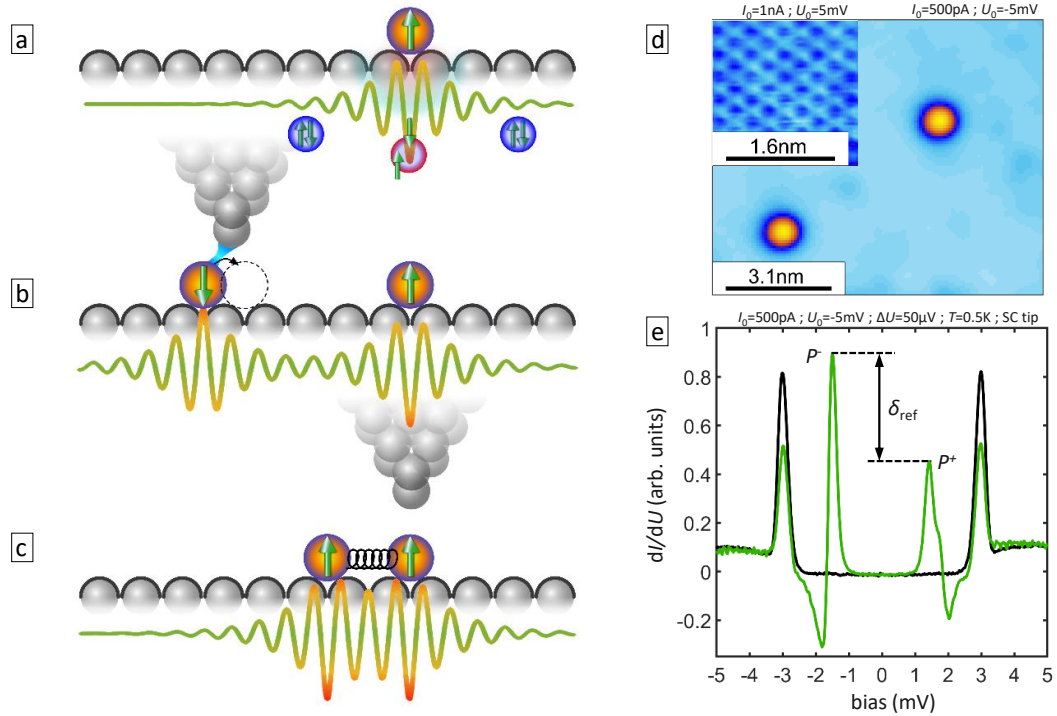
Fig. 4.10: **The experiment of two coupled impurities: a** A single magnetic impurity induces a quasiparticle into the superconductor by breaking a Cooper pair via magnetic exchange interaction that has a spatially extended wave function. **b** A second magnetic impurity is dragged closer to the first by STM atomic manipulation. Its YSR wave function interferes with the one of the first impurity so that their energies shift due to purely indirect interaction. **c** Two impurities closeby create hybridized orbitals and their magnetic moments are directly coupled by exchange interaction. **d** STM topography of two Cr adatoms in a clean Nb(110) area of approximately 10x10nm. Inset: atomic resolution image of Nb(110). **e** STS on single Cr impurity (green) used as the reference for this experiment with indicated negative and positive peak intensities P^+ and P^-, respectively, and their difference δ_{ref}. The bare Nb signal is drawn in black.

by one or two lattice constants, interact via direct and indirect hopping as well which was calculated in an *ab initio* study and will be presented after the experimental data.

The following experiment, aiming to shed more light on the coupling between local magnetic impurities on a superconductor, was carried out in a very systematic way several times and with very good reproducibility. Two Cr adatoms placed inside a 10x10nm clean Nb area were used[2]. One of them remained in a fixed position while the other was moved around to precisely known lattice sites. In every position both atoms have been measured to check consistent behavior, however, data used for interpretation was taken only from the atom which was not manipulated to exclude environmental effects other than the moving atom. A reference position (shown in figure 4.10d,e) was measured before and after atomic manipulations to exclude tip changes during the experiment and indeed confirmed consistency with perfect agreement. For analysis and interpretation of acquired spectra, a spectral weight parameter

$$\delta = P^- - P^+ \tag{4.3}$$

was defined, with in-gap maximum peak intensities P^- and P^+ below and above the Fermi level, respectively, intended to track a shift of the d_{z^2} state. It shall become clear in the following how it is useful to sense small changes in YSR energy.

4.2.3 YSR energy and spectral weight

To find out to which extend observed changes in peak intensities P^+ and P^- can be traced back to shifts in YSR energies $\Delta\varepsilon_{\mathrm{YSR}}$, the correlation has been tested in a simple simulation. It considers purely energy shifts of the d_{z^2} resonance around a Cr adatom on Nb. The sample density of states is modeled by a Dynes function overlapped with two Gaussian peaks symmetrically shifted $\Delta\varepsilon_{\mathrm{YSR}} = -0.2$meV around zero and with very different intensities drawn in figure 4.11a. Note that these initial peak intensities stay constant for the whole the simulation, whereas in reality they are a function of YSR energy, however, the variation is usually small and would trend to further enhance the desired effect that shall be demonstrated here[15,60]. The sample DOS is then convoluted with the tip DOS shown in figure 4.11b using the procedure explained in section 3.1.1. Despite adding only one out of three YSR pairs, the model signal can be matched to a good approximation of the experimental data as shown in panel c. In the next step, $\Delta\varepsilon_{\mathrm{YSR}}$ is varied and it can be seen from panels d and e showing several curves with different energy shift that, as $\Delta\varepsilon_{\mathrm{YSR}}$ approaches zero and both peaks overlap, their energy position becomes difficult to extract while the intensity significantly changes. Owing to the separation of positive and negative

---

[2]There are two exceptions: next-nearest-neighbor dimers along [1$\bar{1}$3] and [3$\bar{3}$1] which were acquired in different measurement runs. This does not impact the reliability of the present experiment since coupling at this distance has obvious impact on the energy of in gap states so that the interpretation does not rely on tiny effects possibly affected by different microtips.
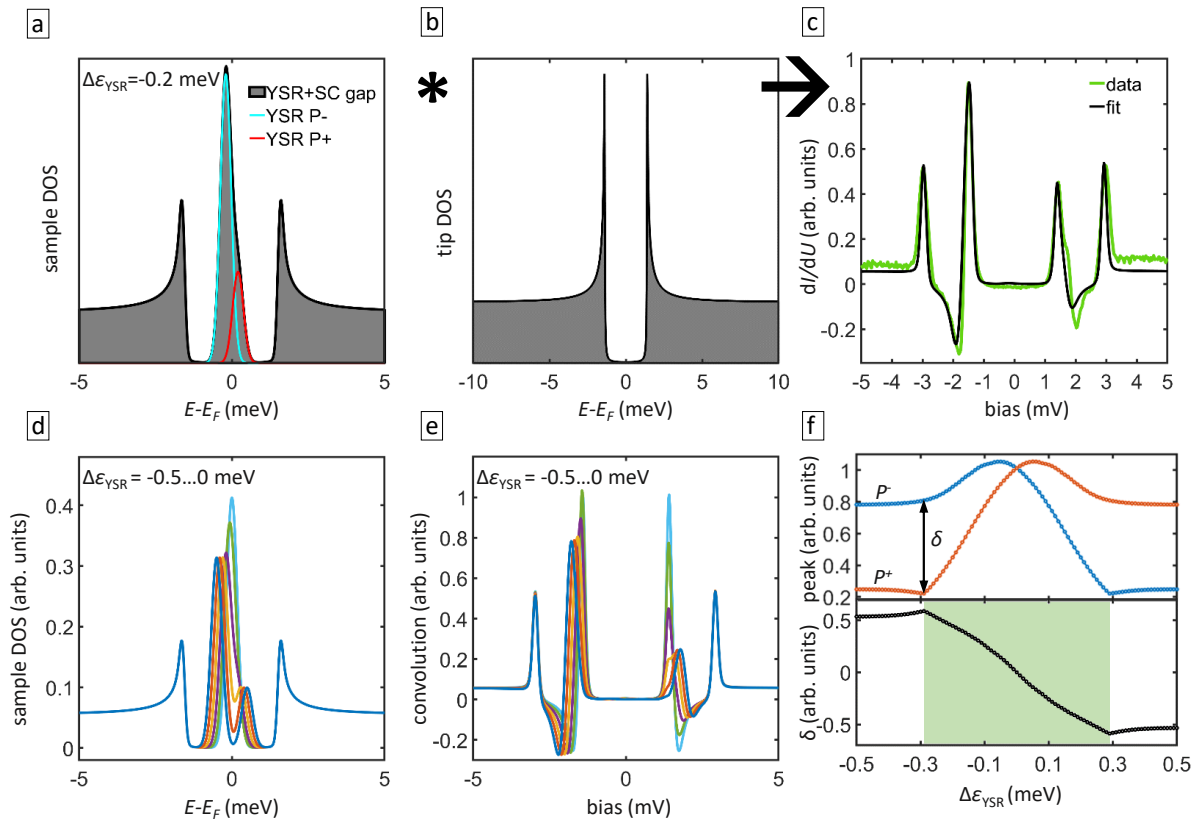
Fig. 4.11: **Signal simulation for YSR energy shifts $\Delta\varepsilon_{\mathbf{YSR}}$: a** Modeled sample density of states in a range ±0.5meV around the Fermi level by considering only the YSR pair originating in the d_{z^2} orbital of a Cr impurity on Nb. **b** Modeled tip DOS in ±10meV. **c** Convolution of **a** and **b** (black) overlapped with the measured signal on isolated Cr. **d,e** Sample DOS and convoluted signal for different $\Delta\varepsilon_{\mathrm{YSR}}$ from -5 meV to 0. **f** Peak intensities P^+ and P^- as well as their difference δ as functions of $\Delta\varepsilon_{\mathrm{YSR}}$. The green area marks the region of approximately linear correlation for energy shifts between ±0.3meV.

part of the spectrum by the effect of the superconducting tip, the values P^+ and P^- are extracted easily (panel f). Within a range of small energy shift $-0.1\text{meV} < \Delta\varepsilon_{\text{YSR}} < 0.1\text{meV}$ they are nicely anticorrelated representing the transfer of spectral weight between each other. Their difference δ even exhibits an almost linear correlation to $\Delta\varepsilon_{\text{YSR}}$ within the full range of overlapping peaks which is approximately $\pm0.3\text{meV}$ in the simulation. This means that especially for small changes in YSR energy, the spectral weight parameter δ is a valuable qualitative probe of high sensitivity. Additionally, sign changes are indicators of a quantum phase transition and the referenced value $\Delta\delta = \delta_{\text{ref}} - \delta$ should reproduce the sign of $\Delta\varepsilon_{\text{YSR}}$.

4.2.4 Directionality of the interaction between close distance dimers

The first set of data is displayed in figure 4.12 and investigates dimers with next-nearest-neighbor spacing aligned along five non-equivalent crystallographic directions. The Nb(110) substrate surface lattice offers a twofold symmetry which is also reflected in its projected Fermi surface depicted in figure 4.12d calculated from DFT. The constant energy contour in momentum space is in the literature sometimes simplified to a stadium shape in first order approximation[155], however, in general it suggests a more complex anisotropic coupling whenever the interaction is mediated by the substrate. Note that not only the angle but spacing varies as well due to the restriction of adatoms to hollow lattice sites, still the focus in this comparison lies on directionality since it is presumably the dominant factor. To support this assumption one can compare dimers $[1\bar{1}1]$ and $[1\bar{1}3]$ giving significantly different spectra despite having nearly equal distance. This is a first confirmation that indeed the substrate plays a crucial role for the interaction of two non-nearest-neighbor magnetic impurity spins. On the contrary, as seen in the previous section in figure 4.7, for nearest-neighbor adatoms only the direct antiferromagnetic exchange matters leaving the superconducting condensate unaffected. Comparing all five directions by looking at figure 4.12b and c, a remarkable impact of the dimer angle on the coupling is observed, i.e. having two configurations versus three on either side of the quantum phase transition between a free spin and spin screened ground state regime. Interestingly, the high symmetry directions corresponding to angles 0° and 90° mark also the two opposite extremes in YSR energy shift with $[001]$ towards negative and $[1\bar{1}0]$ towards positive energies. Mixed directions do not show a monotonic trend with increasing angle, rather the QPT is crossed several times in an oscillating manner. This is likely a manifestation of the complexity of the projected Fermi surface. The ability to alter the angle by atomic manipulation on demand allows great tunability already in this first step. Briefly revisiting the comparison to Fe[31] and Mn[29], interacting Cr adatoms have a considerably larger effect on the sub-gap structure at these spacings. It is likely the only element making a distance dependence study to map the YSR wave function
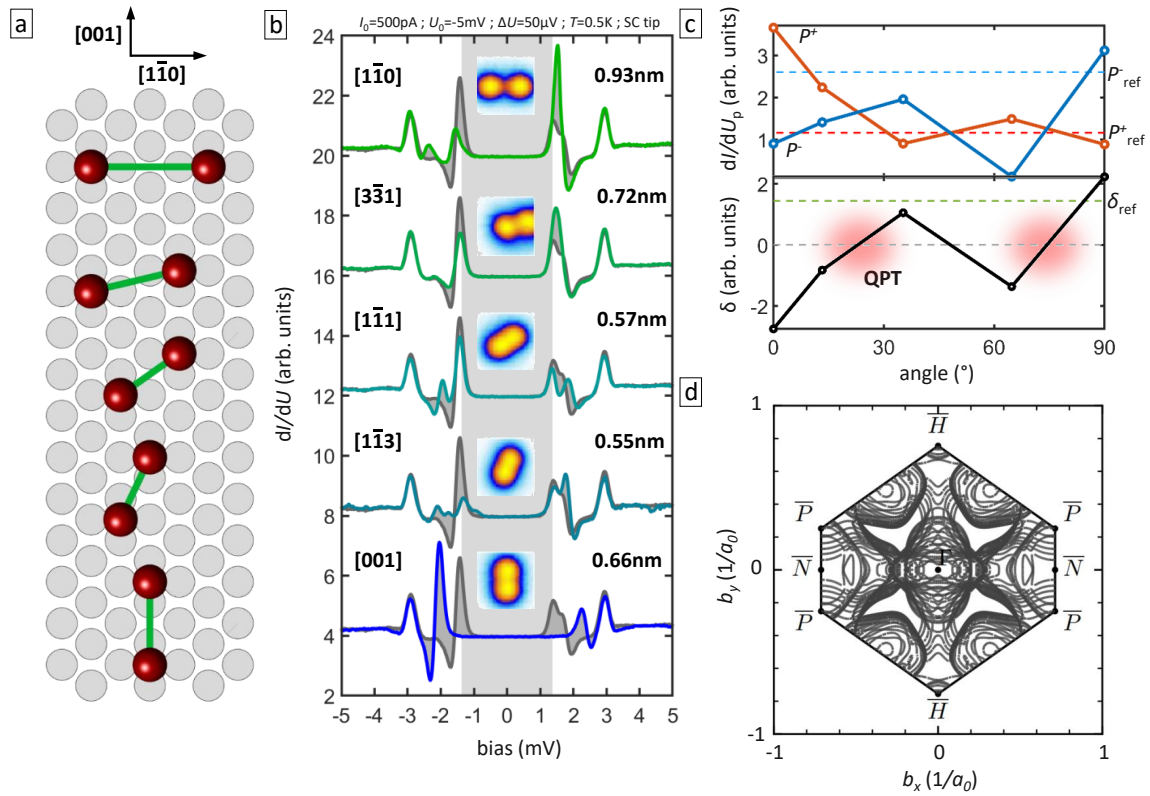
Fig. 4.12: **Dimer angle dependence at next-nearest-neighbor distance: a** Dimer configurations on the Nb(110) lattice. **b** STS on five different dimers measured on top of one atom of the dimer and vertically shifted for clarity. Crystallographic directions are indicated to the left and inserts show topography scans. **c** Peak intensities P^+ and P^- and their difference δ over the dimer angle where $0°$ means $[1\bar{1}0]$. Reference values for the isolated Cr adatom are indicated by respective dashed lines. Red shaded areas suggest angles of occurring quantum phase transitions where P^- crosses the Fermi level from negative to positive. **d** Fermi surface of Nb projected in the (110) plane from DFT calculations.

possible.

4.2.5 Directional and distance dependence

It shall be delightful to investigate up to which distances the superconducting condensate mediates impurity-impurity interaction. One would conventionally expect a fast decay since known metallic RKKY interactions should be restricted by the reduced number of spinful free charge carriers through the formation of Cooper pairs.

Quite astoundingly this is not the case as it is demonstrated in the measurement data shown in figure 4.13. Panels a,b,c show dI/dU signals subtracted by the isolated atom reference spectrum. Separating the atoms step by step away from each other, despite a clear decay of the coupling strength it does not cease and can be sensed up to 4 nm along the crystallographic [001] direction which corresponds to eleven Nb(110) hollow sites in between the adatoms. Considering the substrate being a 3D bulk superconductor this is
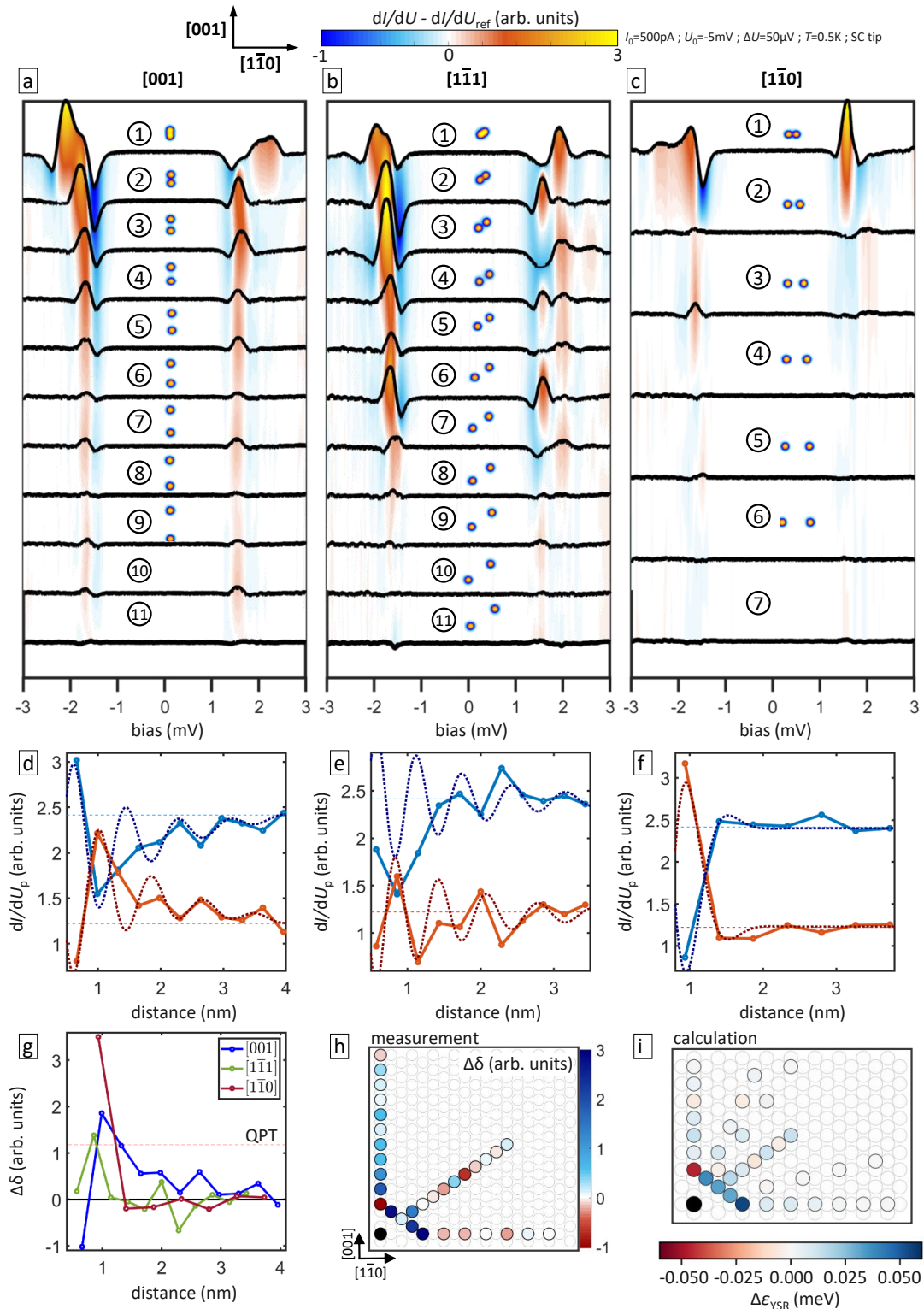
Fig. 4.13: **Dimer distance dependence: a-c** Difference in dI/dU signals between dimer and single Cr reference along indicated crystallographic directions. Insets show topography scans of respective dimers, numbers indicate the separation in discrete lattice steps starting from next-nearest-neighbor positions. **d-f** Peak intensities P^+ and P^- for respective directions over the dimer distance. Dashed lines are guides to the eye that suggest an oscillating behavior of the signals. **g** $\Delta\delta = \delta_{\mathrm{ref}} - \delta$ over distance for all three directions. **h,i** Maps of various dimer configurations where a fixed adatom is drawn in black and a second in colorscale on corresponding lattice sites. The scale shows for **h** the value $\Delta\delta$ measured and for **i** the calculated value $\Delta\varepsilon_{\mathrm{YSR}}$ from theory.

a remarkable distance[24]. Note that, as explained previously, these results are robust and reproducible, therefore there is no doubt about the observation of a long range coupling effect.

The second unambiguous result is the confirmation of strong anisotropy in the coupling expressed in clear directionality regarding the maximum interaction distance. Contrary to $[001]$, along the crystallographic $[1\bar{1}0]$ direction a short decay length brings both adatoms close to the isolated case after only one step, corresponding to $1.39\,\mathrm{nm}$ spacing. The reason for this large discrepancy is again likely rooted in the Fermi surface (figure 4.12d). Its shape can act like a lens focusing propagating waves depending on their energy to beams along certain directions of good momentum space nesting vectors[110]. Energy conservation inevitably leads to intensity reduction along non-focused directions. However, the direction of focused beams can differ between the various YSR states due to energy, i.e. momentum vector, dependence. While along the high symmetry directions $[001]$ and $[1\bar{1}0]$ the dominant effect seems to be a shift of the d_{z^2} state, spectra along the mixed $[1\bar{1}1]$ direction suggest that the observed long range coupling up to $3.5\,\mathrm{nm}$ happens between d_{xy} states (comapare to orbital mapping in figure 4.9).

A third observation is presumably related to the actual wave function representation in real space. Despite a limited spatial resolution due to discrete lattice increments, both long range vectors, i.e. $[001]$ and $[1\bar{1}1]$, quite clearly exhibit alternating and periodic signal variations. It can be grasped from figure 4.13a,b and is pointed out in panel d-f, plotting intensities P^+ and P^- over distance, by dotted lines suggesting a damped oscillation. A phase shift of π between electron- and hole-like peak signal demonstrates the transfer of spectral weight between P^+ and P^-. The aforementioned hollow site sampling restiction makes an exact measurements of the oscillation period impossible, however, best fit values $\lambda_{001} = 0.82\mathrm{nm}$ and $\lambda_{1\bar{1}1} = 0.68\mathrm{nm}$ are on a meaningful order of magnitude compared to the literature[24]. The frequency should be on the order of twice the Fermi wave vector k_F originating from two interfering waves in opposite directions. Given the complex and non-trivial Fermi surface an extraction of the value k_F is not meaningful.

Finally, the referenced spectral weight parameter $\Delta\delta$ is analyzed in panels g and h which is within boundary conditions and tolerance connected to an energy shift of the d_{z^2} YSR state $\Delta\varepsilon_\mathrm{YSR}$. In that, zero marks the border between positive and negative shift compared to the reference and the red dashed line indicates the QPT. Interestingly, all three directions have QPT crossings around $1\,\mathrm{nm}$. Further increasing the distance, for $[001]$ the sign stays positive, $[1\bar{1}0]$ weakly negative and $[1\bar{1}1]$ has alternating sign. Panel h shows a map giving a color coded overview over $\Delta\delta$ in all 31 measured positions. The equivalent plot for the theory results of $\Delta\varepsilon_\mathrm{YSR}$ shows a remarkable agreement for the short distance configurations, catching the correct signs of the shift, however, for higher distance it becomes less accurate and the damping is predicted to be stronger than observed in the experiment. The discrepancy can be explained in several ways: (i) the extremely small
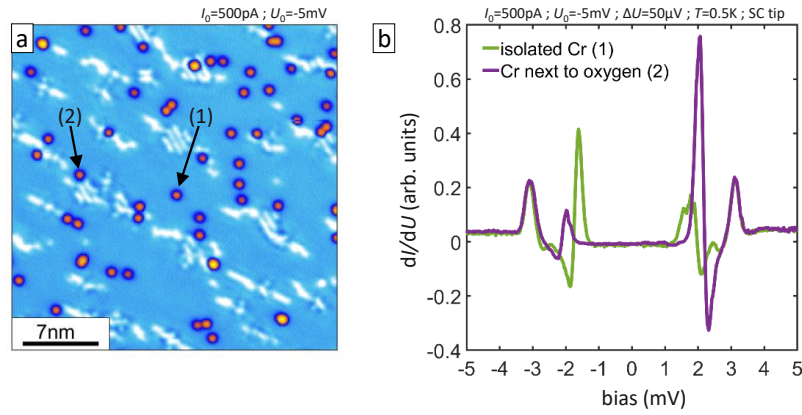
Fig. 4.14: **Coupling to oxygen defects: a** Topography scan of an area with oxygen defects (white) and magnetic adatoms (10mV/500pA). Arrows indicate measured Cr adatoms. **b** STS on isolated Cr and Cr close to an oxygen structure, corresponding to arrow with label (1) and (2) in **a**, respectively.

energy scales tackled by the theory highlight the cutting-edge computational methods in use, however, longer dimer distance and small hopping terms make results progressively susceptible to numerical errors, (ii) both theory and spectral weight parameter analysis omit multi-orbital effects and intensity changes due to normal state DOS and Coulomb potential[60,64], and (iii) although the calculation does consider indirect hopping through the substrate, the macroscopic wave function and YSR quasiparticles are not included in the model since a first-principles implementation is out of reach for today's computational resources. Nevertheless, this especially highlights a crucial role of superconductivity in the substrate-mediated interaction leading to significantly higher range confirmed in the experiment than theoretically predicted. Some more detail on the calculation will be given in the final paragraph of this section.

4.2.6 Interaction with non-magnetic adsorbates

At this point, a brief remark about the influence of non-magnetic adsorbates, in particular oxygen as the main contaminant on Nb(110) surfaces, shall be made. It is important to note that YSR states are not exclusively influenced by magnetic interaction. Local changes of the substrate surface can likewise have an effect on impurity-substrate coupling.

An example is given in figure 4.14. Measurements indicate a similar lateral range compared to Cr-Cr coupling. In the topography (panel a) the adatom (2) appears very close to an oxygen patch which is ordered in a typical NbO stripe-like formation[116]. The exact lattice position relative to the defect was not determined. dI/dU measurements reveal a strong deviation from the isolated Cr atom (1). The dominating peak is shifted towards positive energies and crosses the quantum phase transition indicative of a presumably reduced impurity-superconductor coupling J in the vicinity of the defect. Remarkably, this shift is even stronger than the largest positive shift observed for pure Cr-Cr coupling
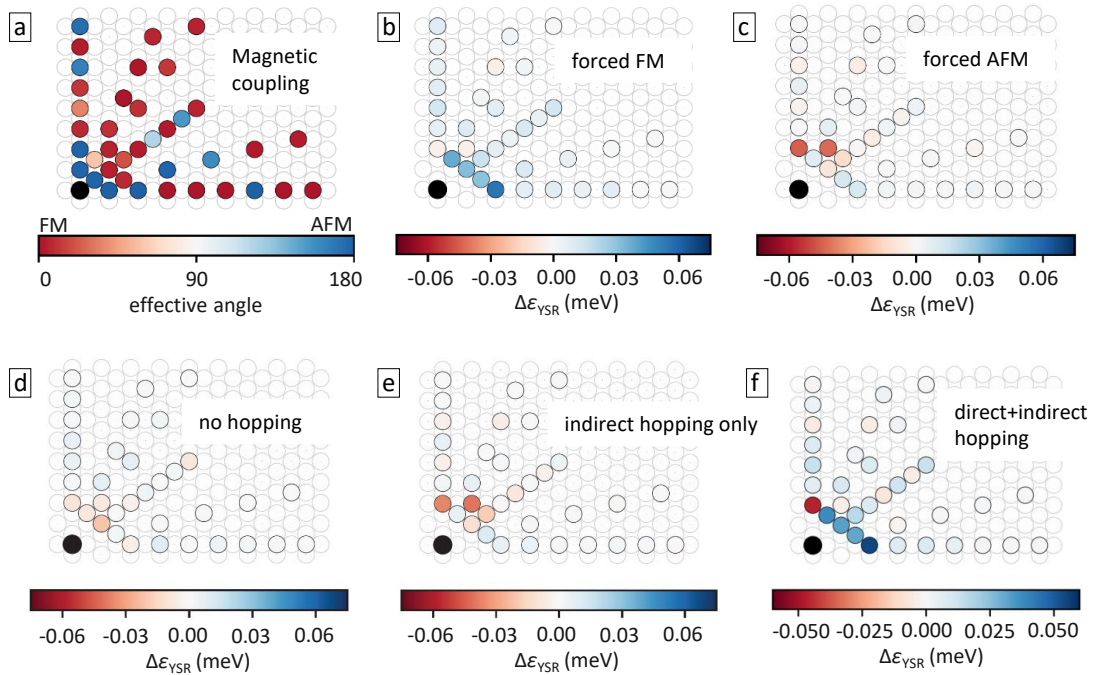
Fig. 4.15: **Theory results on Cr dimer magnetic interaction:** Real space map of adatom pairs (fixed atom black, moved atom in colorscale) **a** Angle between the magnetic moments resulting from combined exchange and DMI interaction. **b,c** Result for the YSR energy shift assuming purely FM and AFM coupling, respectively. **d-f** Role of direct and indirect hopping terms for the interaction: **d** both switched off, **e** only indirect term on, **f** full model.

along $[1\bar{1}0]$ at a distance of $0.93\,\mathrm{nm}$. On the one hand, it is a clear sign that one needs to pay attention to closeby oxygen defects when studying interaction between magnetic impurities to avoid unwanted influences in the data. On the other hand, it demonstrates that the range of tunability for YSR states at hand becomes even greater when considering surface defects. A systematic experiment in a similar style to the Cr-Cr interaction might prove a fruitful study for a future work. However, strong constrains are given by unfeasible atomic manipulation for oxygen which is strongly bound in NbO surface structures, hence it escapes the ultimate control that is the main advantage of the present system under investigation. Therefore, close proximity of measured adatoms to oxygen defects was avoided wherever possible.

4.2.7 Theoretical insights

To be able to elucidate the effect of single parameters separately, it is interesting to calculate the resulting YSR energy shift assuming or forcing certain parameters instead of using results from the fully realistic model for subsequent calculations.

This is visualized in figure 4.15 for the angle between the magnetic moments in the upper and for the electron hopping in the lower panels. First, panel a shows the theory

prediction of the real effective angle between the moments which will be in part verified experimentally at a later stage. It is obtained by minimizing the generalized Heisenberg model containing the on-site anisotropy, the exchange interaction and the Dzyaloshinskii-Moriya interaction. The significance of this result becomes clear when comparing the theoretical value for $\Delta\varepsilon_{\mathrm{YSR}}$ by forcing a purely ferromagnetic (b) or antiferromagnetic (c) coupling between the Cr adatoms which leads to very different shift with in many cases opposite effect on the energy shift. While FM coupling tends to shift towards positive, AFM alignment shifts more towards negative energies. Interestingly, it seems that the real magnetic alignment prefers the respective stronger shift.

Looking at the role of direct and indirect coupling terms separately, the indirect substrate mediated hopping term affects the Fermi surface focused [001] direction the most, yet the dominant role in this model is played by direct hopping. The good agreement with experimental data on next-nearest neighbor dimers confirms a crucial role of direct hopping for these distances.

Summary

In summary, a coupling of two magnetic impurities could be observed and verified between $0.55\,\mathrm{nm}$ up to $4\,\mathrm{nm}$. It shows a strong directionality explained by the anisotropy of the superconducting substrate mediating the interaction through YSR quasiparticles which have been probed by STS. Coupled YSR states undergo a shift in their energy which is detectable as long as they stay below the superconducting gap edge. Inevitable limitations of experimental energy resolution create peak overlaps which hinders the measurement of energy shifts directly. Instead, evaluating the spectral weight asymmetry takes advantage of the high sensitivity in signal intensity. This revealed an oscillatory character of the interaction in space suggesting its origin to be quasiparticle waves with a period related to the Fermi wave vector k_{F}. Theoretical predictions for close distance interaction effects show very good agreement demonstrating the capability of cutting-edge numerical calculations while at the same time limitations of the theoretical approach for longer distances have been revealed. With a minimum number of 25 different indirect coupling configurations experimentally verified and presumably several possible cases more including quantum phase transition crossings, the ability to manipulate coupled impurities in space creates an unprecedented flexibility and tunability in a quantum spin-to-superconductor interface.

4.3 Anomalous spin excitations

Switching off superconductivity, this section enters the field of atomic-scale magnetodynamics in a metallic environment. Once more, research in this field poses a perfect match

with high-resolution STM as a local probe. It allowed to investigate fundamental phe-nomena such as magnetic[133,156–164], vibrational[165], polaronic[166], excitonic[167] or Kondo excitations[151,159,168–170] on single atoms. There is not always a straight forward way to distinguish their spectral shapes, especially if different magnetic processes are expected to occur simultaneously as it is the case for the present study where Kondo effect and spin excitations are expected. Both mechanisms give a possible explanation for the ac-quired data. Their spectral shapes share a similar origin involving magnetic interaction of conduction electrons with defects, however, their fundamental nature is quite different (see section 3.1.1). The recent discovery of unconventional spin excitations being at play in the spectral signature for Co adatoms on Cu, Ag and Au surfaces around the Fermi level[134] motivated the exploration of a similar mechanism for Cr on metallic Nb. There-fore the experimental results will be discussed in the spin excitation framework, however, the focus shall remain on the bare observations. Presented data has been published in *Science Advances*[150].

4.3.1 Magnetic field dependence

To create a clean and undisturbed environment for a single Cr adatom, it was isolated by atomic manipulation to have a $6\,\text{nm}$ clean radius around it as shown in figure 4.16a. The systematic study of different adatom elements in the metallic regime already unveiled a sharp step-like feature at zero bias with the onset within $-1\,\text{mV}$ from zero and a maximum around $0.5\,\text{mV}$ which appears stronger compared to features on other elements due to lower density of states at the Fermi level. All spectra shown here were taken at $600\,\text{mK}$ unless stated differently.

Figure 4.16b compares the spectra taken on bare Nb and on top of a Cr adatom each measured at zero magnetic field and an externally applied field of $1\,\text{T}$ out of plane to fully suppress superconductivity and thereby revealing the zero bias feature otherwise covered by the gap. According to theory the small in-plane anisotropy of Cr is overcome by the applied field so that the magnetic moment changes direction from in plane to out of plane, however, experimentally no difference in spectral shape was confirmed whether applying the external field in or out of plane. Further, comparing both Cr curves, exactly the same step height is confirmed away from the superconducting gap for both 0 and $1\,\text{T}$. Therefore it can be assumed that no considerable impact on the fundamental shape of this feature is induced by the applied field.

To measure its evolution with increasing magnetic field, an out of plane field up to $6\,\text{T}$ has been used corresponding to the maximum field available in the used system. As a remark, $\text{d}I/\text{d}U$ maps at several different energies around the zero-bias feature (not presented here) reveal it to be fully isotropic within the limit of experimental resolution. The results presented in panel c show a broadening effect with increasing magnetic field.
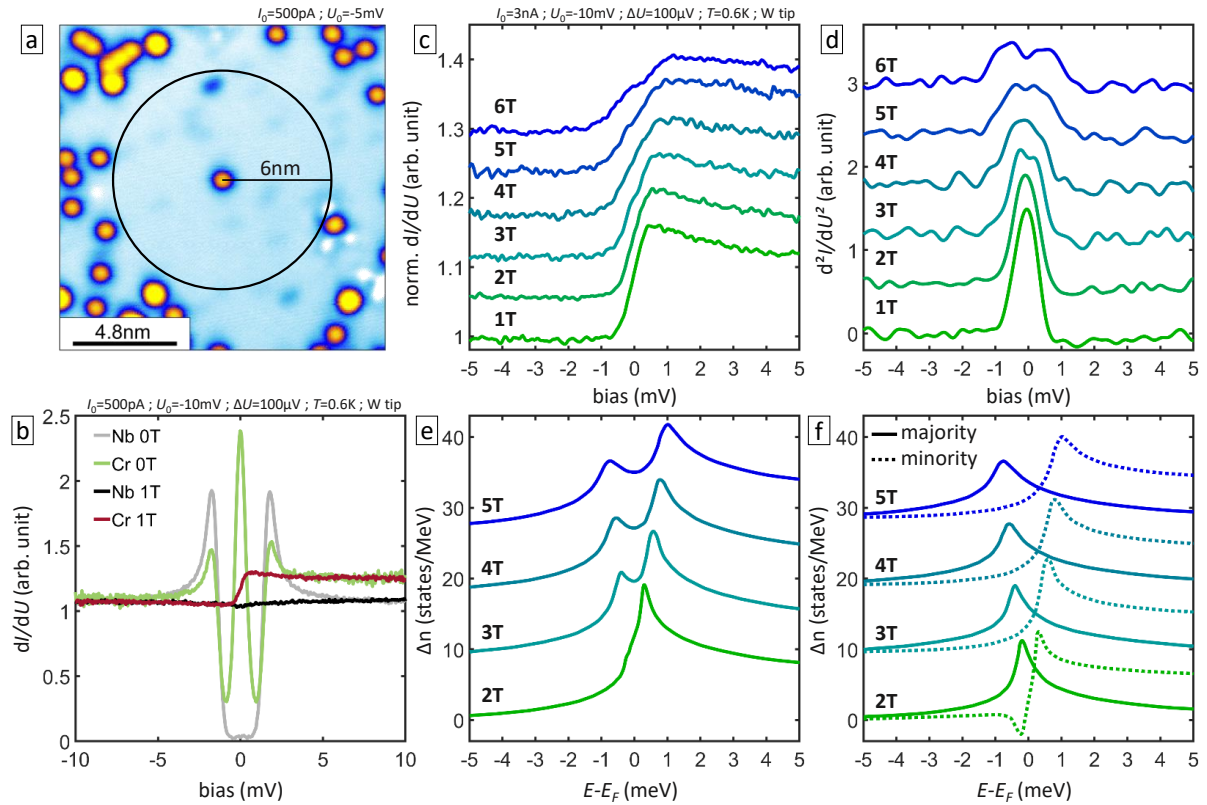
Fig. 4.16: **Magnetic response of Cr on Nb(110): a** STM topography scan of the measurement area. A black circle indicates a 6 nm radius free of other adatoms around the Cr atom which provided the presented data. **b** STS on a Cr adatom compared to substrate area each with superconductivity on (0T) and off (1T). **c** Evolution of the signal on Cr with magnetic field. **d** Derivative of data in **c** to help identifying a split into two separate features. **e** Calculated magnetic field dependence of a spin excitation effect on the density of states. **f** Spin resolved signal from **e**.

A closer look reveals the emergence of a splitting into two separate features, foreshadowed as a double step in the raw data at 6 T. The occurrence of a splitting is better visualized in the derivative (panel d) suggesting two separate peaks already at 3 T.

Panels e and f of figure 4.16 present the results obtained from *ab inito* by combining relativistic time-dependent density functional theory and many-body perturbation theory. In that, the very low magnetic anisotropy of the Cr spin moment allows conduction electrons to excite spin-flip processes at low energies in inelastic tunneling events. They can be described by quantification of the excitation probability in terms of the density of spin-flip excitations. This in turn affects the density of conduction electrons leading to the spectroscopic signatures in tunneling experiments and which is theoretically reproduced without relying on experimental parameters or fitting. It can be understood as the sum of majority and minority spin channels, shifted to opposite directions by the magnetic field eventually leading to a broadening and the emergence of two separate peaks. This is shown in panel f with a peak-like and a step-like feature for the majority and minority
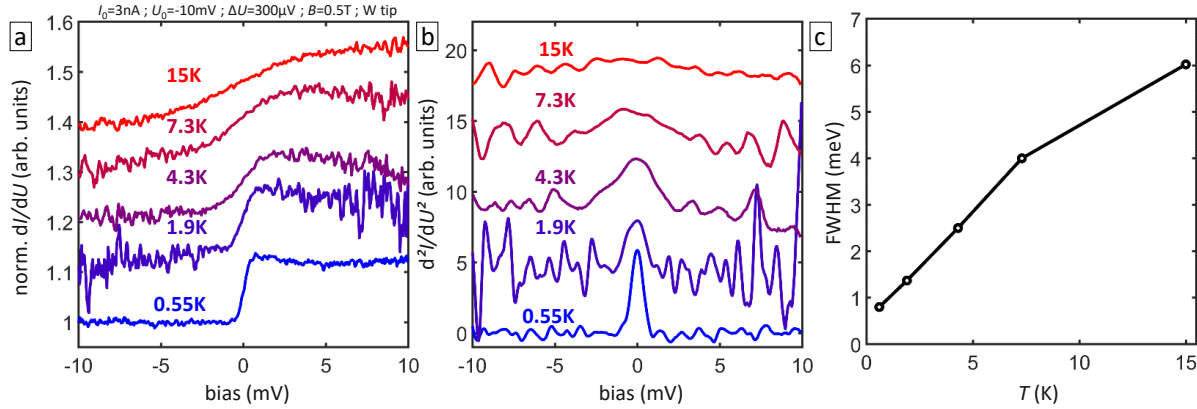
Fig. 4.17: **Temperature dependence of zero-bias feature: a** Raw spectroscopic data for various temperatures at a magnetic field of 1 T and vertically shifted for clarity. **b** Corresponding derivatives of **a**. **c** The broadening in terms of the full width half maximum (FWHM) over temperature.

spins, respectively. Their intrinsic broadening is connected to the lifetime of underlying spin-flip excitations.

In conclusion, the trend observed in the experiment could be nicely captured by a theoretical *ab inito* model assuming spin excitations. It is especially a remarkable achievement since the calculation produces all parameters self-consistently. However, despite providing a valid explanation, it does not serve as an unambiguous proof that spin excitations are the origin of the measured signal since a Kondo signature would also be expected to show broadening and splitting with increasing magnetic field.

4.3.2 Temperature dependence

Another indicator with the potential to help distinguishing the origin is temperature. The entanglement of the impurity spin with the electron bath of the underlying metal leads to a screening in the Kondo picture within a certain energy scale defined by the Kondo temperature. Above this temperature the conduction electrons would enter a weak coupling regime to the spin moment of the impurity resulting in a breakdown of the Kondo effect. In section 4.1 the Kondo temperature of Cr, Mn and Fe has been estimated by a Frota fitting yielding a temperature of ≈ 9K for Cr. Measurements of the Cr zero bias feature at 1 T at elevated temperatures are presented in figure 4.17. Both raw data and derivative show the expected broadening due to thermal excitations following Fermi-Dirac statistics. No sign of splitting appears in the data, ruling out artifacts related to the experimental setup in the measurement of magnetic field dependence. Interestingly, the step-like feature persists up to the highest temperature measured which is 15 K, well above the estimated Kondo temperature of Cr on Nb. This simple finding supports and justifies the spin excitation approach which is still rather unconventional in the magnetic impurity-on-metal community. However, one can still argue that different Kondo channels
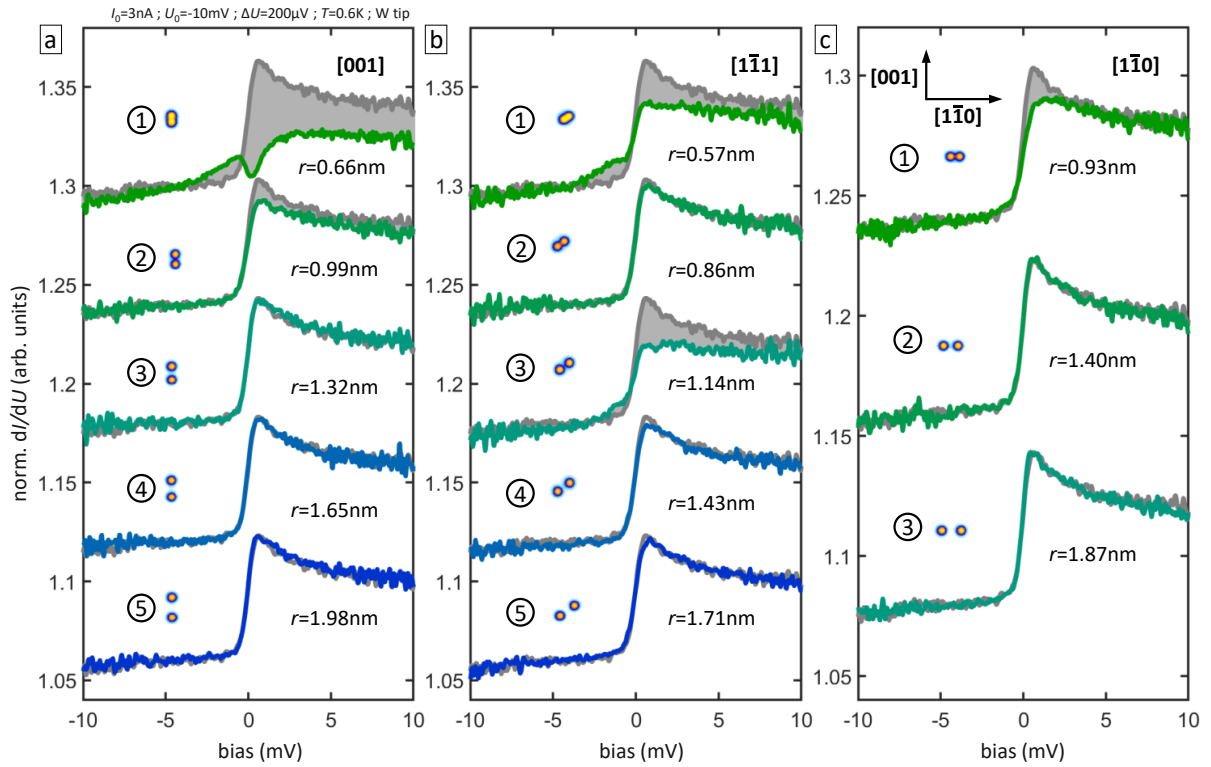
Fig. 4.18: **Dimers in the metallic regime:** Normalized dI/dU spectra on Cr dimers (color) each overlapped to the single Cr reference (grey) and displaced on the y axis for clarity. Three crystallographic directions are shown each with several distance steps where 1 means the next-nearest neighbor position. Topography scans of the dimers are depicted as small insets and the atom separation r is indicated.

corresponding to the d orbitals are overlapped and that only the sharpest of them vanishes leaving the one with higher Kondo temperature persisting.

4.3.3 Dimer interaction

Similar to the experiment described in section 4.2.5 for the superconducting regime, the interaction of two local spins has been investigated in the metallic regime. Substrate mediated coupling can now be explained as conventional RKKY interaction. It becomes clear from the data presented in figure 4.18 that the adatom's mutual influence has a significant impact on their dI/dU spectra, however, exhibiting a shorter range as compared to the superconducting phase. Confirmed deviations from the isolated atom reaching not longer than 1.4 nm, the range is consistent to values reported in the literature for RKKY interactions in a similar system[90]. Note that this is another strong indication for the crucial role of superconductivity in mediating an interaction between magnetic impurities, enhancing the coupling distance by more than a factor 2. Anyway one has to keep in mind that experimental sensitivity presumably receives a boost by the sharpness of YSR resonances used for detecting these interactions which could also account for an

enhancement in the detection range.

All presented data were again taken on the atom in a fixed position on the Nb surface. The [001] direction dimer (figure 4.18a) exhibits the largest difference compared to the single Cr reference in the closest, i.e. the next-nearest neighbor position, with a significant broadening of the step and a dip close to zero. As a side remark, in case of a Kondo interpretation, this would suggest an enhanced impurity-substrate coupling which, together with the negative shift of ε_{YSR} observed before, could identify an initial spin-screened ground state for the d_{z^2} orbital of an isolated single Cr impurity. Additionally, the step height is strongly reduced which is an effect not observed for the broadening related to magnetic field and temperature. Already in the second step, corresponding to $0.99\,\text{nm}$ distance, the overall shape is very similar to single Cr with slightly reduced step height, and for larger distances the deviation is below the detection tolerance. Next, $[1\bar{1}1]$ dimers (panel b) yield a spectrum featuring still a sharp step at zero but without a peak following the step like on single Cr. Further, a broader weak feature appears at negative energies before the step. A remarkable phenomenon along $[1\bar{1}1]$ is the observation of an on-off behavior. It means that the third step looks almost identical to the single Cr case whereas the following fourth step yields again a strong deviation similar to the second step. This could be reminiscent of the oscillations typical for RKKY interactions, however, poorly resolved due to the hollow site limitation. Moreover, it leaves no doubt that the coupling behaves differently along directions [001] and $[1\bar{1}1]$ which is an expression of the substrate surface anisotropy therefore revealing its role in mediating the interaction. Distances longer than $1.14\,\text{nm}$ did not show significant effects. Finally, the $[1\bar{1}0]$ direction shows the weakest effect when comparing all first step spectra which is at the same time the one with largest separation between the atoms. It is no surprise that already the second step having the atoms separated by $1.4\,\text{nm}$ returns to the single Cr spectrum.

This is confirmed by the theoretically obtained parameters for the exchange coupling J for the case of next-nearest neighbor dimers with $7.94\,\text{meV}$, $-8.95\,\text{meV}$ and $1.24\,\text{meV}$ along [001], $[1\bar{1}1]$ and $[1\bar{1}0]$, respectively, where positive values correspond to antiferromagnetic and negative to ferromagnetic coupling. For the theoretical analysis, the assignment of ferromagnetic ($[1\bar{1}1]$) and antiferromagnetic ([001] and $[1\bar{1}0]$) dimers is very important. As already mentioned this was experimentally confirmed as will be shown in section 4.5. Based on the spin susceptibility over excitation energy obtained from the TDDFT model it can be deduced that antiferromagnetic dimers are subjected to stronger electron-hole excitations resulting in a larger broadening, i.e. shorter lifetimes, of spin excitations in contrast to the ferromagnetic case (see Brinker *et al.*[150]). Like shown in figure 4.16 for the single Cr, individual alternation of the spectral shapes for majority and minority spin electrons could explain the complex signals measured by STS that were indeed suggesting two separately evolving features.
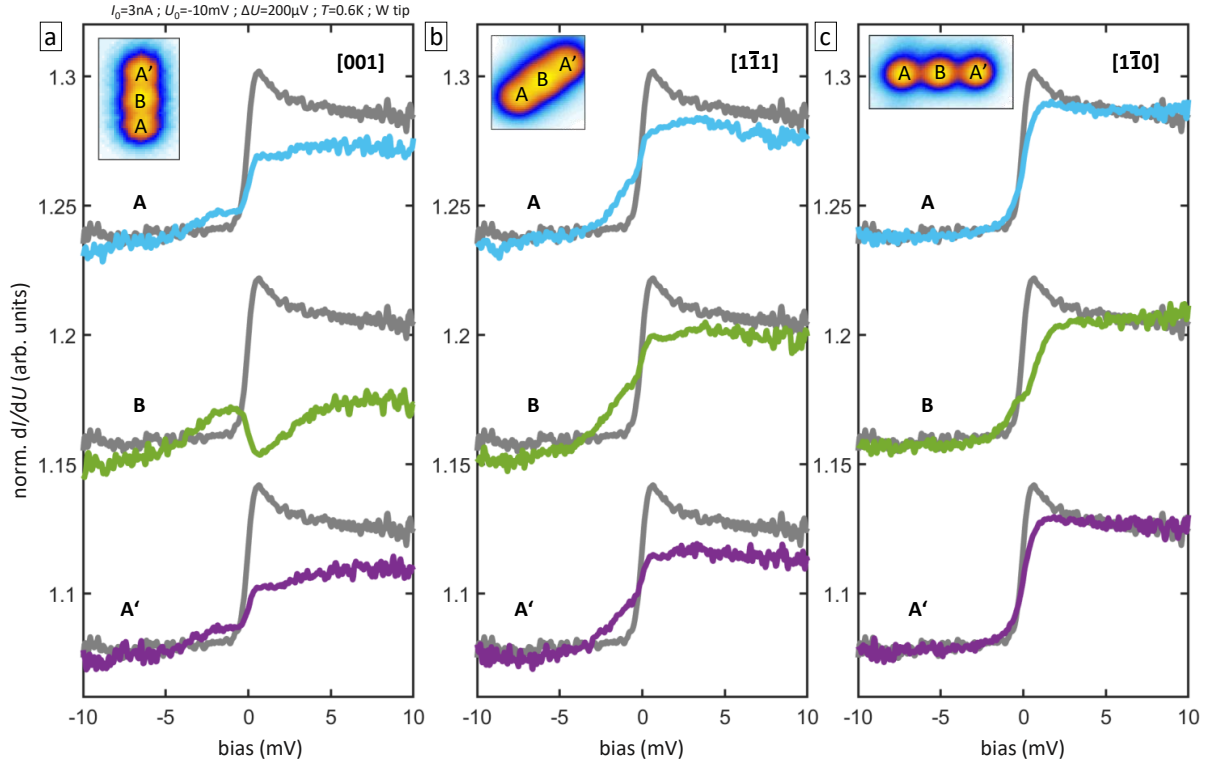
Fig. 4.19: **Trimers in the metallic regime:** Normalized dI/dU spectra on Cr trimers aligned in three different directions and with next-nearest neighbor spacing. Insets show topographic STM images with labels on each atom each corresponding to a colored curve on top of the single Cr reference (grey). (−10mV/3nA)

4.3.4 Trimers

As a final investigation of coupled Cr adatoms on metallic Nb(110), trimers were formed along the usual three directions while keeping a next-nearest neighbor spacing. That way, inevitably a net magnetic moment is maintained that can respond to the applied field for both ferro- and antiferromagnetic coupling. Due to symmetry equivalent results are expected for the atoms A and A' in figure 4.19 for each direction. For the directions of antiferromagnetic coupling, i.e. $[001]$ and $[1\bar{1}0]$, spectral shapes of atom B which has its magnetic moment pointing antiparallel to the field proves a distinct behavior from A and A'. In contrast to that, the ferromagnetically coupled $[1\bar{1}1]$ trimer keeps a similar shape for all three atoms. This further supports the conclusion that distinct spectral shapes are triggered depending whether the adatom spins are aligned parallel or antiparallel. Interestingly, spectra on atom A along $[001]$ have very similar appearance to the $[1\bar{1}1]$ dimer whereas B hosts a large dip feature leading to a reversed sharp step at zero bias which seems to follow the trend of the $[001]$ dimer. Also the $[1\bar{1}1]$ trimer continues the trend observed for the respective dimer. Lastly, even atom B in the $[1\bar{1}0]$ trimer shows an indication of an evolving dip-feature which seems typical for the antiparallel spin alignment. Overall, despite the complexity of the observed spectral shapes and

the mechanisms at play, some reproducible trends can be grasped from the results which might even enable identification of magnetic order in more sophisticated adatom structures without the need of spin-polarized STM tips. This will be put to test in chapter 4.5.

Summary

Summarizing this section about low energy spectroscopic features measured for Cr adatoms on metallic Nb(110), an intriguing wealth of phenomena can be observed by driving the system in the metallic phase. The initial sharp step-like feature on Cr adatoms can be tuned by application of different external magnetic fields or coupling atoms together with different spacing and crystallographic alignment, resulting in either AFM or FM exchange interaction. Those phenomena seem to share a common fundamental origin which is likely either inelastic tunneling via spin excitations or Kondo resonances. Here, the path explored was assuming spin excitations as the underlying mechanism having indeed some indications pointing in this direction. The magnetic field dependence and dimer spectral signatures could be grasped by a theoretical model in the unconventional spin excitation framework. Further, the observed feature persists up to a junction temperature of 15 K. Ultimately, the technical interest in understanding such spin-flip events regarding underlying excitation energies and lifetimes, for the use in e.g. spin-pumping nanoscale devices for innovative spintronics concepts, is arguably higher than in case of a Kondo feature. Finally, once more the tunability resulting from the combination of high spin moment impurities, a highly anisotropic substrate and atomic manipulation offers a well suited platform to study and identify trends in fundamental quantum mechanical processes.
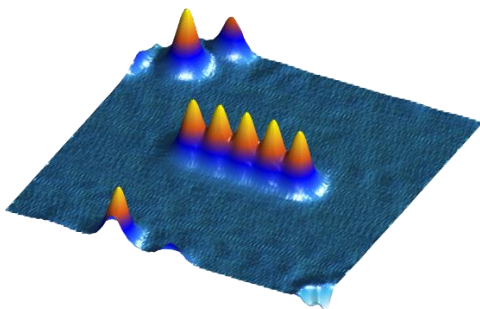
4.4 1D spin chains

Figure: STM   image   of   5   Cr adatoms forming a spin chain.

Since several seminal proposals predicted the emergence of Majorana zero modes hosted in spin chains coupled to a superconductor, it literally triggered a race between scientist groups all over the world to experimentally identify those exotic states attracting high technological interest due to their non-Abelian exchange statistics ideal for quantum computation schemes. Despite claims of their observation, control and manipulation to obtain proof of their properties remains an open challenge.

Majorana modes are predicted to appear at the ends of sufficiently long chains as particle-hole symmetric zero-energy peaks, a theory developed after the proposal of a

spinless toy model chain by Kitaev[98]. Proximitized spin wires with ferromagnetic or helical spin order with spin-orbit coupling to break time-reversal symmetry fulfill the requirements for p-wave topological superconductivity, i.e. spin-split bands inside the gap having a topologically protected crossing at the boundary.

Indeed, the efforts to create one dimensional structures of spinful impurities proximitized to a superconducting condensate has led to a lot of progress in the field and the discovery of traces from zero bias Majorana modes at the ends of such chains has been reported repeatedly[32,35,37]. However, limited flexibility of previous setups left not much room for changes of experimental parameters to rule out trivial explanations for observed phenomena and to consequently proof the finding of Majorana modes, let alone the ability to control them or to utilize their properties. In particular, most studies used exclusively close-packed chains where adatoms are nearest neighbors due to limited coupling range.

In this work, with the ability to control a huge experimental parameter space as demonstrated in the previous sections, 1D spin chains consisting of Cr adatoms on superconducting Nb(110) shall be scrutinized with a critical view on the identification of zero energy boundary modes as the exotic particles predicted by Ettore Majorana in 1937. Atomic manipulation of Cr atoms, their long ranged indirect interaction, anisotropy of the mediating substrate and YSR states close to zero enable the following control knobs to be turned: (i) chain length via the number of atoms N, (ii) inter-atomic coupling strength via (iia) crystallographic direction or (iib) distance between adatoms, (iii) magnetic order being FM or AFM as well as (iv) creating Shiba bands crossing the quantum phase transition. It will be presented systematically in the following sections how the spectroscopic signature is altered at different positions of the chains in single point spectroscopy (SPS) data, cross sectional plots showing the energy-resolved dI/dU signal over the length of the chain as well as dI/dU maps at specific energies visualizing e.g. the spatial distribution of zero modes. Data is posted on arXiv[139].

4.4.1 Building a chain atom-by-atom

As a starting point, one can have a look at the creation of an impurity chain one adatom at a time to observe the evolution of in-gap resonances to Shiba-bands step-by-step. This is presented in figure 4.20a,b for a chain along the crystallographic $[1\bar{1}3]$ direction which is depicted in panel c with an inter-atomic spacing of 0.55 nm. The YSR resonance pairs appear symmetrically around zero inside the superconducting gap for the single Cr adatom, i.e. $N = 1$. These states hybridize for $N = 2$ accompanied by an energy shift plus split, in this case leading to a crossing of the quantum phase transition since the majority of spectral weight is transferred from particle- to hole-like states. So far, the participating adatoms are in equivalent positions. This situation changes from $N = 3$. Like in the previous chapter, the trimer atoms are each in one of two distinct environments depending
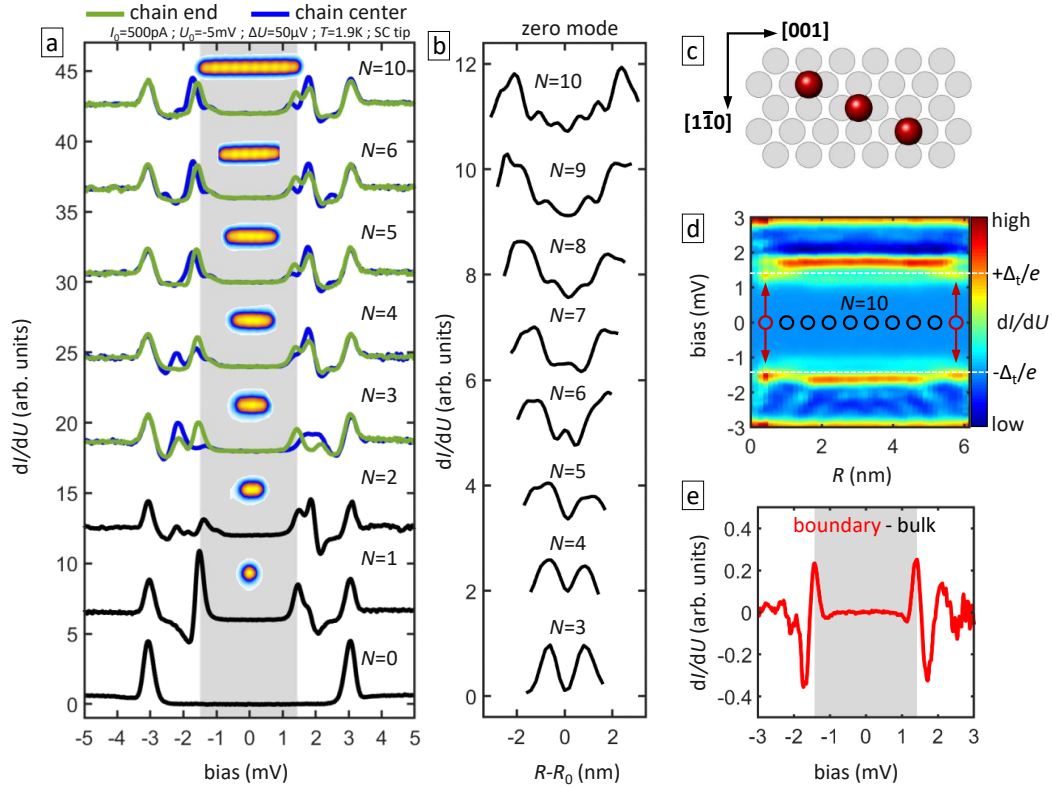
Fig. 4.20: **Chain along** $[1\bar{1}3]$ **built atom-by-atom:** **a** SPS taken on a chain with increasing number of atoms N from $N = 0$, the bare substrate, to $N = 10$ and shifted for clarity. Due to negligible differences $N = 7..9$ have been omitted. Starting from $N = 3$ chain end (green) and center (blue) are distinguished. Insets show STM topography scans of the chain. **b** dI/dU line profile along the chain at zero energy (summed up at $\pm\Delta_{\mathrm{t}}$) for $N = 2...10$. **c** Sketch of a $[1\bar{1}3]$ chain on the Nb(110) lattice. **d** Cross section along the chain showing the energy resolved dI/dU signal for $N = 10$. Atom positions are indicated by circles, arrows point at end modes located at zero energy, white dashed line marks the tip gap. **e** Difference of averaged end atoms and averaged bulk atoms of the $N = 10$ chain.

on their position in the chain being at the end or center, distinguished as green and blue spectra in figure 4.20 for $N > 2$. The central adatom has two neighbors in close distance while the end atoms have only one. Note that their spectroscopic signature is nonetheless different from the dimer where both atoms also have only one neighbor in close proximity. There are two reasons for that: the neighbor atom itself is in a distinct state due to its interaction to the third atom in the trimer, and the long range interaction between Cr adatoms is still on a comparable order of magnitude for closest and next-closest neighbors according to the results from section 4.2.5, thus the atom sees more than just the one next to it. Anyway, it is no surprise that the ends of a chain are spectroscopically different from the bulk atoms simply due to their unique environment. Astoundingly, the spectral weight on the ends shifts toward low energies while more intensity away from the Fermi level is found in the bulk. This trend already starts at $N = 3$ in the $[1\bar{1}3]$ chain where one observes indeed zero energy peaks, i.e. at $\pm\Delta_t$, at the end. This is valid quite generally also for other chains as will be shown in the following. From $N = 3$ up to $N = 6$, an evolution of both end and center spectra is observed progressively reaching an asymptotic limit where changes are below the experimental sensitivity. The fact that such a small number of adatoms can already be representative of longer chains is a direct consequence of the relatively large inter-atomic distance by not occupying nearest-neighbor positions. The larger the role of purely indirect interaction the more it is justified to still speak of individual atoms in the chain whose direct orbital overlap stays small while their YSR states strongly hybridize. Using this individual atom picture, on the one hand, when the interaction between end and center becomes sufficiently small, increasing the number of atoms will simply enlarge the bulk. This seems the case by looking at the intensity at zero energy depicted for $N = 3...10$ in figure 4.20b that is consistently enhanced at the ends with approximately constant spatial extension while the weakly oscillating signal in the bulk grows bigger. On the other hand, periodicity and translational symmetry in the chains results in the emergence of electronic bands. Longer chains host an increasing number of space frequencies showing dispersion.

Figure 4.20d presents the result of 45 SPS measurements along a straight line over the chain where the x axis measures the distance R from the first SPS position, the y axis is the bias and dI/dU signal is shown as a colorscale, in a so-called cross sectional spectroscopy. It nicely visualizes the end modes located at the last atoms of the chain energetically at zero ($\pm\Delta_t$ indicated by white dashed lines) marked by red arrows. Moreover, an oscillating signal reminding of concentric waves in this hybrid energy-space-mapping can be seen especially well between -3 and $-1.5\,\mathrm{mV}$ which is a manifestation of the dispersing Shiba band and can be transformed to momentum space which will be shown for longer chains in a later paragraph.

Finally, panel e highlights the presence of zero bias end modes that show indeed almost perfectly symmetrical intensity around the Fermi level after subtracting the bulk back-

ground signal. Considering the promising starting conditions, i.e. an indirectly coupled, diluted spin chain hosting deep Shiba states, this result would be compatible with the emergence of Majorana zero modes. However, there is at least one circumstance strongly opposing this interpretation. A pair of Majoranas not sufficiently far away from each other is expected to hybridize thereby shifting away from zero. The observation of end modes already at $N = 3$ with a chain length of merely 1.1 nm that essentially show no evolution with N clearly promotes a more trivial approach. A tight-binding model providing such an explanation shall be briefly described later. Before that, a systematic variation of chain parameters shall elucidate the role of directions, inter-atomic spacing and magnetic order for spin chains.

4.4.2 Chains along different angles

Learning that one dimensional assemblies of just a few indirectly coupled magnetic impurities are representative of a spin chain, an investigation of short 5 adatom chains is expected to suffice for a systematic study. Like previously, together with the angle inevitably also the adatom distance changes so that only a combined effect of directionality due to Fermi surface anisotropy and distance dependence can be observed.

The results are presented in figure 4.21. The 8×8 nm topography scans demonstrate a very clean environment around the chain free from surface defects, contaminants and other adatoms. Cross sectional spectroscopy plots in figure 4.21b nicely point out the characteristic differences and similarities between the chains. Spectral weight is accumulated more on the particle side for chains along $[001]$, $[1\bar{1}5]$ and $[1\bar{1}1]$, on the hole side for $[3\bar{3}0]$ and $[1\bar{1}0]$. This observation is in agreement with trends already observed in section 4.2.4 for Cr dimers along corresponding directions. Since the spectral weight distribution is a direct expression of the impurity-substrate coupling in diluted chains it means that the alignment of coupled impurities to the substrate lattice sets the tone for their interaction with the superconducting condensate rather than the number of involved impurities nor their magnetic order being AFM, FM, AFM for $[001]$, $[1\bar{1}1]$, $[1\bar{1}0]$, respectively, highlighting again the role of strong Fermi surface anisotropy. A trend that all of the measured chains have in common is the redistribution of spectral weight between dispersing bulk states at higher energies and end states of high intensity at lower energies. Note that low-energy end modes are not necessarily symmetric around zero as clearly visible e.g. for $[001]$. However, there is indeed always a non-vanishing enhanced zero-energy intensity at the ends of the chain as compared to the bulk. This is visualized in panel c where dI/dU maps show the combined dI/dU signals at $\pm\Delta_t$ which is consistently higher at the ends throughout all the chains. It might be interesting to remark that the additional second dimension in space in dI/dU maps reveals the shape of the electronic states which is in general not isotropic but rather elliptical expressing the alignment to the anisotropic

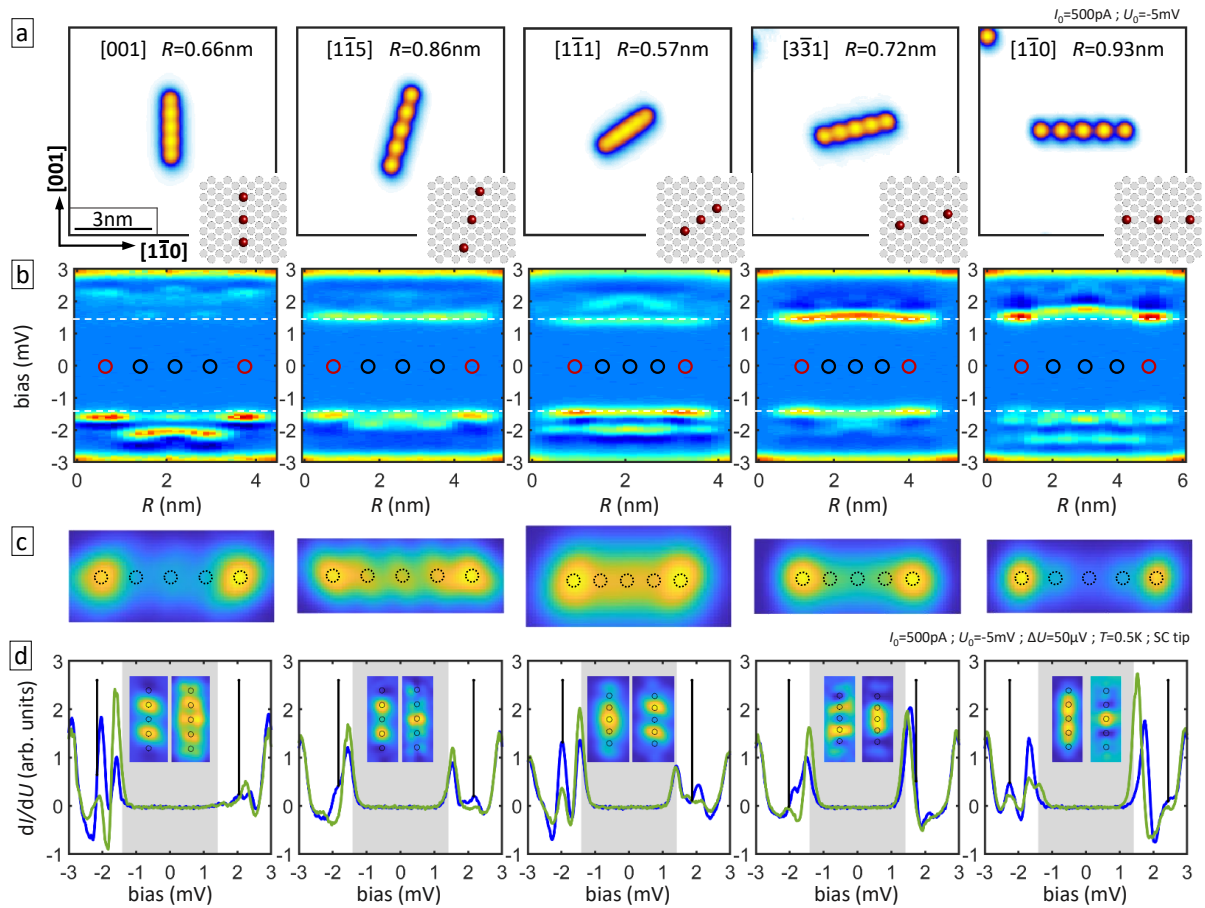**Fig.** 4.21: **Chains consisting of 5 atoms along different crystallographic directions:** **a** STM topography of the chains with insets sketching their lattice alignment. **b** STS cross sections. **c** Zero energy maps (averaged signal at $\pm\Delta_t$). **d** SPS at chain end (green) and center (blue). Insets show dI/dU maps at energies indicated by black lines, left and right panels at negative and positive energy, respectively.
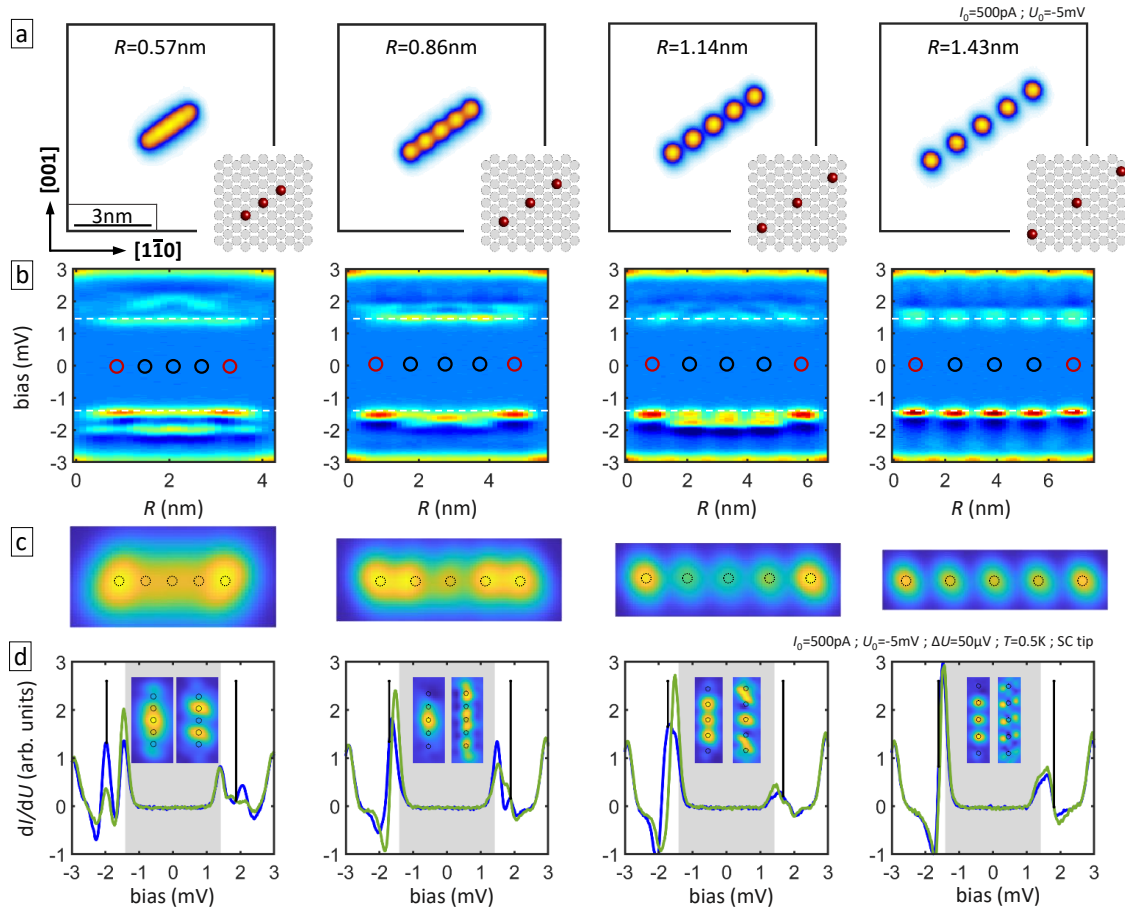
Fig. 4.22: **Chains consisting of 5 atoms along $[1\bar{1}1]$ with different inter-atom spacing: a** STM topography of the chains with insets sketching their lattice positions. **b** STS cross sections. **c** Zero energy maps (averaged signal at $\pm\Delta_t$). **d** SPS at chain end (green) and center (blue). Insets show dI/dU maps at energies indicated by black lines, left and right panels at negative and positive energy, respectively.

lattice, particularly clear for $[1\bar{1}5]$ and $[1\bar{1}1]$. Finally, panel d contrasts chain end (green) and center (blue) in SPS plots where the exact energetic position of the end mode peak with respect to zero (edge of grey tip gap area) can be seen. For $[001]$, $[1\bar{1}5]$ and $[1\bar{1}1]$ it seems like constant-energy peaks that are present along the whole chain simply gain intensity at the end while for $[3\bar{3}0]$ and $[1\bar{1}0]$ a clear shift of the peak towards zero occurs. The insets show dI/dU maps of some bulk states with symmetric and periodic character resembling a one dimensional particle-in-a-box scenario.

4.4.3 Varying inter-atom distance

The next experiment was done in order to shed light on the role of hopping amplitude exclusively controlled by inter-atomic distance for a fixed direction, i.e. $[1\bar{1}1]$ which has the smallest discrete step size provided by the (110) surface lattice.

Figure 4.22 uses the same style like the previous one. As one would expect, the larger the distance the less hybridization occurs and the more individual adatoms resemble an isolated Cr impurity. However, up to 1.14 nm separation dispersing bands especially in the hole-like states appear and even for the largest measured separation of 1.43 nm a faint shift towards lower energies at the end atoms is evident leading to slightly enhanced intensity in zero bias dI/dU maps at the chain ends (figure 4.22c). dI/dU maps showing the spatial distribution of higher energy states also reflect the evolution from strongly hybridized states related to the chain as a whole for densely packed adatoms to separate atomic orbital-like shapes for dilute chains. Although the results for increasing distance are not unexpected, they demonstrate the emergence of low energy chain end states up to remarkably long inter-atomic spacing.

4.4.4 Longer chains

As commonly assumed in the literature, stable Majorana zero modes only manifest in sufficiently long spin chains. To create very long chains becomes progressively more challenging in the experiment due to remaining surface defects and contaminants. Despite the strong influence of closeby oxygen on Cr adatom spectra observed in figure 4.14, Majorana modes should be topologically protected and prove robust against perturbations. However, experimentally the manipulation of adatoms very close to oxygen bears high risk of irreversible tip changes which would sabotage a systematic measurement sequence. Therefore usually chains no longer than 15 to 20 atoms were built. Their diluted character still results in a total length of 16 nm.

Figure 4.23 shows two examples of longer chains along $[001]$ and $[1\bar{1}3]$. The first observation worth mentioning is that in none of the chains there appears a significant difference between chains consisting of an even or odd number of atoms. It can be seen already from the results in figure 4.20 and also in figure 4.23, e.g. panels a and b for $N = 11$ and $N = 12$. Due to symmetry and periodicity of the higher-energy modes the center of the chain alternates between hill and valley with odd and even number, however, the chain ends remain unchanged. Anyway, the spatial extension as well as the energy of end modes show, within the experimental resolution, no signs of evolution with increasing number of atoms, neither for the chains depicted in figure 4.23, i.e. $[001]$ between $N = 11$ and $N = 20$ and $[1\bar{1}3]$ between $N = 5$ and $N = 15$, nor longer chains along other directions. Changing the focus to the bulk of the chains, it becomes clear how progressively more space frequencies fit inside the chain with increasing length, so that a Fourier transformation of the real space axis to momentum space for the longest chains reveals dispersing bands. Examples are marked with red arrows in figure 4.23d and h. In summary, exploring a wide parameter space in the experiment, the observed trends appear very persistent: the spectral weight distribution in dI/dU measurements of a Cr chain of arbitrary length N is
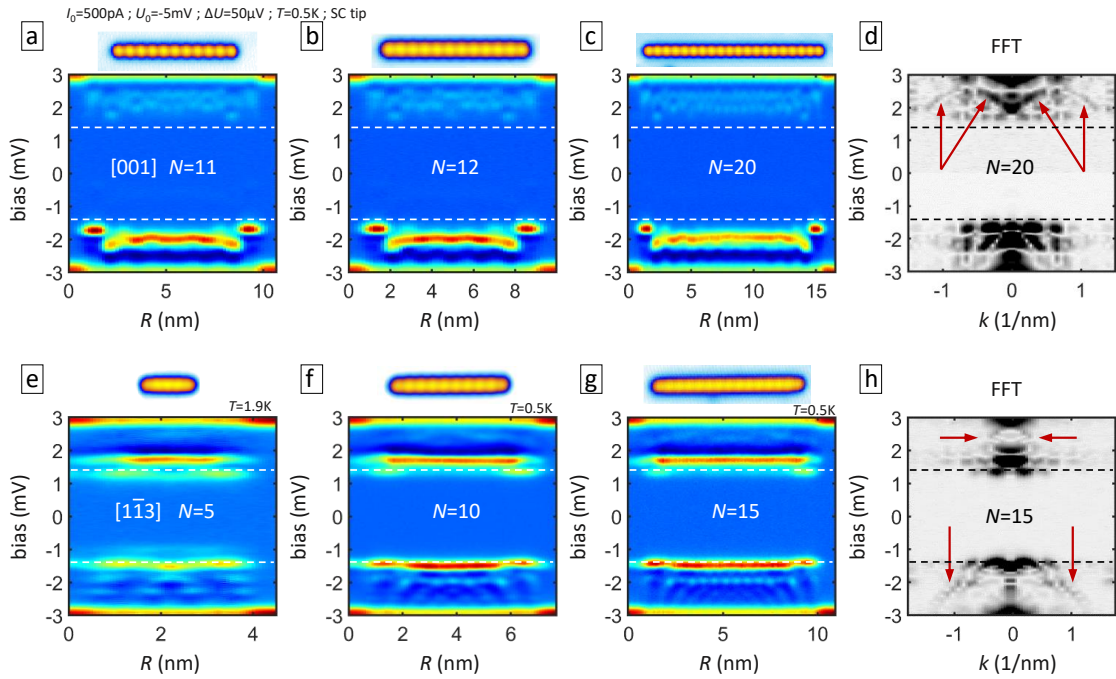
Fig. 4.23: **Chain length evolution: a-c** Cross sectional dI/dU line plots for $N = 11, 12$ and 20 along $[001]$, **e-g** for $N = 5, 10$ and 15 along $[1\bar{1}3]$. **d,h** respective plots after a Fourier transformation of the real space axis to momentum space. Red arrows point to emerging electronic bands.

similar to a Cr dimer $N = 2$ along the same crystallographic direction, end states appear starting from $N = 3$ and are shifted towards the Fermi level compared to the chain bulk even for weak and purely indirect coupling, states in the bulk form dispersing bands visible in momentum space for sufficiently long chains. In the following, less homogeneous chains will be investigated to test the robustness of those trends.

4.4.5 Chain interruption

The next experiment has two goals: to check whether the order matters in which the chain is built, and to see how a vacancy defect acts on the chain's spectroscopic features. First, a complete chain of $N = 15$ atoms along $[1\bar{1}0]$ was measured with cross sectional spectroscopy as shown in figure 4.24a. Then one adatom was removed from the center of the chain leaving a vacancy, and the measurement was repeated. As seen in panel b two low-energy states around the defect appear very similar to the end states but with lower intensity. This would not be incompatible with a topological state since the defect creates another boundary. However, one could also see it as two $N = 7$ chains having two end states each. Still, the coupling between the two closeby ends cannot be neglected so that their end states appear slightly different, i.e. the reduced intensity with respect to the original ends is indicative of this interaction. Since $[1\bar{1}0]$ is the direction with the fastest decay of coupling strength, removing another atom from the closeby end of each chain,
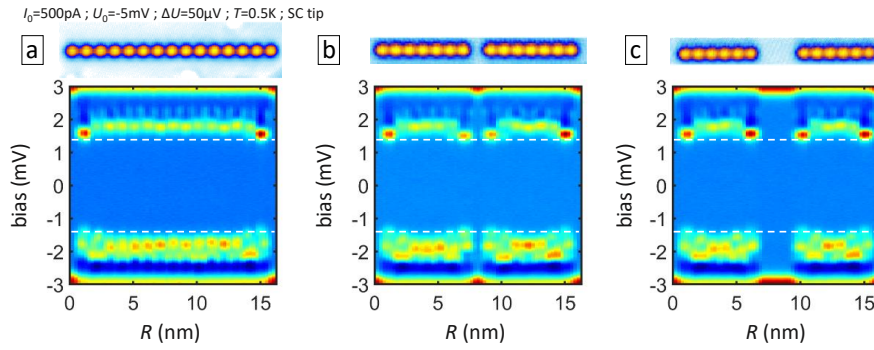
Fig. 4.24: **Chain interruption:** Cross sectional spectroscopy of **a** a $N = 15$ chain along $[1\bar{1}0]$, **b** the very same chain after removing the central atom and **c** after removing the 3 central atoms.

as done in panel c, sufficiently decouples them to leave effectively two $N = 6$ atom chains remaining with approximately unperturbed spectral signature. This means that different building order finally lead to the same resulting chain with low-energy end modes and electronic structure characteristic for their direction and spacing.

4.4.6 Dimerized chains

To gain another possibility to controllably create different boundaries and well-defined defects in adatom chains with the goal of understanding their effect on the overall chain properties, dimerized chains have been built inspired by the so called Su-Schrieffer-Heeger model (SSH)[171,172], which has never been explored previously on magnetic impurity chains on a superconductor.

The SSH model describes fermions on a one dimensional chain with staggered hopping amplitudes v within two-atom unit cells and w between neighboring unit cells. The spin of the electrons is omitted which makes a comparison to a real example difficult and should be done with care, however, the hopping premise is nicely caught by the indirectly coupled locally bound in-gap states. For the Cr chain shown in figure 4.25a the distance along the crystallographic $[1\bar{1}1]$ direction is varied between 0.57 nm and 0.86 nm according to next- and next-next-nearest neighbor separation, respectively. The scenario $v > w$ is represented by unit cells of type α since the short distance unit cell provides enhanced hopping, which results in a topologically trivial regime according to the model. Looking at the results in figure 4.25b clearly low-energy end modes are visible localized over the last dimer unit cell. The cross sectional spectroscopy plot shows an alternating peak energy in the bulk especially clear for the high-intensity peaks at negative energies shifting up and down representing the staggered hopping sequence with a peak around −1.6 mV for high hopping and one around −2.1 mV for low hopping. Just before the end units an up-shift of the low-hopping state can be observed as a transition to the end state. Next, a single defect is introduced in panel c as a domain wall by repeating the same distance
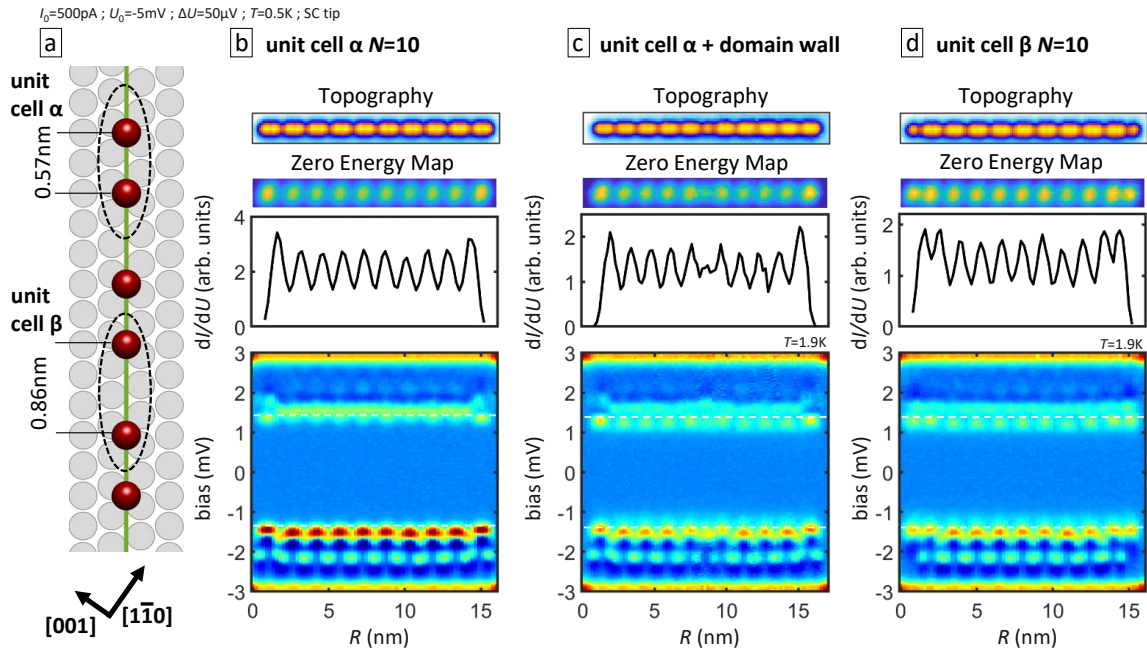
Fig. 4.25: **Dimerized chains: a** Sketch of the Nb(110) lattice with a Cr adatom chain along $[1\bar{1}1]$ having alternate spacing, i.e. a two adatom unit cell being a dimer with short (α) or longer (β) spacing. **b-d** STM topography, dI/dU maps at $E = 0$ (averaged $\pm\Delta_t$) and cross sectional spectroscopy data for $N = 10$ unit cells of type **a** α, **b** α with a single adatom domain wall and **c** β.

twice in the middle of the chain, ending up with a total of 21 instead of the previous 20 atoms. Like before, as defects represent a boundary, additional zero energy modes should appear in case of a topologically non-trivial state. And once more the experiment gives a rather vague answer with an enhancement at zero energy which is just at the limit of experimental sensitivity, thus making an interpretation difficult considering the complexity of this setup. Finally, the topologically non-trivial case $v < w$ within the SSH model corresponds to a chain of unit cell type β shown in panel d. The bulk looks identical to the previous cases, however, the end units feature a less pronounced accumulation of spectral weight at zero. This could be related to the larger intra unit cell atomic distance since the end mode evolves the whole last unit cells consisting of two atoms which leads to higher delocalization and therefore lower intensity. As already mentioned, the validity to compare this setup to the SSH model is very limited. Therefore, the results shall not be used to signal a topologically trivial or non-trivial state, which does not seem feasible, rather they can demonstrate how challenging the identification of boundary modes as topological modes is and that a lot of care is necessary, demanding experiments beyond the detection of a zero-bias feature.
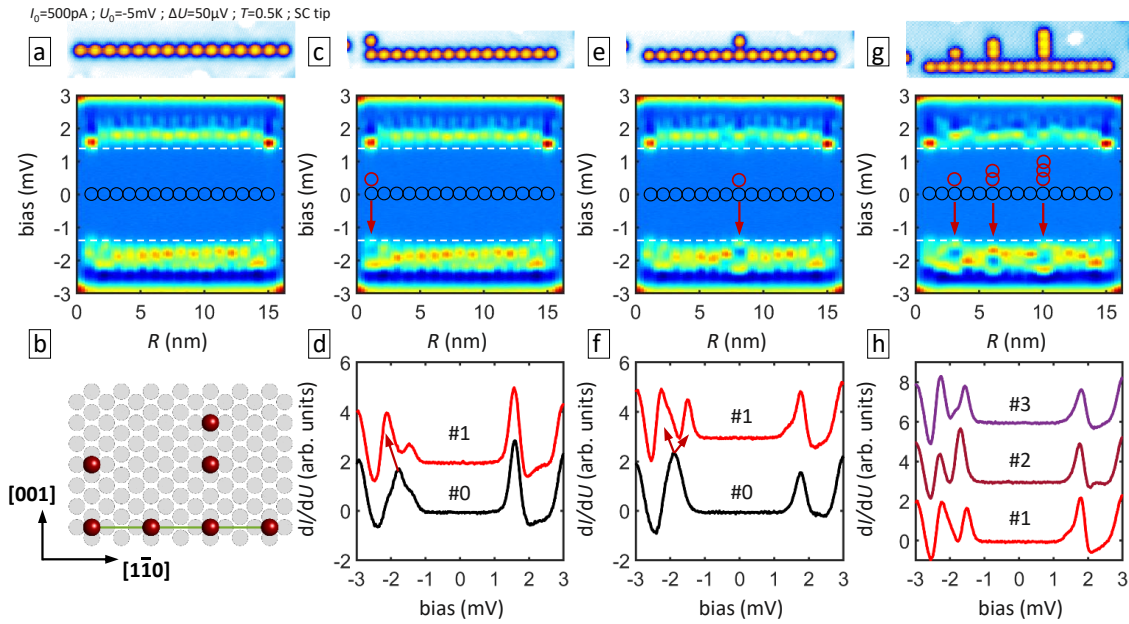
Fig. 4.26: **Chain towards 2D: a** Cross sectional spectroscopy of a $[1\bar{1}0]$ Cr chain with $N = 15$. **b** Schematical illustration of how additional adatoms have been placed. The very same chain like in **a** with an additional Cr adatom in 0.99 nm distance in [001] direction from **c,d** the first atom, **e,f** the central atom of the chain, creating a perturbation. In **g,h** 1, 2 and 3 adatoms have been placed at positions 3, 6 and 10 of the chain, respectively. Red arrows point to effects of perturbations visible in the plots. SPS curves **d,f** show the signal on top of the respective chain atom before (black) and after (red) placing the perturbation. **h** compares SPS on the three perturbed positions.

4.4.7 Towards 2D

With the final experiment concerning 1D chains, a first step towards the two dimensional assemblies shall be done. To test the response to influences approaching from the side of the chain, additional adatoms have been placed orthogonal, i.e. along [001], to a 15 atom chain along $[1\bar{1}0]$.

This setup is shown in figure 4.26. Note that all spectra shown are exclusively taken on the $[1\bar{1}0]$ chain and not on additional adatoms. As another remark, this particular $[1\bar{1}0]$ chain is an example of a slight spacial asymmetry that is observed in some of the investigated chains, despite the ideal scenario being a perfect mirror symmetry about an orthogonal line through the center of the chain. As seen from figure 4.26a symmetry is broken especially in the negative energy states. The reason in this case could quite clearly be closeby oxygen or other adatoms coupling to the chain states. Even in very contaminant-free areas subsurface defects not caught in STM scans can be responsible for such imperfect chain symmetry. However, for this experiment it shall not obscure the desired information.

The general concept of how controlled perturbations are placed is illustrated in panel b. Additional Cr adatoms are moved to positions in 0.99 nm distance, according to 3

lattice constants, along the [001] direction, from an adatom inside the chain. This is a very similar distance compared to the intra-chain separation of $0.93\,\text{nm}$, still, the Fermi surface anisotropy leads to different coupling effects. If more than one additional atom is placed they are separated by $0.66\,\text{nm}$. The first perturbation that should controllably act on the $[1\bar{1}0]$ chain is a single Cr adatom at the first atom position. Indicated by the red arrow in panel c, only very locally limited to one atom position a significant change can be detected. Further it is only seen in the occupied states and does not have any influence on the end mode peak as can be seen clearly from panel d that shows the spectra on the first chain atom before and after placing the additional one. It leads to a shift of spectral weight away from the Fermi level. In the next case shown in panels e and f, the single perturbation is moved to the center of the chain. Like before the strongest effect is observed in the occupied states and there it is spatially limited to one atom. A previously broad peak seems to split into two clearly separated peaks. However, now an effect can be seen also on the closest neighbor atoms where smaller changes in the unoccupied states are observed likely linked to d_{xy} hybridization. Finally, three different perturbations have been placed at once. One single Cr adatom, a [001] close distance dimer and a trimer in position 3, 6 and 10 of the chain. Looking carefully at the cross sectional STS their positions can be clearly inferred from the data since they all induce a strong splitting of spectral weight in the negative energies. There is no large difference depending on the number of stacked adatoms creating the perturbation. At least between one (#1) and two (#2) the peak intensities and energy positions are slightly distinct while the trimer (#3) results in an effect very similar to a single atom. Remarkably, even having all these additional adatoms closeby the end states characterized by a sharp and intense peak seem not affected at all. These results highlight the individual atom character that remains for each constituent of the chain given by the interaction being indirect and a relatively weak hopping between them. Therefore significantly changing the quasiparticle spectrum of one adatom leaves the rest of the chain mostly unaffected. Especially the end states appear very robust. Moreover it is demonstrated how the superposition of couplings along different crystallographic directions can create new possible variations of the in-gap structure opening the door to two dimensional custom built nanostructures bearing the hope that with engineering ingenuity exciting new physics can be found.

4.4.8 Results of a simple tight-binding model

To scrutinize the origin of the observed end modes, a minimal tight-binding model has been employed to simulate a magnetic impurity chain coupled to a superconductor. This model explicitly does not include spin orbit coupling which makes it impossible for the system to enter a topological regime. Hence, all results are of trivial origin. The impurity-substrate coupling parameter is taken as $J = J_{\text{crit}}$ to model the Cr YSR state close to
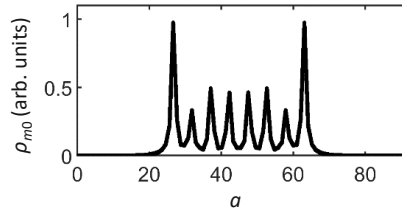
Fig. 4.27: **Result of a minimal tight-binding model:** Calculated density of states at zero energy along a cross section of a magnetic impurity chain embedded in a superconductor modeled on an area of 50×92 lattice constants a.

zero energy. Other model parameters have been varied. A broadening parameter was introduced to account for experimentally limited resolution.

Figure 4.27 shows the result of the calculated density of states at zero energy for a chain of 8 indirectly coupled, i.e. spaced by 5 lattice constants, magnetic impurities on a superconductor for specific model parameters. Quite clearly, an accumulation of states is produced at the chain ends matching the experimental observation. Further, particularly for indirectly coupled chains the outcome is largely independent of the chain length and is similar also for dimerized chains. Even without the claim to reproduce the real situation in the experiment, this is an important result giving a simple message: The phenomenon of zero bias end modes can be described by topologically trivial mechanisms.

Chains summary

Recalling the experiments with bottom-up crafted Cr adatom chains on clean Nb(110), a chain was thoroughly studied adding one atom at a time, crystallographic direction and inter-atomic distance dependence was investigated on short chains with 5 adatoms and chains up to 20 adatoms have been measured as well. It was further tested how chains react to vacancies artificially introduced in a complete structure, to enlarged unit cells by dimerization and to controlled perturbations by other closeby Cr adatoms. It was found that strong low energy end modes emerge for each measured chain which can be perfectly located at zero energy with particle-hole symmetry within experimental resolution for certain chain configurations. These end modes are robust against perturbations and occur, although weaker, also at defects that create additional boundaries. This is an observation in agreement with theoretical predictions of a topological superconductor hosting Majorana zero modes which is a major aim of research on these systems. Therefore it is especially important, however, to keep a critical mindset and to consider all possible origins of experimental observations. The appearance of zero bias end modes for chains as short as 3 atoms in a row is the first observations clearly indicating a trivial phenomenon since two Majoranas are expected to hybridize on short length scales. The fact that the end modes appear for all measured configurations spanning a large parameter space is another indicator for less exotic physics. And finally, a model that explicitly excludes

topological phases can reproduce the experimental observations which ultimately leads to unresolved ambiguity in the measurements. It is therefore concluded that the origin of low energy end modes is trivial in the majority of cases and that under these circumstances the discovery of potentially emerging topological boundary modes would be very challenging. The presented study on magnetic impurity chains is of unprecedented scale in parameter space owing to a system most tunable. Therefore the results, by questioning the criteria that determine how Majorana modes are searched for[120], pose an invaluable input for the field.

4.5 Spin polarized measurements

The importance of strength and sign of magnetic exchange couplings for the interpretation of the previously shown data was pointed out both in the superconducting and metallic phase. So far, the discussion referred to the obtained theory parameters summarized in figure 4.15 for Cr dimers, however, as already mentioned those calculations have been partly checked by spin-polarized STM. Results will be shown in this chapter and highlight both the remarkable predictive power of *ab initio* calculations as well as the necessity of experimental verification.

In order to do so, an STM tip carrying a magnetic moment can be employed to achieve atomically resolved spin contrast through a spin-polarized tunneling current. Two different ways to obtain such a tip will be shown here: using a tip made entirely out of Cr which assumes an antiferromagnetic ground state below the Néel temperature of 308 K, and an *in-situ* tip functionalization with only few magnetic atoms. The latter is attempted in two different ways: using a superconducting tip to set up spin polarized YSR spectroscopy like recently demonstrated for the first time[28], and with a normal metallic tip. One thing all techniques have in common is a usually very frail working condition where a loss of spin contrast if often just a matter of time, in particular when atomic manipulation processes are involved that easily modulate a slightly unstable tip apex. It requires a lot of attempts and time so that up to present date results could be obtained for four chain directions only. Therefore, at the end of this chapter an alternative way of distinguishing FM and AFM chains with a common tungsten tip will be explored that was proposed in section 4.3 about spin excitations. Measurements have been taken on chains consisting of an odd number of Cr adatoms to ensure a magnetic structure that can be fixed with an external field in case of AFM coupling. Data has been published[139,149].

4.5.1 Cr bulk tip

Cr bulk tips from etched high purity Cr bars are the standard way of doing spin polarized STM in the used microscope system. Their spin contrast performance is characterized on
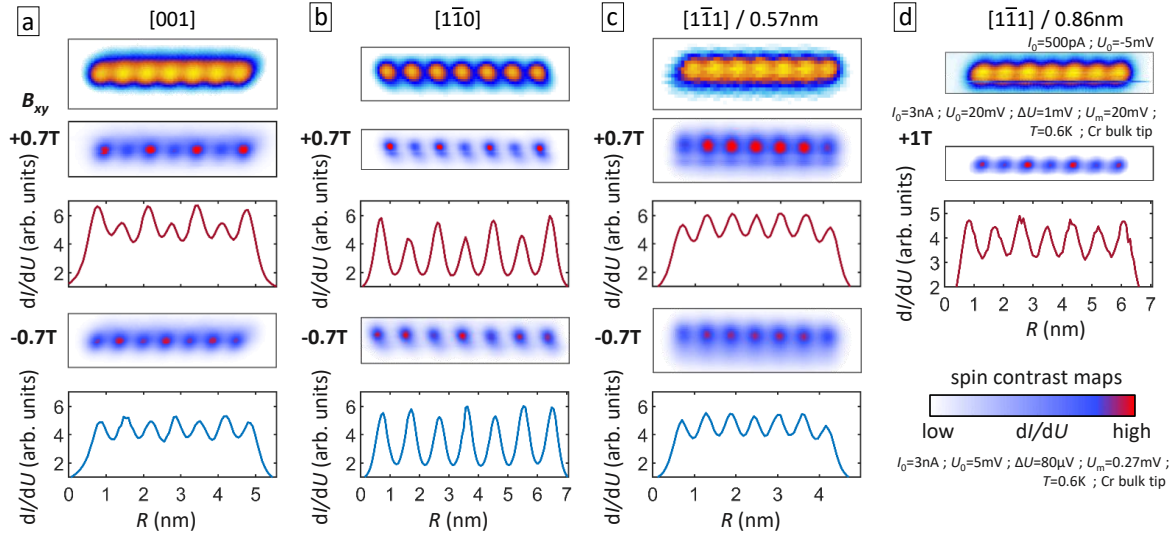
Fig. 4.28: **Sensing magnetic order with a Cr bulk tip:** For each of the 4 shown directions: STM topography image, dI/dU map with given value of external in-plane magnetic field and corresponding extracted line profile, dI/dU map and profile for opposite field direction showing reverted contrast. For direction **d** a different microtip was used which did not provide reverted contrast.

an iron double layer on tungsten as shown in section 3.2.2 before the Nb(110) single crystal is inserted into the microscope and Cr adatoms are deposited. Atomic manipulation is employed to create spin chains that are object to the spin polarized measurement. The initial tip preparation serves the purpose to start off in the best possible situation increasing the likelihood of a successful *in-situ* repreparation of a spin sensitive tip after the chain assembly. To do that, the tip apex was modulated by bias voltage pulses between −1 and −3 mV or Cr atoms from the surface were approached with the tip until they jumped to the apex where their magnetic moment is fixed by the antiferromagnetic exchange to the bulk. Thus, ideally the Cr tip has a stable direction of magnetic moment that holds against external fields applied along different vectors.

The results featuring spin contrast are shown in figure 4.28. For the used tip it was only seen for specific in-plane orientations of the externally applied field. The weak magnetic anisotropy of Cr moments on the surface likely align with the field while keeping their internal magnetic structure[3]. For the presented chains along [001] , [1$\bar{1}$0] and [1$\bar{1}$1] the very same tip configuration could be maintained to measure with constant spin contrast. For each direction figure 4.28a-c shows, from top to bottom, a topography scan, a dI/dU map acquired with open feedback to avoid set point effects while an in plane field of 0.7 T was applied, a corresponding cross sectional profile taken from the scan above, another dI/dU map and line profile for the opposite magnetic field direction. The chains [001] and [1$\bar{1}$0] quite clearly exhibit alternating contrast indicative of AFM coupling for +0.7 T with

---

[3]This conclusion is drawn from the observation of spin contrast in presence of an external out of plane field with a different tip which is shown later.

more intensity on 4 out of 7 atoms which means that the tip magnetization is aligned with the field and consequently the residual moment of the chain. The $[1\bar{1}1]$ chain signal does not alternate suggesting FM order. Only at the end atoms a weaker signal is detected which is very likely not related to magnetism but to the distinct density of states at the chain ends. In the next step, the field is reverted to -0.7 T in antiparallel direction. This is crucial to distinguish the observed signal from non-magnetic effects. Indeed, the AFM chains $[001]$ and $[1\bar{1}0]$ both demonstrate reverted contrast with the three atoms in even positions appearing with higher intensity. Since the switching of contrast was triggered only by magnetic field reversion, the effect is clearly of magnetic origin. However, in this direction the contrast is significantly weaker which suggests an effective rotation of the tip magnetization under the applied field. Further, a field increase to -1 T overcame the anisotropy at the tip apex and aligned its moment which then leads qualitatively to the same picture detected for +0.7 T. The $[1\bar{1}1]$ chain confirms an FM order by showing an overall reduced intensity for the reverted field. Finally, figure 4.28d depicts the case of a chain along $[1\bar{1}1]$ with one step larger distance between the atoms. The measurement was taken with the same macrotip, however, after it experienced a microtip change which lead to a loss of the previously stable magnetization direction. Therefore a contrast reversion could not be obtained in this case. Nevertheless, the observed alternating contrast strongly indicates AFM order along the chain. While $[001]$ (AFM), $[1\bar{1}0]$ (AFM) and $[1\bar{1}1]$ 0.57 nm (FM) quite remarkably confirm the theoretical prediction, $[1\bar{1}1]$ 0.86 nm exhibits AFM order contrary to the theory result which suggested to weakly favor an FM structure. Overall, measurements with the Cr bulk tip eventually yielded the desired information, however, the unpredictability concerning the timescale and success of the experiment makes it worthwhile to investigate alternative routes to spin polarized tunneling. In particular, the availability of well-isolated single magnetic surface adsorbates in the present experiment promotes the use of controlled tip functionalization by picking up single atoms to the tip apex. Results of two distinct approaches using this concept will be described in the following.

4.5.2 Fe functionalized SC tip

The idea of functionalizing the tip probe *in-situ* is not new to STM. It was used in this work widely to pick up a superconducting Nb cluster. However, the intriguing concept to induce YSR states into the superconducting tip gap by picking up single magnetic adsorbates is more recent[28,30]. It is based on the complete spin polarization of particle and hole part of a YSR state (see section 2.1.2).

Here, it was done by adding two Fe adatoms to the apex of a tip which was previously functionalized by a superconducting Nb cluster. To do so, the tip is positioned on top of the adatom and approached in open feedback until a tunneling current of approximately
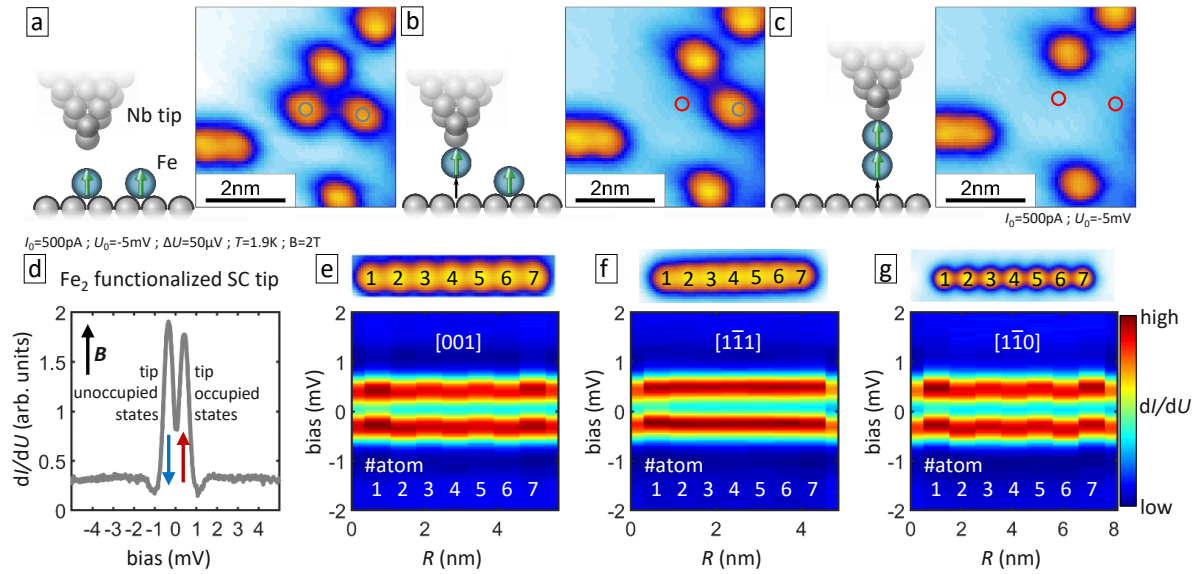
Fig. 4.29: **Fe functionalized Nb tip: a-c** STM images of the same area with corresponding sketches showing the process of subsequently picking up two Fe adatoms with a superconducting STM tip. Grey (red) circles mark the (picked) Fe adatoms. **d** STS taken on the clean substrate representing the tip density of states with a pair of YSR states. An out of plane magnetic field of 2 T was applied to suppress superconductivity in the Nb substrate, not in the tip Nb cluster. **e-f** Topography scans and cross sectional STS on 7 atom Cr chains along three different crystallographic directions.

120 nA at 5 mV is reached. Voltage pulses of 2 V are then applied until a change of tunneling current is observed which indicates a successful transfer to the tip. Like shown in figure 4.29a-c, the atoms are controllably picked up one after the other as seen from subsequent topography scans over the very same sample area. Fe is chosen because it tends to couple ferromagnetically with rather strong out of plane anisotropy and the Fe_2 dimer induces intense YSR states well inside the gap without overlap at the Fermi level (see figure 4.7). When the desired spectral signature is obtained upon measuring on the bare substrate, the tip functionalization was successful. Under an external magnetic field (here 2 T out of plane), used to stabilize the chain magnetization, the dI/dU signal shown in figure 4.29d is detected. While fields above the critical field of 0.5 T fully suppress superconductivity in the Nb single crystal, a much larger field is needed for the Nb cluster at the tip depending on its shape. Therefore the tip gap ($\Delta \approx 1.45$meV) with a pair of YSR peaks persists. Since this dI/dU spectrum represents the tip density of states, occupied and unoccupied states are now flipped compared to the sample DOS, i.e. found at positive and negative bias voltage, respectively. YSR pairs are intrinsically spin polarized so that the resonance at positive bias should only allow tunneling of electrons with spin aligned to the applied field resulting in varying intensities with opposite behavior for particle and hole peak depending on the sample magnetization. Surprisingly, this is not observed for Cr adatom chains along [001], [1$\bar{1}$0] and [1$\bar{1}$1]. Especially the former two that are already known

to feature AFM coupling do not produce the expected signal contrast. Instead, a small alternating shift in energy is observed for both peaks in the same direction. A constant shift is observed for the [1$\bar{1}$1] chain consistent with the previously determined FM order. This result was obtained independently from the orientation and strength of the applied magnetic field. In conclusion, the observation of shifting peaks seems to be reminiscent of the real magnetic structure being either FM or AFM, however, it indicates a very low spin polarization of the tunneling electrons contrary to the expectation, ultimately too weak to determine the state of unknown structures.

4.5.3 Cr functionalized metallic tip

The second tip configuration that produced an especially clear spin polarized dI/dU signal was obtained by picking up a single Cr adatom to the apex of a normal metallic tungsten tip characterized on Ag(111). To pick up a Cr adatom voltage pulses turned out to be less useful and did not succeed in the majority of cases. Rather, approaching the tip in small steps until an abrupt small jump in the tunneling current occurred, lead to the desired pick-up event[4]. However, the success rate of this method seemed significantly lower than for the previously described Fe pick-up. Unwanted outcomes like larger clusters dropping from the tip to the surface or picked from the surface to the tip happened in some attempts. The latter event can become problematic since picked up Nb clusters eventually establish superconductivity in the tip which is situationally unwanted because it depopulates energies around the Fermi level that can potentially provide spin polarization, plus, it is often irreversible without exchanging the whole STM tip[5]. Moreover, depending on the specific microtip the resulting spectroscopic behavior can greatly differ even after a successful pick-up process.

Figure 4.30a schematically illustrates a pick-up event of a Cr adatom and panel b the resulting tip density of states. All curves were acquired under an external magnetic field of > 1T and with the tip positioned over the bare substrate so that the difference between the grey line and colored lines describes only a change in the tip where after functionalization two peaks at approximately ±1mV appeared in the spectra. Further, their response to an increased magnetic field, i.e. both peaks shifting away from the Fermi level in opposite directions, indicate their magnetic character and opposite spin polarization. In agreement with both theory and previous data, antiferromagnetic order is concluded from measurements along 7 atom chains along [001] and [1$\bar{1}$0] , ferromagnetic order for the short distance chain along [1$\bar{1}$1] . dI/dU maps, dI/dU cross sections and SPS on oppositely magnetized chain atoms are shown in figure 4.30c-g for the three chains. Here, the external magnetic field of 2 T was applied out of plane. Together with

---

[4]Occasionally a Cr adatom was also picked up unintentionally during atomic manipulation.

[5]A tip exchange requires a full stop of the experiment, followed by approx. 5 h cooldown and a prepreparation of the Nb sample.
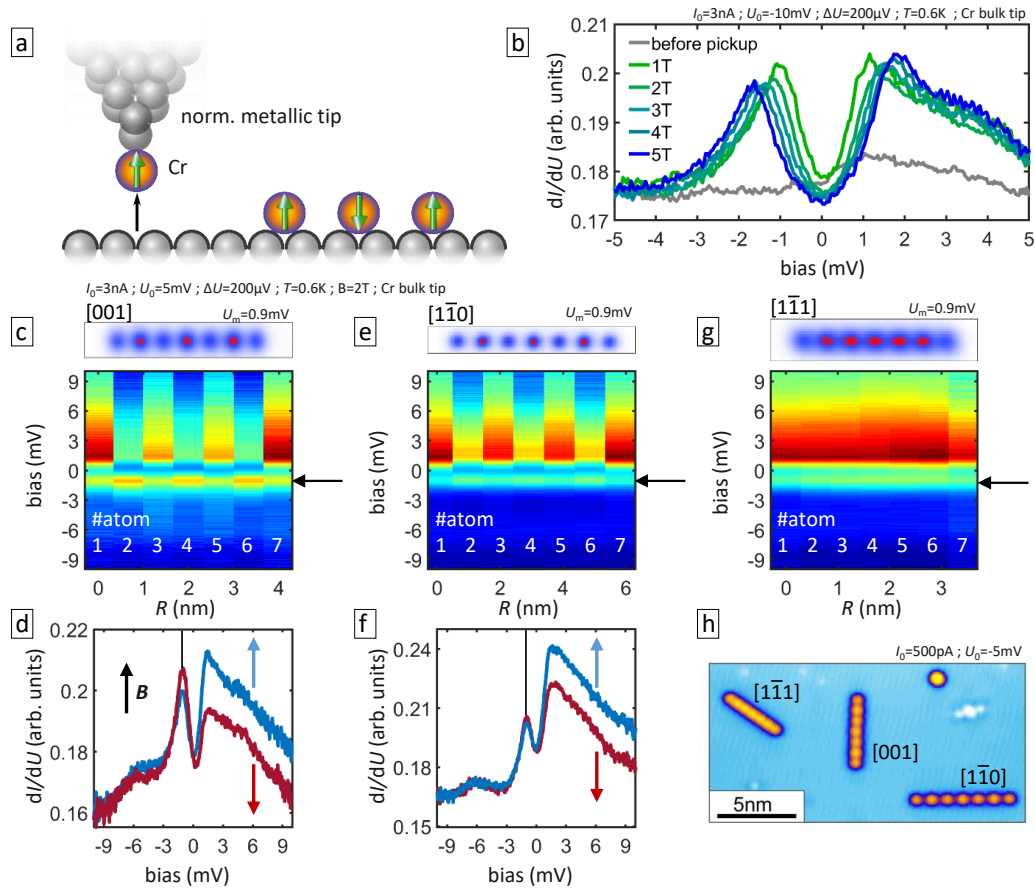
Fig. 4.30: **Cr functionalized W tip: a** Sketch of the functionalization of a W tip with a single Cr atom. **b** Comparison of STS taken on clean substrate before (grey) and after (color) Cr pick-up and magnetic field dependence of functionalized tip. **c-g** dI/dU maps and energy-resolved dI/dU cross sections with spin contrast on 7 atom Cr chains along three distinct directions, for AFM contrast **d,f** show SPS on atoms #3,4 for respective directions. Blue and red arrows show alignment with external magnetic field B = 2T applied out of plane. Black line (arrow in **c,e,g**) indicates energy of dI/dU maps. **h** Topography scan of the area with the three investigated chains.

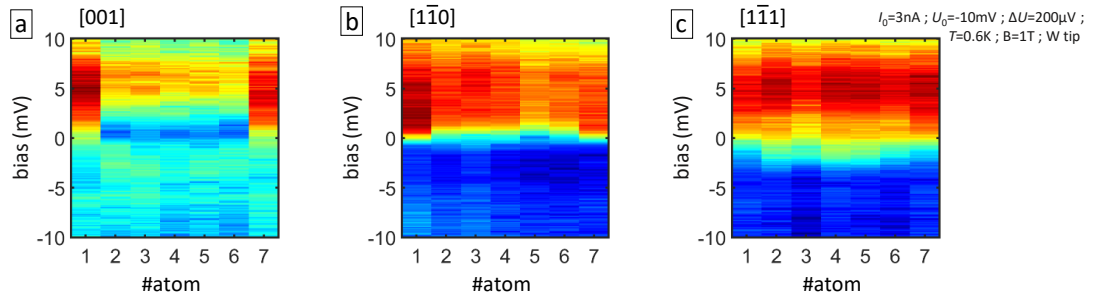**Fig.** 4.31: **Sensing magnetic order with a bare W tip:** STS along chains without a spin-polarized tip and applied field of 1 T out of plane. **a** $[001]$: Alternating behavior around zero is clearly visible. **b** $[1\bar{1}0]$: alternating order can be guessed but is obscured by bad datapoint on atom 5. **c** $[1\bar{1}1]$: Signal has no clear order, a bad datapoint can be inferred on atom 3. For all chains a distinct signal at the ends is observed.

the observed spin contrast with the Cr bulk tip it confirms that the chain magnetization follows the external field both for in plane and out of plane directions. Remarkably, the functionalization with a single Cr adatom yielded the clearest spin contrast out of the three tested methods. It means that two peaks in the DOS of opposite spin could be observed, simultaneously demonstrating anticorrelated intensity changes depending on the sample magnetization like highlighted in figure 4.30d,f. This is basically the situation which was envisioned in the method of spin polarized YSR spectroscopy described in the previous paragraph. Note that the peak at negative bias represents the tip unoccupied states, thus it enhances the signal for sample magnetization anti-aligned with the external field, i.e. even atom numbers in AFM chains $[001]$ and $[1\bar{1}0]$, while the tip occupied states at positive bias side favor tunneling of spin moments aligned with the field. From that one can also understand that the presented $\mathrm{d}I/\mathrm{d}U$ maps which were acquired at the energy of the negative bias peak show high intensity on the atoms that are anti-aligned to the tip magnetic moment which always matches the field direction. Due to low tip spin polarization at the Fermi level which dominates the signal at positive bias, no contrast was observed for $\mathrm{d}I/\mathrm{d}U$ maps at those voltages. Finally, the topography scan in figure 4.30h shows the area where the three measured chains were created, acquired with the functionalized tip. A close look at the chains reveal spin contrast even in the z profile created by the integrated LDOS.

Overall, the single Cr functionalization has proven very useful for atomic resolution spin polarized measurements, however, so far it lacks a refined method to reliably reproduce a working condition.

4.5.4 Bare tungsten tips

As outlined in section 4.3, the metallic phase response to magnetic nanostructures can be different for FM and AFM coupling. If this is sufficiently clear, a much easier deter-

mination of their magnetic order could be performed on unknown adatom formations by using a common bare tungsten tip. Data for 7 atom chains is shown in figure 4.31 for an out of plane field of 1 T. Consistent with previous results, the [001] chain exhibits a clear even-odd alternation in the observed feature around the Fermi level. However, the interpretation for directions [1$\bar{1}$0] and [1$\bar{1}$1] relies on very weak effects, only distinguishable after averaging over 25 acquired STS on each atom. Additionally, bad data points obscure the result even more. Taking into account the highly distinct signals at the ends leave only the 5 internal atoms for inferring a magnetic order. Therefore, to reduce the influence of bad data points, ideally longer chains would have to be used. Nevertheless, the biggest restriction for this method, especially when applying in two dimensions, is the strong directionality of the zero-bias feature which yields different accuracy depending on the measured structure. Conclusively, despite an influence of the magnetic order on the metallic response is very likely, it is by itself not suited to determine the magnetic state of nanostructures.

Summary

In summary, the use and exploration of four different experimental methods in addition to theoretical predictions in order to unravel the internal magnetic structure in coupled Cr adatoms and chains on Nb(110) is important and worth the effort, for the following reasons: (i) the challenging character of spin sensitive STM techniques up to day naturally benefits from the exploration of alternative routes to achieve spin contrast, (ii) information about the magnetic exchange is a crucial parameter for almost every theoretical model of the system, ultimately decisive for the physical understanding of those systems, therefore a robust and consistent result from different ways to probe it is of high value. Indeed, all four experimental attempts yielded consistent conclusions about the magnetic structure of Cr adatom chains along [001], [001] and [1$\bar{1}$1] (short distance). The result is of high reliability for the Cr bulk tip and the single Cr functionalized metallic tip. In the former case, a limited but sufficiently fix magnetization direction allowed to confirm a contrast reversion for opposite external fields strongly suggesting spin sensitivity. The second case, a single Cr pick-up, could compensate its free spin direction having well-separated DOS peaks of opposite spin polarization that nicely demonstrated anticorrelated behavior on magnetized chain atoms. The situation is less clear for the Fe$_2$ functionalized superconducting tip which exhibits very low spin polarization on Cr adatoms. Still, also here the correct information could be inferred by an observed energy shift of tip YSR resonances depending on the originally assumed magnetization on each chain atom. Finally magnetic order could be inferred even without tip functionalization from the intrinsic zero-bias anomalies on Cr adatoms exhibiting an alternating shape on AFM chains. However, directionality and low signal-to-noise ratio strongly limit its

usefulness as a magnetic probe on unknown structures.

The three different coupling configurations mentioned so far agree perfectly to the theory results from *ab inito* which emphasizes the accuracy of calculations, however, one additional configuration, i.e. $[1\bar{1}1]$ with a longer spacing of $0.86\,\mathrm{nm}$, did not show the predicted structure pointing out the complexity of the coupling and the importance of experimental determination.
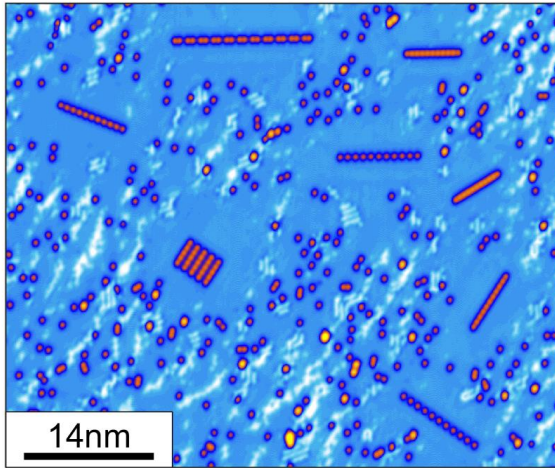
Figure: STM image of an area prepared for magnetic order determination with a Cr bulk tip, finally unsuccessful.

In upcoming experiments, more chain variations as well as two dimensional spin textures (see image to the left) shall be scrutinized with spin sensitive STM in order to ascertain the validity of theory models that can attempt to distinguish trivial and non-trivial boundaries on such structures based on the magnetic order which is crucial for their emergence.

4.6 2D spin nanostructures

Figure: Cr adatom assembly inspired by the Kagome lattice.

Two dimensional spin textures attract great fundamental and technological interest. Geometrical frustration, spin liquids and chiral textures like skyrmions are only some of the intriguing phenomena that appeal also for spintronics applications. A bottom-up approach buildin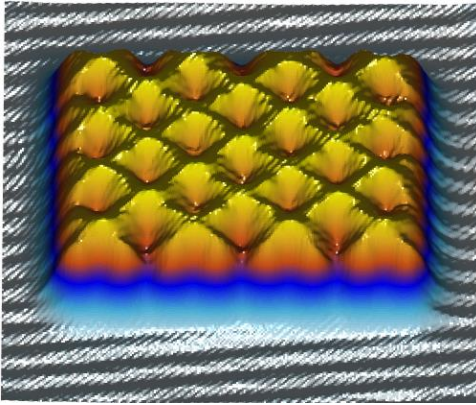g 2D magnetic structures on a superconductor where YSR resonances form two dimensional bands inside the superconducting gap has never been done in previously published studies.

This section will present results on several different 2D structures assembled atom-by-atom from magnetic Cr adatoms on Nb(110). However, the experiments on this topic are at present unfinished and moreover, the understanding of the observations is not yet on a satisfying level. Therefore this section shall give a mere outlook on this topic and will point out some trends derived from the observations made. In particular, it shall be investigated (i) to which extend the combination of different coupling directions can be seen as a superposition of dimer interactions scrutinized in section 4.2, (ii) what happens at boundaries like corners and edges and how their shape matters, (iii) whether the size of the assemblies matters and (iv) whether there are zero-energy boundary modes. The latter question is again asked with regard to topological superconductivity, however, like before an unambiguous result is not expected from these experiments.

4.6.1 Rectangular lattice, broken Symmetry and Frustration

At first, the focus shall be on two dimensional structures where the coupling mainly acts along the high symmetry directions $[001]$ and $[1\bar{1}0]$. Inevitably, a diagonal coupling along $[1\bar{1}1]$ arises as well, however, over the longest adatom distance. Thereby, a non-symmetric triangular assembly and a symmetric full rectangular one shall be scrutinized.

To characterize each adatom assembly, full spectroscopic grids have been acquired to obtain complete three dimensional information including two space and one energy dimension. Sampling rates provide spatial step sizes of $\approx 0.16\,\text{nm}$ and energy steps of $< 20\,\mu\text{V}$. Figure 4.32 shows results on the simplest triangular and rectangular structures. Topography images demonstrate a clean environment. The schematical plots define the color code referring to STS data on 2D structure adatoms (filled circles) and on adatom pairs along corresponding crystallographic directions from section 4.2 (lines). White arrows show an assumed spin alignment concluded from spin polarized measurements on adatom chains along $[001]$ and $[1\bar{1}0]$ in section 4.5 which both favor antiferromagnetic order.
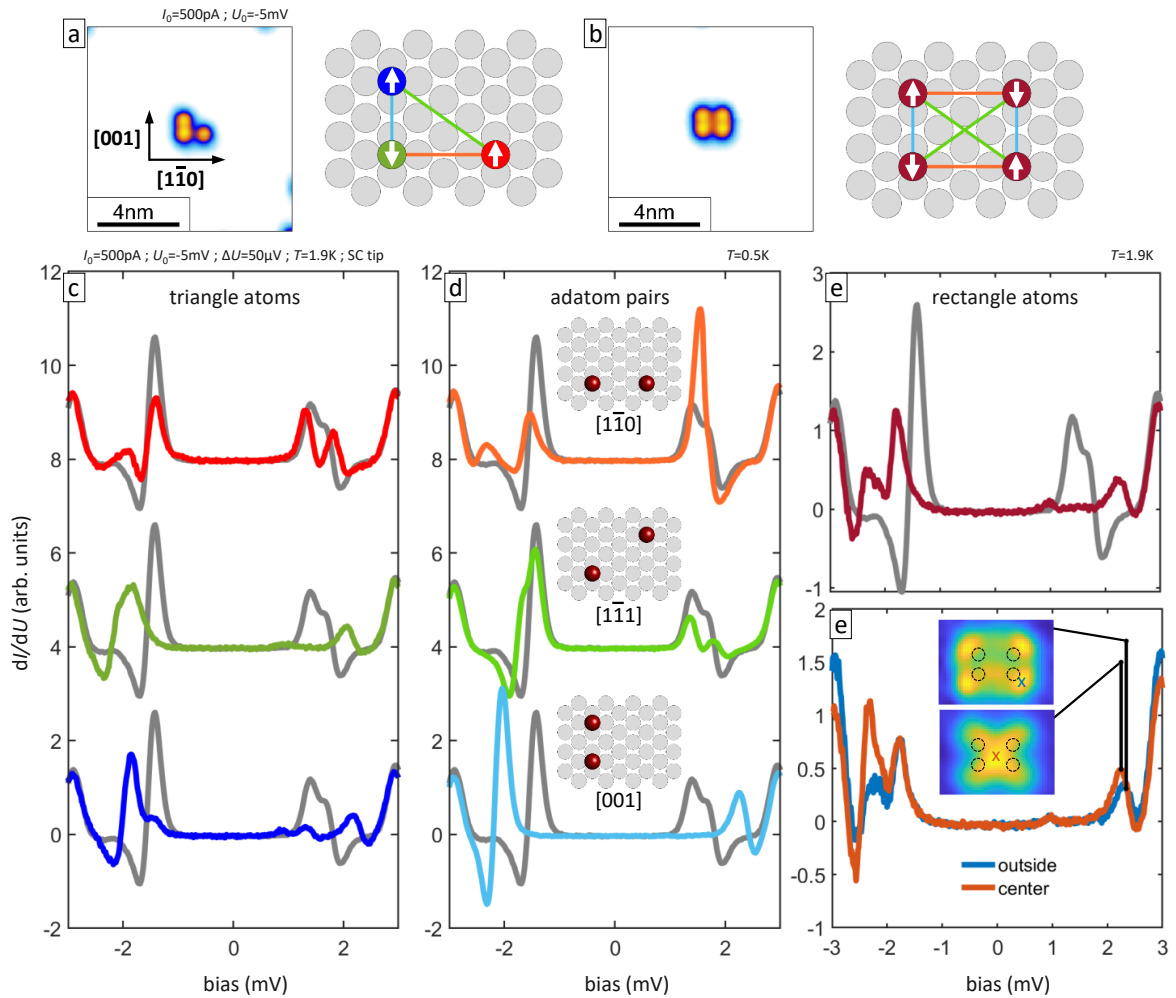
Fig. 4.32: **Superposition of dimer interaction: a** Topography image and lattice positions of 3 Cr adatoms in a triangular (**b** 4 atoms in a rectangular) arrangement. White arrows indicate assumed spin alignment. **c** STS on all 3 triangle atoms (colors like in **a**) with single Cr reference (grey). **d** STS on adatom pairs arranged like depicted in insets (colors correspond to lines in **a,b**). **e** STS on rectangle atoms (red) with single Cr reference (grey). **e** STS in 2 different positions on rectangle indicated in insets. Insets: dI/dU maps at 2 different energies indicated in STS plots showing split into bonding and antibonding state.

First, STS on the triangle structure (panel c) shall be compared to the separate pair interaction results (panel d). The most isolated triangle adatom depicted as a filled red circle is in 0.93 nm and 1.14 nm distance to the green and blue adatom, respectively. Its YSR spectrum drawn in red shows the dominant peak with nearly particle-hole symmetric intensity at $\pm\Delta_t$ marking the zero energy. Note that the grey isolated Cr reference data was obtained with the same microtip but at lower temperature, therefore signals are broadened on 2D structures and more intensity may appear inside the tip superconducting gap. Another well separated pair of peaks at $\pm$1.9 mV can be clearly identified. Looking at panel d, the interaction along $[1\bar{1}0]$ acts on the dominant d_{z^2} derived peak with a shift to positive energies across zero and promotes the d_{yz} derived peak on top of the atom at negative energies around -2.3 mV. In contrast, the interaction along $[1\bar{1}1]$ with 1.14 nm distance apparently shows minimal hybridization in the d_{z^2} peak and acts on the d_{xy} peak with a shift away from the Fermi level. This interpretation is consistent with geometrical expectations. Naturally, in the hybridization of orbitals between 3 adatoms, the result is more complex than just adding up coupled pair interactions, however, due to the strong indirect coupling component and relatively large adatom spacing, roughly both influences from $[1\bar{1}0]$ and $[1\bar{1}1]$ can be identified on the red triangle atom. One would expect that this is best observed on adatoms with rather large and comparable spacing to their neighbors like it is the case here. Coupling between the remaining two adatoms is governed by a strong negative shift of the d_{z^2} peak observed for the $[001]$ direction. It dominates the resulting spectra due to the strong shift, however, the peak on the green triangle atom appears somewhat closer to the Fermi level than on the adatom pair, being at around -1.9 mV and -2 mV, respectively. This might be attributed to the counteracting positive shift from the $[1\bar{1}0]$ interaction which is indeed of this order. Further, influence of the third adatom on YSR states derived from other orbitals can not be neglected and causes green and blue adatoms to be distinct, so that all three triangle atoms are different which reflects the asymmetry of this arrangement.

The substrate's twofold symmetry is recovered when adding the fourth adatom to complete a rectangle which makes all of them equivalent. The same spectrum is obtained on all four and shown in panel e. It is again dominated by $[001]$ coupling with strong d_{z^2} signal at -1.9 mV and 2.1 mV, showing another peak at -2.3 mV due to hybridization of other orbitals. Finally, in panel e, for the example of the positive energy peak on the 4 adatom rectangle, a splitting into bonding and antibonding states in both space and energy is demonstrated. Note that both states tend to overlap on top of the adatoms where most presented spectra are acquired leading to a broadening of the YSR peaks.

In the next step, the two dimensional assemblies are scaled up to 7 adatoms per edge, meaning 28 Cr adatoms in the triangle and 49 in the rectangle geometry. Topography images are presented in figure 4.33 a and b together with zero energy dI/dU maps corresponding to the added intensity at $\pm\Delta_t$. Here, both zero energy maps are shown with the
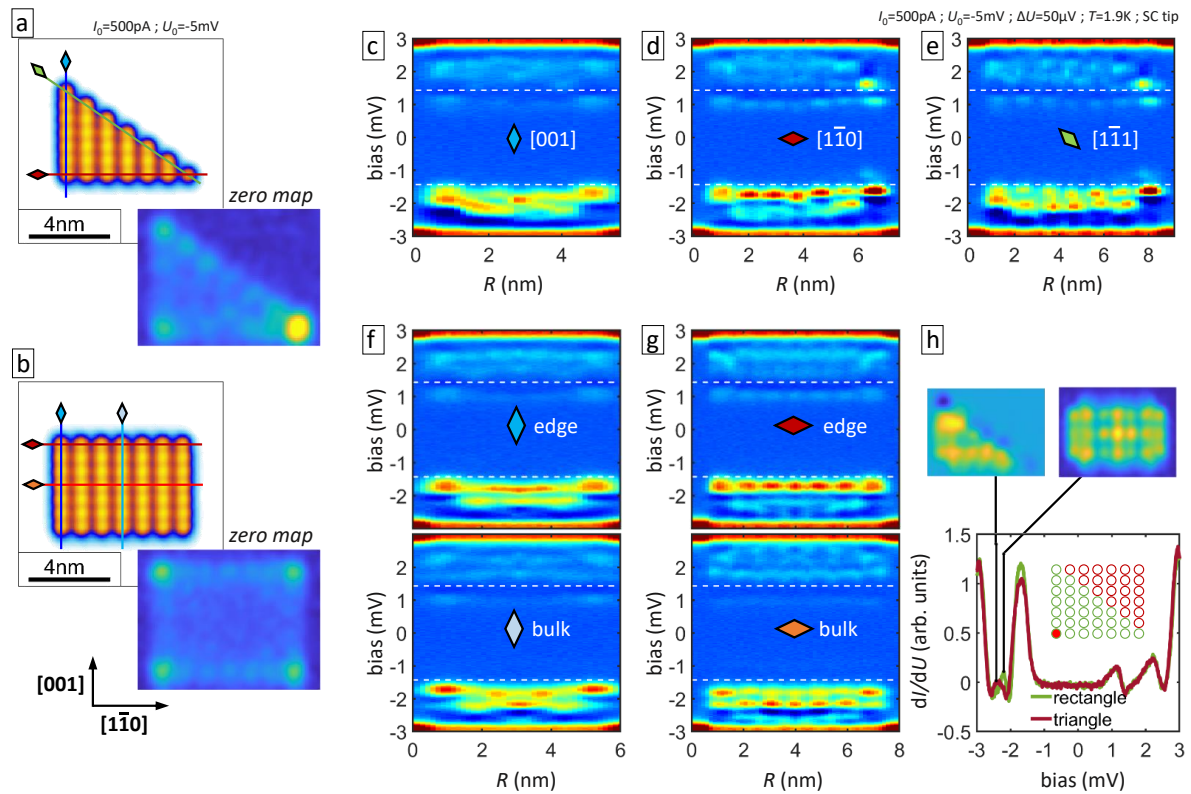
Fig. 4.33: **Bigger nanostructures: a** Topography image and zero energy dI/dU map (identical colorscale limits) of triangular lattice from 28 Cr adatoms, **b** rectangular lattice from 49 (7x7) adatoms. Colored lines with rhombic markers indicate paths of STS cross sections shown in **c-g**. Dashed white lines mark the tip superconducting gap. **h** Comparison of STS on the very same corner adatom inside the triangular (red) and rectangular (green) lattice shown as a filled red circle in the inset illustrating the lattice atoms. Above 2 dI/dU maps at indicated energies are shown for triangular (left) and rectangular (right) lattice.

Fig. 4.34: **Potentially non-collinear structures: a** 5 adatom arrangement with competing magnetic exchange couplings and hypothetical resulting spin alignment. **b** 73 adatom arrangement inspired by the Lieb lattice and containing 9 structures like shown in **a**. **c** 92 adatom arrangement inspired by the Kagome lattice.

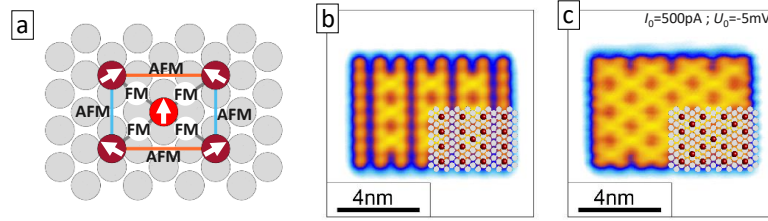same colorscale contrast to highlight differences and similarities. In general, the spectra are characterized by a negative shift of the dominant peak due to [001] coupling away from the Fermi level. Therefore nowhere in these two structures a zero energy peak is observed. However, like for the chains in section 4.4 a shift towards the Fermi level occurs together with accumulation of spectral weight at boundaries. This leads to higher intensity at zero at edges and even more at corners. By far the highest accumulation of spectral weight close to zero is found on the most isolated triangle atom which is essentially in a similar situation like in figure 4.32 for the 3 atom triangle not having a direct [001] coupling to other adatoms. Moreover, the triangle exhibits a rather irregular distribution along the edges better seen in figure 4.33c-e. The cross section along [001] might suggest a periodic shift of YSR states. Along [001] a discontinuity appears at the center of the edge, while the [1$\bar{1}$1] edge shows a more continuous change of energy shifts for each YSR state. Overall, the interplay of translational symmetry and missing mirror symmetry seems to produce an intriguing electronic structure that likely needs a larger number of unit cells to unfold regular patterns. In contrast to that, the twofold mirror symmetry of the rectangle produces expected patterns corresponding to dispersing bands with accumulation of spectral weight of low energy states at edges as seen in panels f and g. The corners are characterized by broader peaks close to zero with respect to the edges. Panel h compares the bottom left atom position in triangle and rectangle geometry. In both, it has the same immediate environment within at least 4 nm radius and indeed features very similar spectra in both cases. This again highlights the character of dilute adatom nanostructures where indirect coupling maintains an important role and the individual atoms can be considered separately to a certain degree. Despite being similar, the spectra are not identical, especially in the energy position of the less intense peak below −2 mV. It belongs to a bulk band as can be seen from the depicted dI/dU maps at corresponding peak energies for triangle and rectangle. As a consequence of the emergence of bonding and antibonding states shown in figure 4.32e, it demonstrates the creation of bands depending on the nanostructure as a whole, so that the individual atom description only considering an interaction radius of 4 nm is not fully sufficient.

So far, the spin texture of magnetic nanostructures could be quite easily guessed from the favored antiferromagnetic coupling demonstrated for the predominant coupling paths $[001]$ and $[1\bar{1}0]$ in the rectangular geometry. A difference in the superconducting regime between even and odd number of atoms resulting in a vanishing and non-vanishing residual magnetic moment, respectively, could not be observed. Although it could not yet be verified, assembling structures with competing ferro- and antiferromagnetic coupling of comparable strength may enable the design of nanostructures with non-collinear spin textures, without doubt a very interesting prospect for the field of atomic-scale magnetodynamics. According to DFT calculations[150] this requirement is met by Cr adatoms coupled along $[1\bar{1}1]$ with $0.57\,\mathrm{nm}$ and $[001]$ with $0.66\,\mathrm{nm}$ spacing. Like shown in figure 4.34a, inserting an atom in the center of the previously shown rectangle, realizes this combination. Two different nanostructures have been assembled containing this 5 atom unit, however, more experiments are needed to unravel their magnetic properties. Their design was inspired by famous literature examples, i.e. the Lieb[173] and the Kagome lattice[174,175]. Especially the latter is known for its intriguing quantum spin dynamics, electron correlations and even topological states.

4.6.2 Rhombic lattice

Another different geometry that has been built with some variations is the rhombic lattice. Like the rectangle it is characterized by twofold symmetry, the shortest adatoms distances are $0.85\,\mathrm{nm}$ along $[1\bar{1}1]$ and $0.99\,\mathrm{nm}$ along $[001]$. Out of those two, only for the $[1\bar{1}1]$ x3 coupling a spin sensitive result could be obtained and indicated antiferromagnetic coupling, thus AFM order is assumed for this geometry. Larger adatom assemblies have been built in the variations: empty bulk, filled bulk and rectangular edge cut.

Results are shown in figure 4.35. Panels a and b again show the simplest rhombus consisting of four adatoms. Like before, panels c and d compare the adatom pair interaction along the relevant directions with the rhombus atom spectra. The direction $[1\bar{1}0]$ was omitted here because of weak pair interaction. As one can expect from a geometrical point of view, the d_{xy} derived YSR state is likely main subject to hybridization and the formation of bands. In this configuration a lot of spectral weight remains around zero. Panels e,f and g show topography images of three rhombus variations, while in h, corresponding constant energy $\mathrm{d}I/\mathrm{d}U$ maps are depicted. The maps express the complexity of two dimensional YSR band creation where slightly different signals are obtained on almost every adatom in the assembly while obeying the twofold symmetry. For each variation a zero energy map is given. All three show significant spectral weight at zero over the whole structure so one can say in contrast to the rectangle structure that there is no bulk gap. Interestingly, while there is at least a slightly enhanced intensity at corners and edges of variations f and g like it was previously quite generally the case, variation e with-
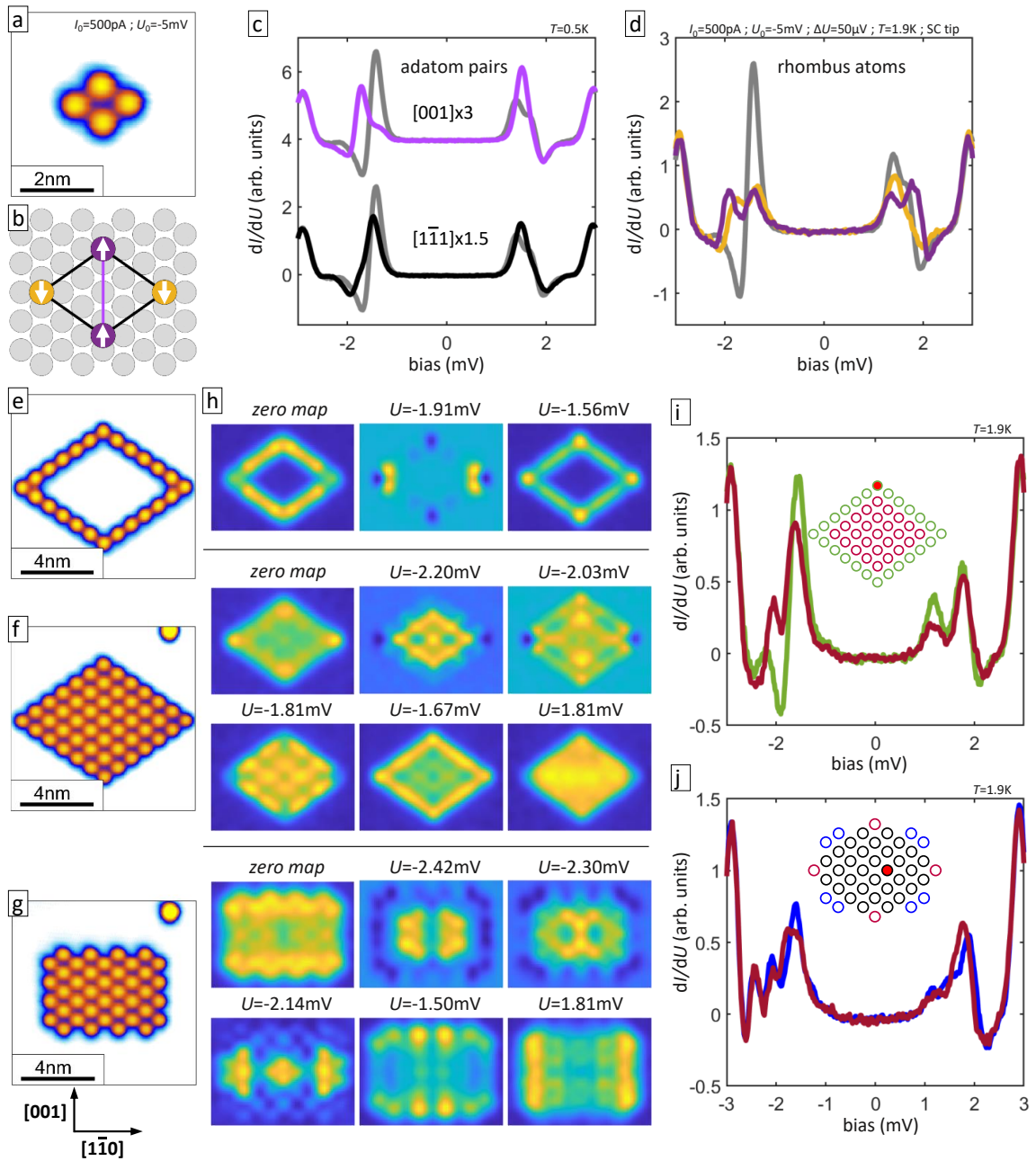
Fig. 4.35: **Rhombic lattice: a** Topographic image of 4 adatoms forming the rhombic lattice unit cell. **b** Lattice positions and spin alignments. Lines indicate interaction along specific directions shown as STS on adatom pairs in **c** with single Cr reference (grey). **d** STS on 2 different sites of adatoms shown in **a,b**. **e-g** Topography of 3 multi-cell rhombic lattice variations: empty bulk, filled bulk and varied boundary. **h** Several dI/dU maps at picked energies corresponding to structures to the left. **i,j** STS comparing same atom position (filled red circle) in similar structures: **i** rhombus filled (red) and empty (green), **j** filled rhombus with different boundary.

out bulk atoms shows less zero-energy intensity at its corners. A qualitative explanation could be that in this case the corners form triangles as two dimensional structures while in between there are one dimensional adatom wires. Spectral weight in general is more smeared out on 2D than on 1D structures. Another example for this can be seen in panel i where the same adatom corner position marked in red is compared for the filled and empty rhombus. In addition to three energetically almost equivalent peaks, a fourth one in the filled rhombus comes from the [001] interaction and seems to reduce the intensity for the other peaks, hence there is a flow of spectral weight to the additional peak. Finally figure 4.35j demonstrates a similar relation between individual atom and complete structure contributions like figure 4.33h for the rectangle. It compares a locally equivalent bulk atom position in the rhombus for different edge cuts. Despite being very much alike, small differences show that the YSR band formation depends on the boundary, at least for the here realized nanostructure sizes.

Trends & Outlook

The possibilities to design 2D geometries on this platform are large, and the assemblies realized so far demonstrate how YSR band formation can be tuned and engineered by different combination of adatom pair interaction and boundary shapes. Figure 4.36 shows an overview over all measured 2D nanostructures with a topography image and corresponding zero energy maps. Panels a-d each show the evolution by scaling up the size of a certain geometry. Owing to the dilute character, i.e. placing adatoms not in nearest neighbor sites made possible by their long range interaction, an asymptotic limit seems reached already at sizes of about 4 edge atoms for the low-energy states. The higher energy bands would need bigger structures to unfold their periodicity. Assemblies shown in e were built mostly out of scientific curiosity and inspired by other works, e.g. predicted controllable Majorana states in impurity-spin ring structures[102]. Unraveling the peculiar shape of their electronic states will be a task for upcoming theory models. In any case, to explore the possibility of creating topologically non-trivial bands which would be one major achievement in this field a close collaboration between theory and experiment is inevitable. At the end of this work such a collaboration was just established. Going beyond chain assemblies in versatile platforms of magnetic impurities on superconductors bears great potential, e.g. in the creation of crystalline topological superconductors from Shiba lattices, promising fruitful upcoming research.
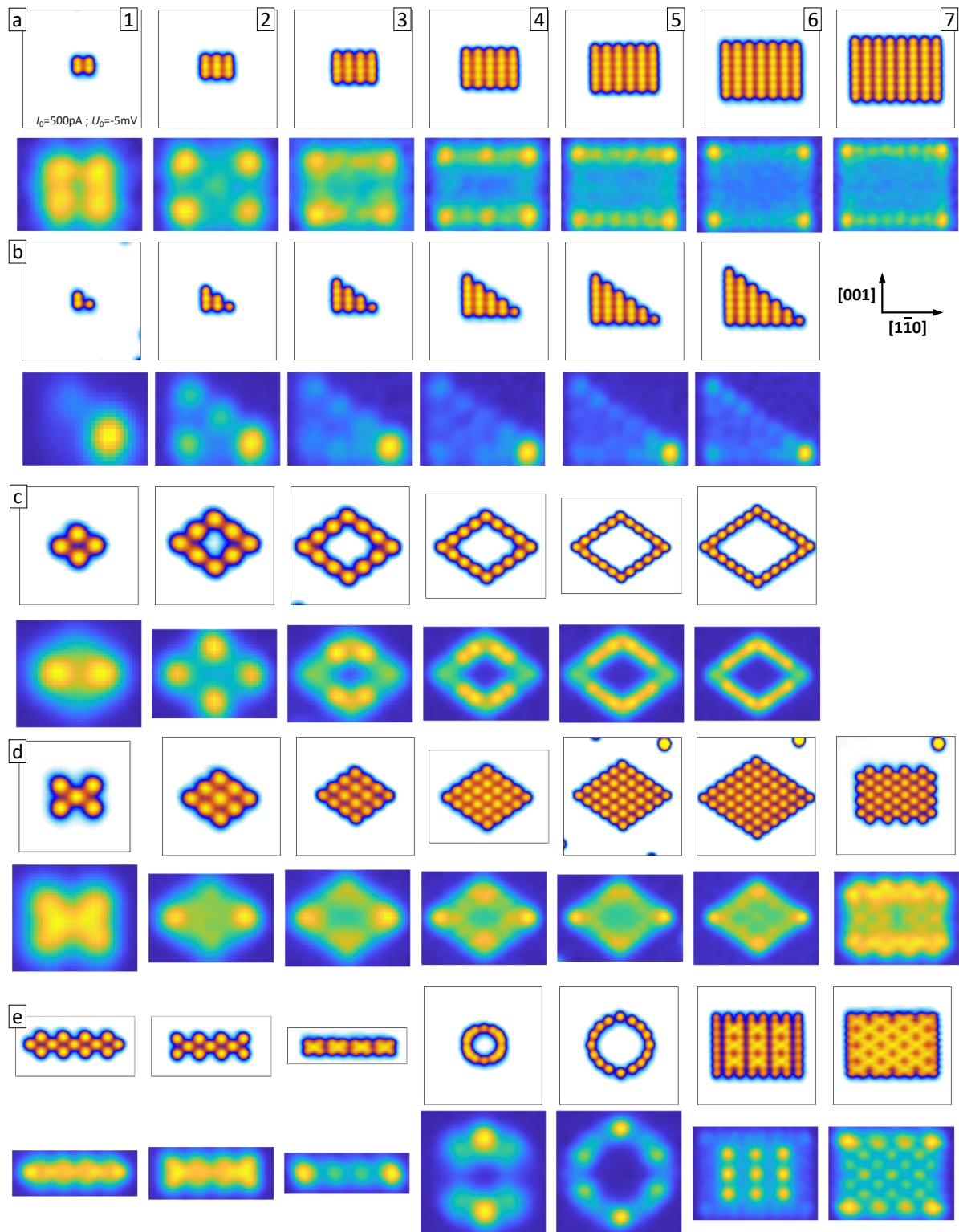
Fig. 4.36: **Realized magnetic nanostructures overview and corresponding zero energy dI/dU maps: a** Rectangular lattice 2x2...8x8. **b** Triangular lattice. **c** Rhombus empty bulk, **d** filled bulk. **e**1-3 chain-like, 4-5 ring-like assemblies, 6-7 superstructures inspired by Lieb lattice and Kagome lattice.

5 Conclusion & Outlook

This work has consistently followed systematic measurement protocols using a great variety of tools offered by STM to get access to well-defined trends in nanoscale interfaces of magnetism and superconductivity, a topic of ongoing debate in solid state physics. The system under test was the prototypical elemental s-wave superconductor Nb with magnetic impurity atoms in dilute concentration adsorbed to the clean Nb(110) surface.

An investigation of single isolated impurities from five $3d$ elements correlated the evaluation of angular momentum-resolved magnetic impurity-substrate coupling J inferred from YSR spectroscopy, relative quantification of a reduced superconducting order parameter via Josephson supercurrent analysis and the characteristics of zero-bias features in the system's metallic phase supported by first-principles calculations. A periodic behavior regarding the adatoms' spin moment throughout the subsequent order numbers was observed in agreement to calculations: Vanadium is weakly magnetic and couples ferromagnetically to the substrate, therefore induces no sub-gap states to superconductivity, has a small effect on Cooper pair tunneling and is featureless on metallic Nb. Chromium has a large spin moment which is screened ineffectively, inducing deep YSR states with its J being close to the critical value defining a quantum phase transition between ground and excited spin state, resulting in the by far strongest supercurrent reduction and a sharp step seen in metallic phase spectroscopy. Manganese and iron have high spin moments that are progressively screened more effectively by stronger coupling to the substrate, leading to shallow YSR states closer to the gap edge, less influence on superconductivity and broader signals in the metallic phase. Cobalt adatoms end up without any residual magnetic moment. Conclusively, a balanced impurity-substrate coupling with high spin moment avoids screening from the continuum of quasiparticles which results in the strongest detrimental influence on superconductivity. This balance is well-met for Cr d_{z^2} as well as d_{xy} states atop the Nb(110) surface crystal field.

The consequence is a low-energy quasiparticle wave propagating several nanometer away from the Cr adatom before being fully damped. From direct spatially resolved observation of YSR state hybridization between two impurities, oscillating patterns in distance dependent Cr-Cr interaction was observed up to 4 nm, where the mediation via overlapping YSR wave functions is fully attributed to the superconducting condensate. This results in a direct transfer of the Nb(110) Fermi surface anisotropy to a strongly directional impurity coupling. In order to characterize the Cr-Cr vector-dependent energy shift of sub-gap

resonances, a total of 31 impurity dimer configurations has been probed using atomic manipulation. Ultimately, a demonstration of hybridization induced, equilibrium state, controlled YSR state tuning through an energy range of approximately 2 meV across the quantum phase transition at zero energy is one of the highlights of this work.

In close collaboration to first-principles theory, the evolution of the sharp step-like zero-bias metallic phase response on Cr adatoms has been investigated in magnetic field, at elevated temperature as well as in dimer and trimer adatom rows. Despite a Kondo resonance as the origin of the spectral shape cannot be ruled out, the intriguing approach of an anomalous spin excitation feature could explain the observations well. Splitting minority and majority spin channels in external fields might prove useful insight with regard to spintronics devices. A crucial role of the magnetic exchange coupling, i.e. ferro- or antiferromagnetic, was pointed out for the dimer and trimer spectra, as well as the substrate anisotropy in determining it.

The search for topological superconductivity and Majorana zero modes in proximitized spin chains so far lacked a test platform with sufficient control over a large set of parameters. Cr quantum impurities on Nb(110) embody this requirement, therefore a big-scale study of one dimensional assemblies has been conducted building a Cr chain step-by-step, tuning the length, crystallographic angle, hopping amplitudes and magnetic exchange. Irrespective of most variations, a general trend of spectral weight redistribution was identified: chain ends accumulate intensity at low energies, bulk modes at higher energies form dispersing Shiba-bands. Certain chains match criteria for Majorana end modes, being particle-hole symmetric end locked at zero energy. Additional concepts to distinguish topological modes, i.e. introducing artificial boundaries or modulating the hopping amplitude, did not rule out their existence. However, a minimal trivial-regime tight-binding model confirmed the origin of the above stated trend to be non-topological and reproduced all test results with suitable parameters. In conclusion, despite controlling a huge parameter space non-trivial end modes are not distinguishable from trivial ones.

In order to theoretically elucidate spin nanostructures and to create one and two dimensional assemblies with tailored magnetic properties, a decisive role is played by the sign of exchange interaction. Its experimental determination on the atomic scale is a challenging but powerful way to use the STM. Three methods to obtain spin-polarized tunneling have been tested and compared. Less useful was tip functionalization with a superconducting Nb cluster and an iron dimer on the apex to employ spin-polarized YSR states for sensing magnetic orientations. Despite being conceptually the most promising, measurements yielded very weak spin contrast. Both Cr bulk tip and single Cr *in situ* functionalization yielded good results, however, with low success rates. The magnetic order of three distinct Cr chains along different crystallographic directions has been consistently determined: [001] (adatom distance 0.66 nm) and [1$\bar{1}$0] (0.93 nm) are antiferromagnetic while [1$\bar{1}$1] (0.57 nm) has ferromagnetic order.

This work ends with an outlook into two dimensional assemblies, potentially extending concepts established so far to experimentally nail down the border between trivial and topological phases. After retracing the YSR signatures from dimers over chains to 2D lattices and observations of bulk Shiba bands as well as spectral weight accumulation at edges and corners, different concepts inspired the assembly of ring-structures and potentially frustrated spin lattices. However, both experimental and theoretical characterization are at an incomplete stage.

Considering the extensive research on 1D spin structures yet remains scratching the surface of topological superconductivity, the future search for exciting physics at the artificially crafted quantum spin-to-superconductor interface will likely progressively take advantage of the additional prospects of the second space dimension. The results of this thesis pave the way for a large-scale study on proximitized tailored spin textures featuring Shiba bands well inside the superconducting quasiparticle gap. Spin-triplet supercurrents and braiding concepts for Majorana modes may thus find new approaches for realization.

Not all results in this work are well-understood, yet it poses an extensive and coherent exploration of maybe the most controlled, tunable and formable quantum spin-to-superconductor interface system studied up to date.

Postface

Just around the time when Onnes discovered Superconductivity, Albert Einstein formulated a general theory of relativity[176]. For now more than 100 years scientists merely confirm implications of his ideas.

However, solid matter with its full spectrum of many-body phenomena not seldomly leaves nuts uncracked even for the most powerful theoretical methods. In the previous chapters it occasionally proved challenging to explain the experiment with theory models to a satisfactory extend. This promotes the abiding importance of experiments unveiling the unforeseen rather than just confirming predictions or as Onnes has put it: "Through measurement to knowledge."

Acknowledgments

I would like to express sincerest gratitude to everyone who supported me on my way, gave me the chance to work in a modern research laboratory and contributed to this work with ideas, discussions, comments, and patience during the writing process.

First I want to thank Prof. *Torsten Fritz* from the Friedrich-Schiller-University in Jena for all the support since the beginning of my Master in Jena and together with *Dr. Yutaka Miyatake* and *Dr. Takeshi Miura* from Unisoku in Osaka made me aware of the fascinations in scanning probe microscopy. Without them I would not have had the chance to learn a lot about lab work while being abroad in Japan which is like a second home to me.

Deepest gratitude to *Prof. Stuart Parkin* for accepting me as a PhD student at the Max Planck Institute in Halle, for being my doctoral supervisor and continuously supporting me on my way without hesitation.

Very special thanks to *Dr. Paolo Sessi* for being a great mentor and friend, sharing his long experience of research with scanning tunneling microscopes and for being the most understanding person for work-related as well as personal problems. For me, the work atmosphere in the STM lab could not have been better. He gave me the chance to gain experience with many different samples exhibiting a great variety of physical phenomena. Ultimately, he is the person who made this particular project and thesis possible.

I am happy that I had the chance to work together with *Prof. Samir Lounis*, *Dr. Sascha Brinker*, *Ana Montero*, *Filipe Guimarães* from Forschungszentrum Jülich, *Prof. Daniel Loss*, *Prof. Jelena Klinovaja*, *Richard Hess* from the University of Basel, as well as *Prof. Titus Neupert* and *Martina Soldini* from the University of Zurich, who all put a lot of effort for an understanding of atomic scale magnetic-superconductor interfaces employing powerful theory models and calculations and who were available for many fruitful discussions about our measurement data.

Finally a huge thank you to an incredibly loving and patient family who had to face tough times during the writing process and regardless gave me support and motivation to carry on.

References

[1] Laesecke, A. Through measurement to knowledge: The inaugural lecture of Heike Kamerlingh Onnes (1882). *Journal of research of the National Institute of Standards and Technology* **107**, 261–277 (2002).

[2] Onnes, H. K. *Commun. Physical Lab., Univ. Leiden* **37**, 133–144 (Suppl. 34b) (1913).

[3] Parkin, S. & Yang, S.-H. Memory on the racetrack. *Nature nanotechnology* **10**, 195–198 (2015).

[4] Linder, J. & Robinson, J. W. A. Superconducting spintronics. *Nature Physics* **11**, 307–315 (2015).

[5] Sarma, S. D., Freedman, M. & Nayak, C. Majorana zero modes and topological quantum computation. *npj Quantum Information* **1**, 15001 (2015).

[6] Nadj-Perge, S., Drozdov, I. K., Bernevig, B. A. & Yazdani, A. Proposal for realizing Majorana fermions in chains of magnetic atoms on a superconductor. *Physical Review B* **88**, 20407(R) (2013).

[7] Pientka, F., Glazman, L. I. & von Oppen, F. Topological superconducting phase in helical Shiba chains. *Physical Review B* **88**, 155420 (2013).

[8] Alicea, J. New directions in the pursuit of Majorana fermions in solid state systems. *Reports on progress in physics. Physical Society (Great Britain)* **75**, 076501 (2012).

[9] Klinovaja, J., Stano, P., Yazdani, A. & Loss, D. Topological superconductivity and Majorana fermions in RKKY systems. *Physical review letters* **111**, 186805 (2013).

[10] Bardeen, J., Cooper, L. N. & Schrieffer, J. R. Theory of superconductivity. *Physical Review* **108**, 1175–1204 (1957).

[11] Yu, L. Bound state in superconductors with paramagnetic impurities. *Acta Physica Sinica* **21**, 75–98 (1965). URL `http://wulixb.iphy.ac.cn/en/article/id/851`.

[12] Shiba, H. Classical spins in superconductors. *Progress of Theoretical Physics* **40**, 435–451 (1968).

[13] Rusinov, A. I. On the theory of gapless superconductivity in alloys containing paramagnetic impurities. *JETP* **29**, 1101–1106 (1969). URL `http://www.jetp.ac.ru/cgi-bin/dn/e_029_06_1101.pdf`.

[14] Yazdani, Jones, Lutz, Crommie & Eigler. Probing the local effects of magnetic impurities on superconductivity. *Science (New York, N.Y.)* **275**, 1767–1770 (1997).

[15] Franke, K. J., Schulze, G. & Pascual, J. I. Competition of superconducting phenomena and Kondo screening at the nanoscale. *Science (New York, N.Y.)* **332**, 940–944 (2011).

[16] Ruby, M. *et al.* Tunneling processes into localized subgap states in superconductors. *Physical review letters* **115**, 087001 (2015).

[17] Ruby, M., Peng, Y., von Oppen, F., Heinrich, B. W. & Franke, K. J. Orbital picture of Yu-Shiba-Rusinov multiplets. *Physical review letters* **117**, 186801 (2016).

[18] Ruby, M., Heinrich, B. W., Peng, Y., von Oppen, F. & Franke, K. J. Wave-function hybridization in Yu-Shiba-Rusinov dimers. *Physical review letters* **120**, 156803 (2018).

[19] Farinacci, L. *et al.* Tuning the coupling of an individual magnetic impurity to a superconductor: Quantum phase transition and transport. *Physical review letters* **121**, 196803 (2018).

[20] Farinacci, L. *et al.* Interfering tunneling paths through magnetic molecules on superconductors: Asymmetries of Kondo and Yu-Shiba-Rusinov resonances. *Physical review letters* **125**, 256805 (2020).

[21] Choi, D.-J. *et al.* Mapping the orbital structure of impurity bound states in a superconductor. *Nature communications* **8**, 15175 (2017).

[22] Choi, D.-J. *et al.* Influence of magnetic ordering between Cr adatoms on the Yu-Shiba-Rusinov states of the β-Bi_2Pd superconductor. *Physical review letters* **120**, 167001 (2018).

[23] Kezilebieke, S., Dvorak, M., Ojanen, T. & Liljeroth, P. Coupled Yu-Shiba-Rusinov states in molecular dimers on $NbSe_2$. *Nano letters* **18**, 2311–2315 (2018).

[24] Ménard, G. C. *et al.* Coherent long-range magnetic bound states in a superconductor. *Nature Physics* **11**, 1013–1016 (2015).

[25] Ménard, G. C. *et al.* Two-dimensional topological superconductivity in Pb/Co/Si(111). *Nature communications* **8**, 2040 (2017).

[26] Kim, Y., Zhang, J., Rossi, E. & Lutchyn, R. M. Impurity-induced bound states in superconductors with spin-orbit coupling. *Physical review letters* **114**, 236804 (2015).

[27] Kim, H., Rózsa, L., Schreyer, D., Simon, E. & Wiesendanger, R. Long-range focusing of magnetic bound states in superconducting lanthanum. *Nature communications* **11**, 4573 (2020).

[28] Schneider, L., Beck, P., Wiebe, J. & Wiesendanger, R. Atomic-scale spin-polarization maps using functionalized superconducting probes. *Science Advances* **7**, eabd7302 (2021).

[29] Beck, P. *et al.* Spin-orbit coupling induced splitting of Yu-Shiba-Rusinov states in antiferromagnetic dimers. *Nature communications* **12**, 2040 (2021).

[30] Huang, H. *et al.* Spin-dependent tunneling between individual superconducting bound states. *Physical Review Research* **3**, L032008 (2021).

[31] Odobesko, A. *et al.* Observation of tunable single-atom Yu-Shiba-Rusinov states. *Physical Review B* **102**, 174504 (2020).

[32] Nadj-Perge, S. *et al.* Topological matter. Observation of Majorana fermions in ferromagnetic atomic chains on a superconductor. *Science (New York, N.Y.)* **346**, 602–607 (2014).

[33] Ruby, M. *et al.* End states and subgap structure in proximity-coupled chains of magnetic adatoms. *Physical review letters* **115**, 197204 (2015).

[34] Kamlapure, A., Cornils, L., Wiebe, J. & Wiesendanger, R. Engineering the spin couplings in atomically crafted spin chains on an elemental superconductor. *Nature communications* **9**, 3253 (2018).

[35] Schneider, L. *et al.* Controlling in-gap end states by linking nonmagnetic atoms and artificially-constructed spin chains on superconductors. *Nature communications* **11**, 4707 (2020).

[36] Schneider, L. *et al.* Topological Shiba bands in artificial spin chains on superconductors. *Nature Physics* **17**, 943–948 (2021).

[37] Schneider, L. *et al.* Precursors of Majorana modes and their length-dependent energy oscillations probed at both ends of atomic Shiba chains. *Nature nanotechnology* **17**, 384–389 (2022).

[38] Liebhaber, E. *et al.* Quantum spins and hybridization in artificially-constructed chains of magnetic adatoms on a superconductor. *Nature communications* **13**, 2160 (2022).

[39] Friedrich, F., Boshuis, R., Bode, M. & Odobesko, A. Coupling of Yu-Shiba-Rusinov states in one-dimensional chains of Fe atoms on Nb(110). *Physical Review B* **103**, 235437 (2021).

[40] Flensberg, K., von Oppen, F. & Stern, A. Engineered platforms for topological superconductivity and Majorana zero modes. *Nature Reviews Materials* **6**, 944–958 (2021).

[41] Steiner, J. F., Mora, C., Franke, K. J. & von Oppen, F. Quantum magnetism and topological superconductivity in Yu-Shiba-Rusinov chains. *Physical review letters* **128**, 036801 (2022).

[42] Larbalestier, D. & Canfield, P. C. Superconductivity at 100—where we've been and where we're going. *MRS Bulletin* **36**, 590–593 (2011).

[43] Berlincourt, T. Type II superconductivity: Quest for understanding. *IEEE Transactions on Magnetics* **23**, 403–412 (1987).

[44] Meissner, W. & Ochsenfeld, R. Ein neuer Effekt bei Eintritt der Supraleitfähigkeit. *Die Naturwissenschaften* **21**, 787–788 (1933).

[45] De Haas, D. & Voogd, J. *Commun. Physical Lab., Univ. Leiden* **9**, 214b (1913).

[46] Schubnikow, L., Chotkewitsch, W., Schepelew, J. & Rjabinin, J. Arbeiten auf dem Gebiete tiefer Temperaturen. *Sondernummer Phys. Z. Sowjet* **39** (1936).

[47] London, F. & London, H. The electromagnetic equations of the supraconductor. *Proceedings of the Royal Society of London. Series A - Mathematical and Physical Sciences* **149**, 71–88 (1935).

[48] Landau, L. D. & Ginzburg, V. L. On the theory of superconductivity. *Zh. Eksp. Teor. Fiz., Phys. Z. Sowjetunion* **20**, 1064–1082 (1950).

[49] Abrikosov, A. A. On the magnetic properties of superconductors of the second group. *Sov. Phys. JETP* **5**, 1174–1182 (1957).

[50] Bednorz, J. G. & Müller, K. A. Possible high T_c superconductivity in the Ba-La-Cu-O system. *Zeitschrift für Physik B Condensed Matter* **64**, 189–193 (1986).

[51] Ishida, K., Nakai, Y. & Hosono, H. To what extent iron-pnictide new superconductors have been clarified: A progress report. *Journal of the Physical Society of Japan* **78**, 062001 (2009).

[52] Snider, E. *et al.* Room-temperature superconductivity in a carbonaceous sulfur hydride. *Nature* **586**, 373–377 (2020).

[53] Kleiner, R. & Buckel, W. *Superconductivity: An Introduction* (Wiley-VCH, s.l., 2015), 3. edn.

[54] Fu, L. & Kane, C. L. Superconducting proximity effect and Majorana fermions at the surface of a topological insulator. *Physical review letters* **100**, 096407 (2008).

[55] Majorana, E. Teoria simmetrica dell'elettrone e del positrone. *Il Nuovo Cimento* **14**, 171–184 (1937).

[56] Kitaev, A. Fault-tolerant quantum computation by anyons. *Annals of Physics* **303**, 2–30 (2003).

[57] Schrieffer, J. R. *Theory of superconductivity*, vol. 20 of *Frontiers in physics* (Addison-Wesley, Redwood City, Calif., 1988), 4. print edn.

[58] de Gennes, P.-G. *Superconductivity of metals and alloys.* Advanced book program (CRC Press Taylor & Francis Group, Boca Raton and London and New York, 2018).

[59] Tinkham, M. *Introduction to superconductivity.* Dover books on physics (Dover Publ, Mineola, NY, 2004), 2. edn.

[60] Balatsky, A. V., Vekhter, I. & Zhu, J.-X. Impurity-induced states in conventional and unconventional superconductors. *Reviews of Modern Physics* **78**, 373–433 (2006).

[61] Fernandes, R. M. Lecture notes: Bcs theory of superconductivity. URL `https://portal.ifi.unicamp.br/images/files/graduacao/aulas-on-line/fen-emerg/lecture_notes_BCS.pdf`. Institute of Physics, University of Campinas.

[62] Kondo, J. Resistance minimum in dilute magnetic alloys. *Progress of Theoretical Physics* **32**, 37–49 (1964).

[63] Sakai, O., Shimizu, Y., Shiba, H. & Satori, K. Numerical renormalization group study of magnetic impurities in superconductors. ii. dynamical excitation spectra and spatial variation of the order parameter. *Journal of the Physical Society of Japan* **62**, 3181–3197 (1993).

[64] Heinrich, B. W., Pascual, J. I. & Franke, K. J. Single magnetic adsorbates on s -wave superconductors. *Progress in Surface Science* **93**, 1–19 (2018).

[65] Salkola, M. I., Balatsky, A. V. & Schrieffer, J. R. Spectral properties of quasiparticle excitations induced by magnetic moments in superconductors. *Physical review. B, Condensed matter* **55**, 12648–12661 (1997).

[66] Martín-Rodero, A. & Yeyati, A. L. The Andreev states of a superconducting quantum dot: mean field versus exact numerical results. *Journal of physics. Condensed matter : an Institute of Physics journal* **24**, 385303 (2012).

[67] Žonda, M., Pokorný, V., Janiš, V. & Novotný, T. Perturbation theory of a superconducting 0 - π impurity quantum phase transition. *Scientific reports* **5**, 8821 (2015).

[68] Žonda, M., Pokorný, V., Janiš, V. & Novotný, T. Perturbation theory for an Anderson quantum dot asymmetrically attached to two superconducting leads. *Physical Review B* **93**, 024523 (2016).

[69] Shiba, H., Satori, K., Sakai, O. & Shimizu, Y. Numerical renormalization group study of the Kondo effect in superconductors. *Physica B: Condensed Matter* **186-188**, 239–241 (1993).

[70] Bauer, J., Oguri, A. & Hewson, A. C. Spectral properties of locally correlated electrons in a Bardeen–Cooper–Schrieffer superconductor. *Journal of Physics: Condensed Matter* **19**, 486211 (2007).

[71] žitko, R. Quantum impurity models for magnetic adsorbates on superconductor surfaces. *Physica B: Condensed Matter* **536**, 230–234 (2018).

[72] Golež, D., Bonča, J. & žitko, R. Vibrational Andreev bound states in magnetic molecules. *Physical Review B* **86**, 085142 (2012).

[73] Pershoguba, S. S., Björnson, K., Black-Schaffer, A. M. & Balatsky, A. V. Currents induced by magnetic impurities in superconductors with spin-orbit coupling. *Physical review letters* **115**, 116602 (2015).

[74] Kaladzhyan, V., Bena, C. & Simon, P. Characterizing p-wave superconductivity using the spin structure of Shiba states. *Physical Review B* **93**, 214514 (2016).

[75] Pershoguba, S. S., Nakosai, S. & Balatsky, A. V. Skyrmion-induced bound states in a superconductor. *Physical Review B* **94**, 064513 (2016).

[76] žitko, R., Bodensiek, O. & Pruschke, T. Effects of magnetic anisotropy on the subgap excitations induced by quantum impurities in a superconducting host. *Physical Review B* **83**, 054512 (2011).

[77] Moca, C. P., Demler, E., Jankó, B. & Zaránd, G. Spin-resolved spectra of Shiba multiplets from Mn impurities in MgB_2. *Physical Review B* **77**, 174516 (2008).

[78] žitko, R. Spectral properties of Shiba subgap states at finite temperatures. *Physical Review B* **93**, 195125 (2016).

[79] Flatté, M. E. & Reynolds, D. E. Local spectrum of a superconductor as a probe of interactions between magnetic impurities. *Physical review. B, Condensed matter* **61**, 14810–14814 (2000).

[80] Morr, D. K. & Stavropoulos, N. A. Quantum interference between impurities: Creating novel many-body states in s -wave superconductors. *Physical review. B, Condensed matter* **67** (2003).

[81] Morr, D. K. & Yoon, J. Impurities, quantum interference, and quantum phase transitions in s -wave superconductors. *Physical Review B* **73**, 224511 (2006).

[82] Yao, N. Y., Glazman, L. I., Demler, E. A., Lukin, M. D. & Sau, J. D. Enhanced antiferromagnetic exchange between magnetic impurities in a superconducting host. *Physical review letters* **113**, 087202 (2014).

[83] Yao, N. Y. *et al.* Phase diagram and excitations of a Shiba molecule. *Physical Review B* **90**, 241108 (2014).

[84] Ruderman, M. A. & Kittel, C. Indirect exchange coupling of nuclear magnetic moments by conduction electrons. *Physical Review* **96**, 99–102 (1954).

[85] Kasuya, T. A theory of metallic ferro- and antiferromagnetism on Zener's model. *Progress of Theoretical Physics* **16**, 45–57 (1956).

[86] Yosida, K. Magnetic properties of Cu-Mn alloys. *Physical Review* **106**, 893–898 (1957).

[87] Parkin, S., More, N. & Roche, K. Oscillations in exchange coupling and magnetoresistance in metallic superlattice structures: Co/Ru, Co/Cr, and Fe/Cr. *Physical review letters* **64**, 2304–2307 (1990).

[88] Parkin, S. & Mauri, D. Spin engineering: Direct determination of the Ruderman-Kittel-Kasuya-Yosida far-field range function in ruthenium. *Physical review. B, Condensed matter* **44**, 7131–7134 (1991).

[89] Parkin, S. Systematic variation of the strength and oscillation period of indirect magnetic exchange coupling through the 3d, 4d, and 5d transition metals. *Physical review letters* **67**, 3598–3601 (1991).

[90] Zhou, L. *et al.* Strength and directionality of surface Ruderman–Kittel–Kasuya–Yosida interaction mapped on the atomic scale. *Nature Physics* **6**, 187–191 (2010).

[91] Matthias, B. T., Suhl, H. & Corenzwit, E. Spin exchange in superconductors. *Physical review letters* **1**, 92–94 (1958).

[92] Woolf, M. A. & Reif, F. Effect of magnetic impurities on the density of states of superconductors. *Physical Review* **137**, A557–A564 (1965).

[93] Rohrer, H. & Binnig, G. Scanning tunneling microscopy. *Surface Science* **126**, 236–244 (1983).

[94] Wiesendanger, R., Anselmetti, D. & Güntherodt, H.-J. Advances in STM design and instrumentation. *Europhysics News* **21**, 72–73 (1990).

[95] Ji, S.-H. *et al.* High-resolution scanning tunneling spectroscopy of magnetic impurity induced bound states in the superconducting gap of Pb thin films. *Physical review letters* **100**, 226801 (2008).

[96] Ji, S.-H. *et al.* Application of magnetic atom induced bound states in superconducting gap for chemical identification of single magnetic atoms. *Applied Physics Letters* **96**, 073113 (2010).

[97] Ast, C. R. *et al.* Sensing the quantum limit in scanning tunnelling spectroscopy. *Nature communications* **7**, 13009 (2016).

[98] Kitaev, A. Y. Unpaired Majorana fermions in quantum wires. *Physics-Uspekhi* **44**, 131–136 (2001).

[99] Beenakker, C. Search for Majorana fermions in superconductors. *Annual Review of Condensed Matter Physics* **4**, 113–136 (2013).

[100] Li, J. *et al.* Topological superconductivity induced by ferromagnetic metal chains. *Physical Review B* **90**, 235433 (2014).

[101] Prada, E. *et al.* From Andreev to Majorana bound states in hybrid superconductor–semiconductor nanowires. *Nature Reviews Physics* **2**, 575–594 (2020).

[102] Li, J., Neupert, T., Bernevig, B. A. & Yazdani, A. Manipulating Majorana zero modes on atomic rings with an external magnetic field. *Nature communications* **7**, 10395 (2016).

[103] Ternes, M. *et al.* Subgap structure in asymmetric superconducting tunnel junctions. *Physical Review B* **74**, 132501 (2006).

[104] Josephson, B. D. Possible new effects in superconductive tunnelling. *Physics Letters* **1**, 251–253 (1962).

[105] Randeria, M. T., Feldman, B. E., Drozdov, I. K. & Yazdani, A. Scanning Josephson spectroscopy on the atomic scale. *Physical Review B* **93**, 161115(R) (2016).

[106] Hatter, N., Heinrich, B. W., Ruby, M., Pascual, J. I. & Franke, K. J. Magnetic anisotropy in Shiba bound states across a quantum phase transition. *Nature communications* **6**, 8988 (2015).

[107] Hatter, N., Heinrich, B. W., Rolf, D. & Franke, K. J. Scaling of Yu-Shiba-Rusinov energies in the weak-coupling Kondo regime. *Nature communications* **8**, 2016 (2017).

[108] Karan, S. *et al.* Superconducting quantum interference at the atomic scale. URL http://arxiv.org/pdf/2102.12521v2.

[109] Roth, L. M., Zeiger, H. J. & Kaplan, T. A. Generalization of the Ruderman-Kittel-Kasuya-Yosida interaction for nonspherical fermi surfaces. *Physical Review* **149**, 519–525 (1966).

[110] Weismann, A. *et al.* Seeing the fermi surface in real space by nanoscale electron focusing. *Science (New York, N.Y.)* **323**, 1190–1193 (2009).

[111] Ding, H. *et al.* Tuning interactions between spins in a superconductor. *Proceedings of the National Academy of Sciences of the United States of America* **118**, e2024837118 (2021).

[112] Eigler, D. M. & Schweizer, E. K. Positioning single atoms with a scanning tunnelling microscope. *Nature* **344**, 524–526 (1990).

[113] Enders, A., Skomski, R. & Honolka, J. Magnetic surface nanostructures. *Journal of physics. Condensed matter : an Institute of Physics journal* **22**, 433001 (2010).

[114] Khajetoorians, A. A. *et al.* Atom-by-atom engineering and magnetometry of tailored nanomagnets. *Nature Physics* **8**, 497–503 (2012).

[115] Khajetoorians, A. A., Wegner, D., Otte, A. F. & Swart, I. Creating designer quantum states of matter atom-by-atom. *Nature Reviews Physics* **1**, 703–715 (2019).

[116] Odobesko, A. B. *et al.* Preparation and electronic properties of clean superconducting Nb(110) surfaces. *Physical Review B* **99**, 115437 (2019).

[117] Beck, P., Schneider, L., Wiesendanger, R. & Wiebe, J. Effect of substrate spin-orbit coupling on the topological gap size of Shiba chains. URL http://arxiv.org/pdf/2205.10062v1.

[118] Beck, P., Schneider, L., Wiesendanger, R. & Wiebe, J. Systematic study of Mn atoms, artificial dimers and chains on superconducting Ta(110). URL http://arxiv.org/pdf/2205.10073v1.

[119] Pawlak, R., Hoffman, S., Klinovaja, J., Loss, D. & Meyer, E. Majorana fermions in magnetic chains. *Progress in Particle and Nuclear Physics* **107**, 1–19 (2019).

[120] Jäck, B., Xie, Y. & Yazdani, A. Detecting and distinguishing Majorana zero modes with the scanning tunnelling microscope. *Nature Reviews Physics* **3**, 541–554 (2021).

[121] Nakosai, S., Tanaka, Y. & Nagaosa, N. Two-dimensional p -wave superconducting states with magnetic moments on a conventional s -wave superconductor. *Physical Review B* **88**, 180503(R) (2013).

[122] Röntynen, J. & Ojanen, T. Topological superconductivity and high Chern numbers in 2D ferromagnetic Shiba lattices. *Physical review letters* **114**, 236803 (2015).

[123] Li, J. *et al.* Two-dimensional chiral topological superconductivity in Shiba lattices. *Nature communications* **7**, 12297 (2016).

[124] Schecter, M., Syljuåsen, O. F. & Paaske, J. Cooper pair induced frustration and nematicity of two-dimensional magnetic adatom lattices. *Physical Review B* **97**, 174412 (2018).

[125] Wiesendanger, R. *Scanning Probe Microscopy and Spectroscopy* (Cambridge University Press, 2010).

[126] Voigtländer, B. *Scanning Probe Microscopy* (Springer Berlin Heidelberg, Berlin, Heidelberg, 2015).

[127] von Bergmann, K. Iron nanostructures studied by spin-polarised scanning tunneling microscopy. *Universität Hamburg, PhD thesis* (2004). URL `https://ediss.sub.uni-hamburg.de/handle/ediss/631`.

[128] Ternes, M. Scanning tunneling spectroscopy at the single atom scale. *Lausanne, EPFL, PhD thesis* (2006). URL `https://infoscience.epfl.ch/record/64356`.

[129] Bardeen, J. Tunnelling from a many-particle point of view. *Physical review letters* **6**, 57–59 (1961).

[130] Tersoff & Hamann. Theory of the scanning tunneling microscope. *Physical review. B, Condensed matter* **31**, 805–813 (1985).

[131] Chen. Origin of atomic resolution on metal surfaces in scanning tunneling microscopy. *Physical review letters* **65**, 448–451 (1990).

[132] Friedel, J. Metallic alloys. *Il Nuovo Cimento* **7**, 287–311 (1958).

[133] Ternes, M. Spin excitations and correlations in scanning tunneling spectroscopy. *New Journal of Physics* **17**, 063016 (2015).

[134] Bouaziz, J., Mendes Guimarães, F. S. & Lounis, S. A new view on the origin of zero-bias anomalies of Co atoms atop noble metal surfaces. *Nature communications* **11**, 6112 (2020).

[135] Fein, A. P., Kirtley, J. R. & Feenstra, R. M. Scanning tunneling microscope for low temperature, high magnetic field, and spatially resolved spectroscopy. *Review of Scientific Instruments* **58**, 1806–1810 (1987).

[136] Wiebe, J. *et al.* A 300 mK ultra-high vacuum scanning tunneling microscope for spin-resolved spectroscopy at high energy resolution. *Review of Scientific Instruments* **75**, 4871–4879 (2004).

[137] Shockley, W. On the surface states associated with a periodic potential. *Physical Review* **56**, 317–323 (1939).

[138] Herman, F. & Hlubina, R. Microscopic interpretation of the Dynes formula for the tunneling density of states. *Physical Review B* **94**, 144508 (2016).

[139] Küster, F. *et al.* Non-Majorana modes in diluted spin chains proximitized to a superconductor. *Proceedings of the National Academy of Sciences* **119**, e2210589119 (2022).

[140] Ambegaokar, V. & Baratoff, A. Tunneling between superconductors. *Physical review letters* **10**, 486–489 (1963).

[141] Bode, M. Spin-polarized scanning tunnelling microscopy. *Reports on Progress in Physics* **66**, 523–582 (2003).

[142] Slonczewski. Conductance and exchange coupling of two ferromagnets separated by a tunneling barrier. *Physical review. B, Condensed matter* **39**, 6995–7002 (1989).

[143] Küster, F. *et al.* Correlating Josephson supercurrents and Shiba states in quantum spins unconventionally coupled to superconductors. *Nature communications* **12**, 1108 (2021).

[144] Razinkin, A. S. & Kuznetsov, M. V. Scanning tunneling microscopy (STM) of low-dimensional NbO structures on the Nb(110) surface. *The Physics of Metals and Metallography* **110**, 531–541 (2010).

[145] Sürgers, C., Schöck, M. & Löhneysen, H. v. Oxygen-induced surface structure of Nb(110). *Surface Science* **471**, 209–218 (2001).

[146] Heinze, S., Blügel, S., Pascal, R., Bode, M. & Wiesendanger, R. Prediction of bias-voltage-dependent corrugation reversal for STM images of bcc (110) surfaces:

W(110), Ta(110), and Fe(110). *Physical review. B, Condensed matter* **58**, 16432–16445 (1998).

[147] Papanikolaou, N., Zeller, R. & Dederichs, P. H. Conceptual improvements of the KKR method. *Journal of Physics: Condensed Matter* **14**, 2799–2823 (2002).

[148] Bauer, D. S. G. *Development of a relativistic full-potential first-principles multiple scattering Green function method applied to complex magnetic textures of nano structures at surfaces: Zugl.: Aachen, Univ., Diss., 2013*, vol. 79 of *Schriften des Forschungszentrums Jülich Reihe Schlüsseltechnologien* (Forschungszentrum Jülich, Jülich, 2014). URL `http://hdl.handle.net/2128/5899`.

[149] Küster, F., Brinker, S., Lounis, S., Parkin, S. S. P. & Sessi, P. Long range and highly tunable interaction between local spins coupled to a superconducting condensate. *Nature communications* **12**, 6722 (2021).

[150] Brinker, S., Küster, F., Parkin, S. S. P., Sessi, P. & Lounis, S. Anomalous excitations of atomically crafted quantum magnets. *Science advances* **8**, eabi7291 (2022).

[151] Ternes, M., Heinrich, A. J. & Schneider, W.-D. Spectroscopic manifestations of the Kondo effect on single adatoms. *Journal of physics. Condensed matter : an Institute of Physics journal* **21**, 053001 (2009).

[152] Prüser, H. *et al.* Long-range Kondo signature of a single magnetic impurity. *Nature Physics* **7**, 203–206 (2011).

[153] Otte, A. F. *et al.* Spin excitations of a Kondo-screened atom coupled to a second magnetic atom. *Physical review letters* **103**, 107203 (2009).

[154] Loth, S. *et al.* Controlling the state of quantum spins with electric currents. *Nature Physics* **6**, 340–344 (2010).

[155] Odobesko, A. *et al.* Anisotropic vortices on superconducting Nb(110). *Physical Review B* **102**, 174502 (2020).

[156] Lounis, S., Costa, A. T., Muniz, R. B. & Mills, D. L. Dynamical magnetic excitations of nanostructures from first principles. *Physical review letters* **105**, 187205 (2010).

[157] Khajetoorians, A. A. *et al.* Itinerant nature of atom-magnetization excitation by tunneling electrons. *Physical review letters* **106**, 037205 (2011).

[158] Hirjibehedin, C. F., Lutz, C. P. & Heinrich, A. J. Spin coupling in engineered atomic structures. *Science (New York, N.Y.)* **312**, 1021–1024 (2006).

[159] Heinrich, A. J., Gupta, J. A., Lutz, C. P. & Eigler, D. M. Single-atom spin-flip spectroscopy. *Science (New York, N.Y.)* **306**, 466–469 (2004).

[160] Fernández-Rossier, J. Theory of single-spin inelastic tunneling spectroscopy. *Physical review letters* **102**, 256802 (2009).

[161] Chilian, B. *et al.* Anomalously large g factor of single atoms adsorbed on a metal substrate. *Physical Review B* **84**, 212401 (2011).

[162] Khajetoorians, A. A. *et al.* Spin excitations of individual Fe atoms on Pt(111): impact of the site-dependent giant substrate polarization. *Physical review letters* **111**, 157204 (2013).

[163] Bryant, B., Spinelli, A., Wagenaar, J. J. T., Gerrits, M. & Otte, A. F. Local control of single atom magnetocrystalline anisotropy. *Physical review letters* **111**, 127203 (2013).

[164] Oberg, J. C. *et al.* Control of single-spin magnetic anisotropy by exchange coupling. *Nature nanotechnology* **9**, 64–68 (2014).

[165] Stipe, Rezaei & Ho. Single-molecule vibrational spectroscopy and microscopy. *Science (New York, N.Y.)* **280**, 1732–1735 (1998).

[166] Pohlit, M. *et al.* Evidence for ferromagnetic clusters in the colossal-magnetoresistance material EuB$_6$. *Physical review letters* **120**, 257201 (2018).

[167] Pommier, D. *et al.* Scanning tunneling microscope-induced excitonic luminescence of a two-dimensional semiconductor. *Physical review letters* **123**, 027402 (2019).

[168] Madhavan, Chen, Jamneala, Crommie & Wingreen. Tunneling into a single magnetic atom: spectroscopic evidence of the Kondo resonance. *Science (New York, N.Y.)* **280**, 567–569 (1998).

[169] Hewson, A. C. *The Kondo Problem to Heavy Fermions* (Cambridge University Press, 2009).

[170] Knorr, N., Schneider, M. A., Diekhöner, L., Wahl, P. & Kern, K. Kondo effect of single Co adatoms on Cu surfaces. *Physical review letters* **88**, 096804 (2002).

[171] Asbóth, J. K., Oroszlány, L. & Pályi, A. The Su-Schrieffer-Heeger (SSH) model. In Asbóth, J. K., Oroszlány, L. & Pályi, A. (eds.) *A Short Course on Topological Insulators*, vol. 919 of *Lecture Notes in Physics*, 1–22 (Springer International Publishing, Cham, 2016).

[172] Batra, N. & Sheet, G. Understanding basic concepts of topological insulators through Su-Schrieffer-Heeger (SSH) model. *Resonance* **25**, 765–786 (2020). URL `http://arxiv.org/pdf/1906.08435v1`.

[173] Slot, M. R. *et al.* Experimental realization and characterization of an electronic Lieb lattice. *Nature Physics* **13**, 672–676 (2017).

[174] Li, Z. *et al.* Realization of flat band with possible nontrivial topology in electronic Kagome lattice. *Science advances* **4**, eaau4511 (2018).

[175] Ghimire, N. J. & Mazin, I. I. Topology and correlations on the Kagome lattice. *Nature materials* **19**, 137–138 (2020).

[176] Einstein, A. Die Grundlage der allgemeinen Relativitätstheorie. *Annalen der Physik* **354**, 769–822 (1916).

List of Publications

- Sessi, P., Fan, FR., Küster, F., Manna, K., Schröter, N. B. M., Ji, JR., Stolz, S., Krieger, J. A., Pei, D., Kim, T.K., Dudin, P., Cacho, C., Widmer, R., Borrmann, H., Shi, W., Chang, K., Sun, Y., Felser, C. & Parkin, S. S. P.
Handedness-dependent quasiparticle interference in the two enantiomers of the topological chiral semimetal PdGa.
Nature communications **11**, 3507 (2020).

- Zhang, Y., Küster, F., Zhang, J., Liu, D., Pal., B., Deniz, H., Sessi, P., Gilbert, M. J. & Parkin, S. S. P.
Competing Energy Scales in Topological Superconducting Heterostructures.
Nano Letters **2021**, 21, 2758-2765.

- Galeski, S., Ehmcke, T., Wawrzyńczak, R., Lozano, P. M., Cho, K., Sharma, A., Das, S., Küster, F., Sessi, P., Brando, M., Küchler, R., Markou, A., König, M., Swekis, P., Felser, C., Sassa, Y., Li, Q., Gu, G., Zimmermann, M. V., Ivashko, O., Gorbunov, D. I., Zherlitsyn, S., Förster, T., Parkin, S. S. P., Wosnitza, J., Meng, T. & Gooth, J.
Origin of the quasi-quantized Hall effect in $ZrTe_5$.
Nature communications **12**, 3197 (2021).

- Chang, K., Villanova, J. W. D., Ji, J.-R., Das, S., Küster, F., Barraza-Lopez, S., Sessi, P. & Parkin, S. S. P.
Vortex-Oriented Ferroelectric Domains in SnTe/PbTe Monolayer Lateral Heterostructures.
Advanced Materials **2021**, 33, 2102267.

- Küster, F., Montero, A., Guimarães, F., Brinker, S., Lounis, S., Parkin, S. S. P. & Sessi, P.
Correlating Josephson supercurrents and Shiba states in quantum spins unconventionally coupled to superconductors.
Nature communications **12**, 1108 (2021).

- Küster, F., Brinker, S., Lounis, S., Parkin, S. S. P. & Sessi, P.
Long range and highly tunable interaction between local spins coupled to a super-

conducting condensate.
Nature communications **12**, 6722 (2021).

- Brinker, S., Küster, F., Parkin, S. S. P., Sessi, P. & Lounis, S.
  Anomalous excitations of atomically crafted quantum magnets.
  Science advances **8**, eabi7291 (2022).

- Küster, F., Brinker, S., Hess, R. G., Loss, D., Parkin, S. S. P., Klinovaja, J., Lounis, S. & Sessi, P.
  Non-Majorana modes in diluted spin chains proximitized to a superconductor.
  Proceedings of the National Academy of Sciences **119**, e2210589119 (2022).

- Soldini, M.O., Küster, F., Wagner, G., Das, S., Aldarawsheh, A., Thomale, R., Lounis, S., Parkin, S.P.P., Sessi, P. & Neupert, T.
  Two-dimensional Shiba lattices as a possible platform for crystalline topological superconductivity.
  Nature Physics (2023).

Selbstständigkeitserklärung / Declaration

Ich, Felix Küster, erkläre hiermit, dass ich diese Arbeit selbstständig und ohne fremde Hilfe verfasst, andere als die von mir angegebenen Quellen nicht benutzt und die den benutzten Werken wörtlich oder inhaltlich entnommenen Stellen als solche kenntlich gemacht habe.

I hereby declare that this thesis is entirely my own work, has been written without the help of others, that I only used the mentioned sources and indicated all kinds of citations correctly.

_____

Curriculum Vitae

Felix Küster

Personal Details

Name	KÜSTER, Felix
E-Mail	felix.kuester@mpi-halle.mpg.de

Education

2018/04 – present	Max Planck Institute of Microstructure Physics NISE department, low temperature STM group Doctoral student
2017/07 – 2018/04	UNISOKU Co., Ltd. Osaka, Japan Department Scanning probe microscopy R&D Scholarship DAAD (German Academic Exchange Service) Program "Language and Practical Experience in Japan"
2016/09 – 2017/06	Naganuma School for Japanese Studies, Tokyo, Japan Scholarship DAAD (German Academic Exchange Service) Program "Language and Practical Experience in Japan"
2016/06 – 2016/09	Friedrich Schiller University of Jena, Germany Institute of Solid State Physics, Fritz Group (Surface Physics) Scientific Assistant
2013/10 – 2016/06	Friedrich Schiller University of Jena, Germany Final degree: Master of Science Physics Focus: Solid State Physics and Optics/Photonics Master Thesis: "Electron Correlations in and Temperature Dependent Physical Properties of Axially Substituted Metal-Phthalocyanines"
2014/10 – 2015/08	Osaka University, Japan Graduate School of Science, Hanasaki Group (Strong Electron Correlations) FrontierLab@OsakaU Program, JASSO Scholarship
2010/10 – 2013/10	Friedrich Schiller University of Jena, Germany Degree: Bachelor of Science Physics